INFORMATION TO USERS

This manuscript has been reproduced from the microfilm master. UMI films the text directly from the original or copy submitted. Thus, some thesis and dissertation copies are in typewriter face, while others may be from any type of computer printer.

The quality of this reproduction is dependent upon the quality of the copy submitted. Broken or indistinct print, colored or poor quality illustrations and photographs, print bleedthrough, substandard margins, and improper alignment can adversely affect reproduction.

In the unlikely event that the author did not send UMI a complete manuscript and there are missing pages, these will be noted. Also, if unauthorized copyright material had to be removed, a note will indicate the deletion.

Oversize materials (e.g., maps, drawings, charts) are reproduced by sectioning the original, beginning at the upper left-hand corner and continuing from left to right in equal sections with small overlaps.

Photographs included in the original manuscript have been reproduced xerographically in this copy. Higher quality 6" x 9" black and white photographic prints are available for any photographs or illustrations appearing in this copy for an additional charge. Contact UMI directly to order.

ProQuest Information and Learning
300 North Zeeb Road, Ann Arbor, MI 48106-1346 USA
800-521-0600

UMI®

Morphology and Optical Properties of Polyolefin Blown Films

Lei Wang
Department of Chemical Engineering
McGill University, Montreal

November 1999

A Thesis submitted to the Faculty of Graduate Studies and Research in partial fulfiment of the requirements for the degree of Doctor of Philosophy

National Library
of Canada

Acquisitions and
Bibliographic Services

395 Wellington Street
Ottawa ON K1A 0N4
Canada

Bibliothèque nationale
du Canada

Acquisitions et
services bibliographiques

395, rue Wellington
Ottawa ON K1A 0N4
Canada

Your file Votre référence

Our file Notre référence

0-612-64689-0

Canada

To my parents

Morphology and Optical Properties of Polyolefin Blown Films

by

Lei Wang

Submitted to the Department of Chemical Engineering
on November 1999, in partial fulfillment of the requirements for
the degree of Doctor of Philosophy

Abstract

Optical properties of polyethylene blown films are of great commercial and scientific interest. An understanding of the relationship between morphology and optical properties will have a significant impact on product and process optimization.

In this work, a number of linear low density polyethylene (LLDPE) resins of different molecular and structural characteristics were studied. Intrinsic properties such as refractive index and absorption coefficient were estimated from resin compositions using group contribution models. The refractive indices of sample films were also measured using the method of Transmission Spectrum.

The morphology of polyethylene films was investigated using Atomic Force Microscopy (AFM) and Near-field Scanning Optical Microscopy (NSOM). Both the surface and bulk morphologies were evaluated. The observation shows the dominant spherulitic structure on the surface as well as in the bulk, as the result of nucleation and crystallization during the film blowing process. In addition to qualitative observations and comparisons, quantitative characterization methods were employed to describe the features of the morphology.

Based on the morphology characterization, the surface reflection was described by the Beckmann-Davies theory of reflection of electro-magnetic waves by rough surface. The directional distribution of reflected intensity was computed according to the surface roughness information. The gloss values of sample films were computed accordingly and compared with experimental measurements. Furthermore, the problem of light transmission and scattering was investigated. A scattering geometry was proposed from the observations of the morphology of sample films. The light scattering by the surface of polymer films was analyzed using a model that is based on the Mie theory of scattering. The haze values of sample films were computed and compared with experimental measurements.

Morphologie et propriétés optiques de films polyolefins

par

Lei Wang

Soumis au département de génie chimique en Novembre 1999,
en vue de l'obtention du titre de Docteur en Philosphie

Résumé

Les propriétés optiques des films de polyéthylènes obtenus par gonflage de gaine sont d'un grand intérêt à la fois commercial et scientifique. La compréhension de la relation entre la morphologie et les propriétés optiques aura un impact important sur l'optimisation du procédé et du produit.

Dans ce travail, un certain nombre de résines de polyéthylène linéaire basse densité (LLDPE) de différentes caractéristiques moléculaires et structurelles ont été étudiées. Les propriétés intrinsèques comme l'indice de réfraction et le coefficient d'absorption ont éte estimées à partir de la composition de la résine en utilisant les modèles de contribution de groupe. L'indice de réfraction des échantillons de film a également été mesuré par la méthode de Spectre de Transmission.

La morphologie des films de polyéthylène a été étudiée à l'aide d'un Microscope à Force Atomique (AFM) et d'un microscope optique à balayage near field (NSOM). Les morphologies de surface et interne ont été évaluées. Les observations montrent une structure sphérolythique dominante tant à la surface qu'à coeur, résultant de la nucléation et de la cristallisation pendant le procédé d'extrusion gonflage. En plus de ces observations et comparaisons qualitatives, des méthodes de caractérisations qantitatives ont éte utilisées pour décrire l'évolution de la morphologie.

A partir de la caractérisation de la morphologie, la reflection surfacique a été décrite par la théorie de Beckmann-Davies de reflection des ondes electro-magnetiques par surface rugueuse. La distribution directionnelle de l'intensité de reflection a été calculée numériquement à partir de la rugosité de la surface. Les valeurs de gloss des échantillons de film ont alors été calculées et comparées à des mesures expérimentales. Par ailleurs, le probème de transmission de la lumière et de la diffusion ont été abordés. Une géométrie diffusive a été proposée à partir d'observations de la morphologie d'échantillons de films. La lumière diffusée par la surface du film de polymère a été analysée en utilisant un modèle basé sur la théorie de diffusion de Mie. Les valeurs de haze des échantillons de film ont été calculées et comparées avec des mesures expérimentales.

Acknowledgments

I would like to express my deepest gratitude towards my supervisors: Dr. Musa R. Kamal and Dr. Alejandro D. Rey. Their guidance and encouragement were indispensable in the completion of this thesis.

I would like to thank Dr. Tao Huang of the research group for his advice and assistance through out this project.

Special thanks to Ms. Zuojian Tang for obtaining some of the AFM images of surface morphology and for microtoming the cross-section samples of films.

Thanks to Dr. Mark P. Andrews and Dr. Serge Pelissier of the Department of Chemistry of McGill University for their invaluable help with the measurements of refractive indices of sample films.

Thanks to Dr. Joo Teh of NOVA Chemicals at Calgary, Alberta for supplying the samples and data that made this project possible.

Thanks to all the members in Polymer research group for the lively discussions and assistance during the course of this project.

Thanks to Miss Kimberly Huie for proof reading the draft of this thesis.

I also wish to acknowledge the financial support of the Natural Sciences and Engineering Research Council of Canada (NSERC), Formation de Chercheurs et l'Aide à la Recherche (FCAR), Gouvernement du Québec and McGill University.

Finally and most importantly, I would like to thank my parents and my brother for their love and support.

Contents

List of Figures

List of Tables

Chapter 1

Introduction

Polymeric materials are widely used in packaging, usually in the form of films. The most important factors in selecting films for packaging applications are strength, barrier properties and transparency. The properties of a film are a consequence of its structures. This structure may be considered at different levels, ranging from the molecular to macroscopic. Many properties, such as density and electrical properties depend upon the molecular structure, whereas transparency and mechanical properties depend upon larger structures. The strength and flexibility of crystalline polymers, for example, depends upon the size, perfection and organization of the crystals. This project seeks to establish the underlying principles that relate optical properties, particularly haze and gloss, of polyethylene films to film morphology.

1.1 The Film Blowing Process

The most common method to produce polyolefin films is the film blowing process [1]. Film blowing produces thin films more rapidly and economically than the casting process. The melt film blowing process is based on simultaneous stretching and inflation of a moving tube of polymer melt extruded from an annular die. The bubble of molten polymer is cooled while this is occurring and crystallizes at a freeze-line, beyond which no significant deformation is possible. The inflated circular-cylindrical tube so formed is further cooled and then passed through a train of guide rollers which flatten it sufficiently for it to go through a pair of driven rubber nip-rolls without crinkling. It is then wound onto cylindrical cores as final product, either as tubes or as flat sheets after the sides are cut off. The schematic of the film blowing process called *tubular film blowing* or simply film blowing is shown in Figure 1-1. This process most often is conducted vertically upward.

In practice, cooling is usually achieved by blowing a jet of cool air onto the film from an annular air ring external to the die. In addition, internal cooling is achieved by air inside the bubble. The bubble is, in principle, unsupported between the die and the guide system. The biaxial stretching is achieved by over pressure from inside before the freeze-line. The two axes of orientation are the axial direction (*machine direction*, MD) due to the drawing of the tube and the circumferential direction (*transverse direction*, TD) due to the blowup of the tube. The mechanical properties of blown film are nearly uniform in both directions as a result of this biaxial orientation.

The film blowing process is very important commercially. A substantial fraction of polyolefin production (low-density polyethylene LDPE, linear low-density polyethylene LLDPE, high-density polyethylene HDPE and polypropylene PP) is converted into packaging films [1]. The quality of the output is usually measured by the uniformity of film thickness and the optical clarity. Uniformity of film thickness requires steady uniform output from the screw extruder driving the flow, a well designed die held at a steady uniform temperature with a carefully designed die gap, even air cooling and low friction at the guide rolls or plates. Unfortunately, the complexity of this process and the great number of processing parameters involved, combined with the complexity of the process of melt solidification have made it difficult to obtain comprehensive and accurate analysis of the film blowing process and the morphology evolution during the process.

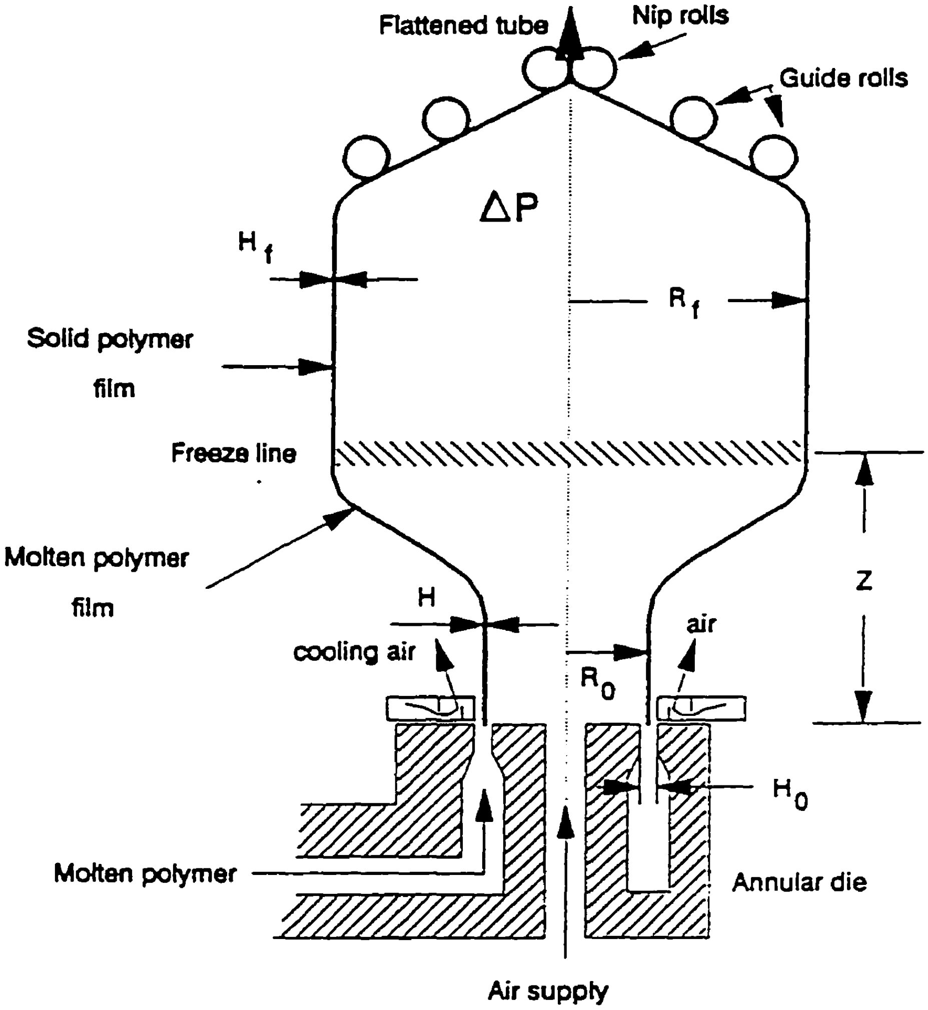

Figure 1-1: Schematic of the film blowing process

1.2 Semicrystalline Polymers

The polymer single crystal was first discovered in 1957 by Keller [2]. These single crystals are lamellar structures, about 100Å thick, in which perfect order exists, as has been shown by electron diffraction patterns. In most solid crystalline polymers, spherical aggregates of crystalline material, called *spherulites*, are recognized by their characteristic appearance under the polarized light microscope. Electron microscopy of fracture surfaces in spherulites has shown that lamellar structures persist throughout the body of the spherulites. This seems to be the natural result of crystal growth, in which the spherulite originating from a nucleus grows at the expense of the surrounding non-crystalline melt. Most or all linear polymers can crystallize [3]. Among polyolefins, this is the case with polyethylene (PE). The situation is more complex for polymers that contain bulkier side groups attached to the backbone. For polyolefins, atactic polypropylene (PP, side chain: CH_3) or polystyrene (PS, side chain:phenyl group) are amorphous.

Semicrystalline polymers are a complex mixture of amorphous and crystalline phase polymers. It is generally assumed that their morphology consists of thin crystalline lamella separated from each other by amorphous layers and connected by tie molecules through the amorphous phase. Crystalline lamellar and amorphous interlamellar layers can form spherulites or other types of morphological textures. Spherulites are the basic morphology for polymers crystallized from the melt or concentrated solutions. They are usually obtained in industrial processes such as extrusion or injection molding. In a spherulite, crystalline lamella separated by amorphous layers radiate from a center and branch sufficiently often to occupy the outwardly increasing volume. The spherulitic structure is the dominant morphology in polyethylene blown films, as shown in later sections.

1.3 Appearance of Transparent Objects

The appearance of a transparent object consists of several visual characteristics, as shown in Figure 1.3.

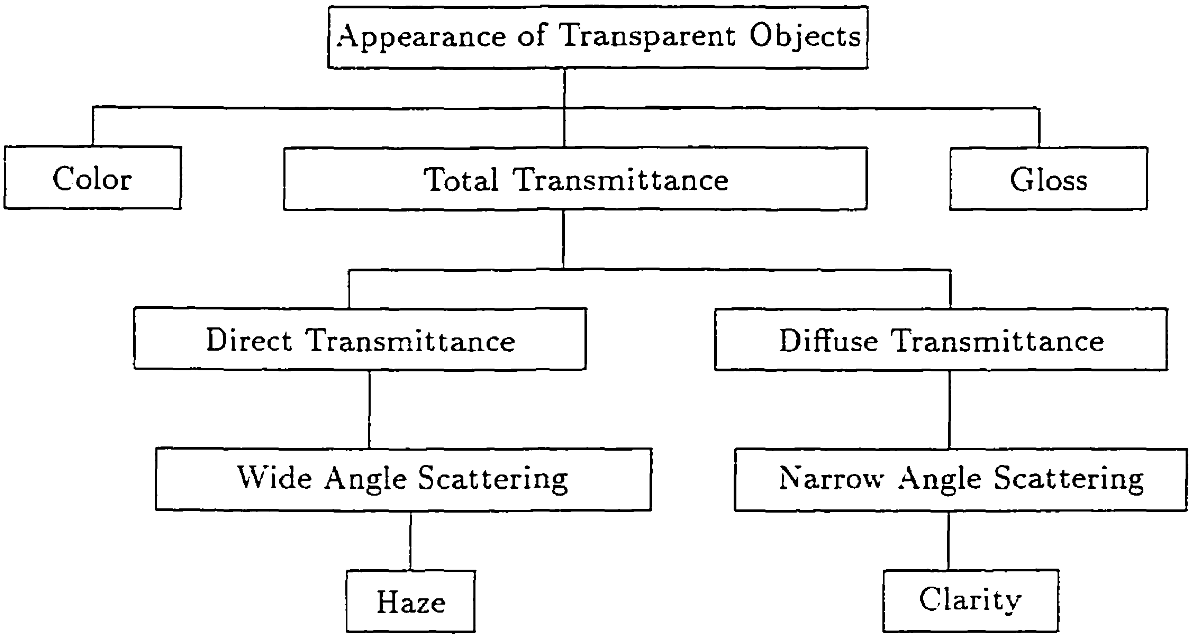

Figure 1-2: Appearance of Transparenct Objects

The terms most often used to describe the optical appearance of an object are transparency, translucency and opacity. A transparent sample is one that transmits light so as to render objects beyond it perfectly visible. At the other extreme, an opaque material transmits no light, and all information concerning objects lying behind it is lost. A translucent specimen lies between these two extremes in that it transmits light, but diffuses it so that objects beyond it are not completely visible. The difference between transparency and translucency is best illustrated by examining clear glass and frosted glass. In most cases, polymeric materials have intermediate properties. For example, polyethylene film is transparent in the sense that objects may be approximately seen clearly through it, but it is not perfectly clear like fine optical glass and often possesses a hazy and turbid appearance. Different films may also differ in the degrees of haziness and fine detail resolution of the images of objects beyond them. For polymeric films, direct transmittance is defined as the ratio of the intensity of light that does not deviate from its incident direction to the original intensity[4]. When the direct transmittance is larger than 90%, the film is considered transparent, and when it is less than 90%, the film is considered translucent. An opaque material has transmittance of 0%.

The deterioration of the image viewed through a polymer film is due to the decrease in light intensity when passing through the film. This reduction in intensity is mainly due to light scattering at the surface and in the bulk of the film. The scattering of light is the result of inhomogeneity of the medium due to spatial variations of the refractive index in the film. The refractive index variation could be the result of local density variation. Polymers with regular molecules, such as polyethylene and co-polymers, are likely to crystallize during the solidification process, whereas amorphous polymers, such as polymethyl methacrylate and polystyrene, rarely solidify into the crystalline phase. Since the density of the crystalline phase polymer is higher, the refractive index is higher than that of the amorphous phase. As a result, the crystalline polymers tend to scatter light more than amorphous polymers and, therefore, the former appear less transparent.

1.3.1 Color

The color of a transparent object is associated with absorption of certain wavelengths of the visible light spectrum ($400nm - 800nm$). This effect in polymer films is usually achieved by incorporating pigments and/or dye into the melt. The coloring additives are well-mixed with the polymer melt and the final product. Because of the presence of additives, the corresponding wavelength will be absorbed when white light passes through the specimen. As a result, the color of the specimen will be the sum of the residual visible light spectrum. It is known that color is not an absolute property, but depends very much on the surface condition of the test sample and viewing conditions. Two colors that will match in one set of conditions may not match in another. Similarly, two mouldings of a plastic material may appear to have different colors if their surface finishes are different. Hence, the differentiation and testing of color is still largely done visually [5]. Color of polymer films is not within the scope of this project.

1.3.2 Total Transmittance

The total transmittance is the ratio of all the light flux that is transmitted through the specimen to that of the incident light. It represents the ability to carry visual information of objects located on one side to an observer located on the other end. This ability may be reduced by imperfect transmission, such as loss of light intensity due to surface reflection, light scattering at the surface and the bulk, refraction at both surfaces and absorption by the material. Since total transmittance includes all of the light intensity that is transmitted, it is further divided into direct transmittance and diffuse transmittance according to the direction of the light flux.

Direct Transmittance

Direct transmittance is the amount of light flux that does not deviate from the path of incident light.

Diffuse Transmittance: Haze and Clarity

Diffuse transmittance includes all of the light intensity that deviates from the path of incident light, due to light scattering or refraction by the object. It is further divided into narrow angle scattering and wide angle scattering, which lead to the two most important areas of evaluating transparency of a polyethylene film: haze and clarity.

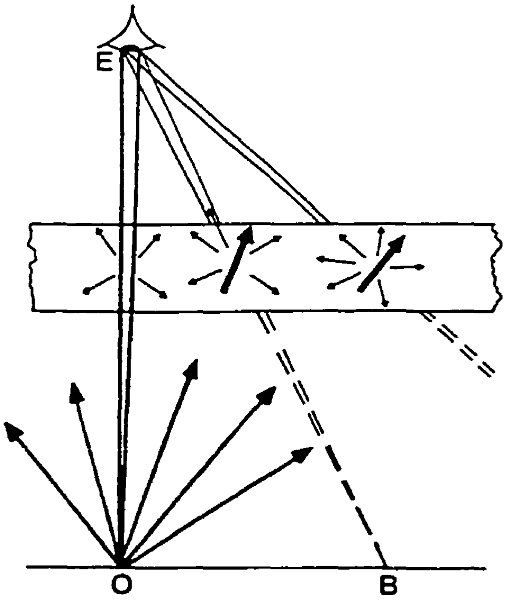

Figure 1-3: Schematic of how light scattering affects the contrast of objects viewed through a scattering specimen

Figure 1-3 shows how a specimen that is scattering light affects the appearance of an object viewed through it. In order to simplify the diagram, refraction and reflection at the specimen/air boundaries have been omitted, since they do not materially affect the following discussion. The simplest possible object is considered. A single luminous point is placed at O on an otherwise black background. The first situation to be examined is when the scattering specimen is absent. The point O emits light in all directions, but only that travelling within a narrow cone enters the eye at **E** and forms the visual image. No other light is received by the eye. If the eye turns to look at point **B**, the center of the field of vision will appear dark. If a scattering specimen is now interposed between the observer and the object, the situation will change into what is shown in Figure 1-3. First of all, some of the light that would have travelled to the eye directly will be scattered as it traverses the specimen, so that the point O will appear less bright. Secondly, if the eye is focused on point **B**, it will receive some light that has been scattered by the sample. Thus, the net effect of light scattering by the specimen inserted between object point O and the receiver is to make the bright spot less bright and the surrounding area lighter. The contrast of the object viewed through the specimen is therefore reduced, and the object will appear hazy.

Consequently, if the quantity of scattered light increases, the point O will appear darker, the point **B** and the surrounding area brighter, and the contrast will decrease. The directional distribution of the scattered light also affects the appearance of the object. From Figure 1-3, it is evident that as the center of the field of vision moves away from the bright point O through **B**, the angle, at which light is scattered in order to reach the eye, increases.

The second aspect of transparency is clarity, which is defined as the ability of a specimen to transmit the fine detail of an object placed beyond it. Figure 1-4 illustrates two neighboring bright point objects at O and O′ on an otherwise uniformly black back-

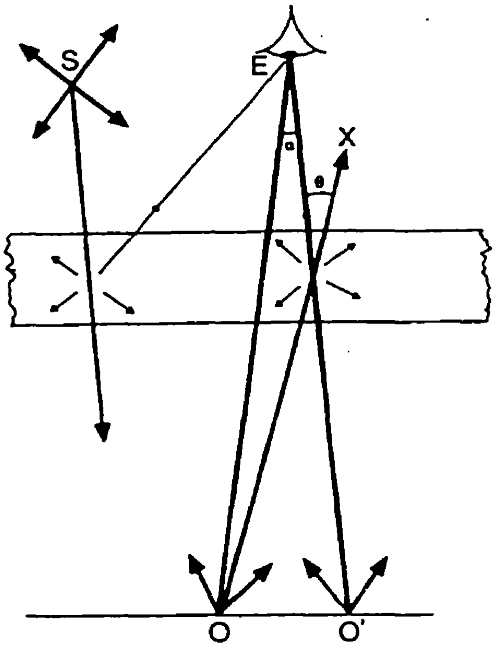

Figure 1-4: Schematic of how light scattering affects the fine details of objects viewed through a scattering specimen

ground. To simplify the diagram, only the central rays of the cones of light entering the eye have been drawn, and reflection and refraction at the specimen/air boundaries have been omitted. The case is considered in which the angle α is about one minute of arc, so that in the absence of the scattering specimen, the two bright points are just resolved by eye. When the specimen is interposed, some of the light emitted by point **O** in the direction **OX** will be scattered through an angle θ, and will appear to be coming from **O′**. If the scattering specimen is not too close to **O** and **O′**, since α is small, θ is small. If the intensity of this light scattered at low angles is comparable with that reaching the eye directly from **O′**, it impairs the observer's ability to see **O′**. When the specimen is inserted between the eye and the object, light scattered at low angles causes the two point-sources to appear to be surrounded by bright halos. If these halos overlap, the points can no longer be resolved. Thus, the inability to resolve fine detail through a sample is due to light scattered at low angles. The apparent loss of contrast in objects is caused by light scattered at larger angles. These facts form the basis of the physical methods for assessing clarity and haze. The separation between these aspects of transparency is due to this difference between the scattering angles corresponding to the two cases.

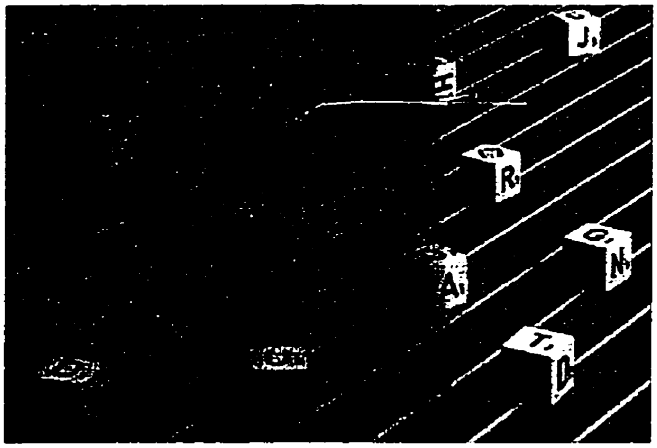

Figure 1-5: Visualization of haze: loss of contrast

The visual effects of haze and clarity are illustrated in Figure 1-5 and Figure 1-6. As shown, a group of cubes are randomly placed on the ground. The lines indicate the distance among cubes and the distance from the viewer. The viewing field is then half covered with a polymer film. As can be seen in the first case in Figure 1-5, the contrast of the field is reduced when viewed through the specimen. The letters on the cube on the right side appear darker than those on the cube on the left side which are behind the film. One may also notice that the details, the letters, of the cube are still visible and that the contrast reduction is uniform over the distance.

In Figure 1-6 the situation is somewhat different. The contrast of the letters on all the cubes remains close. The letters, however, on the cubes on the left side of the viewing field, which are viewed through the film, are not clear. For cube close to the film, the details of the letters are still distinguishable. For cubes further away from the film, however, all details are lost and the letters on these cubes are rendered completely unrecognizable. This experiment reveals the different aspects of appearance that are associated with haze and clarity. In addition, it also shows the key factor in differentiating haze and clarity. Haze is independent of distance, whereas clarity strongly depends upon the distance between the film and the objects beyond it.

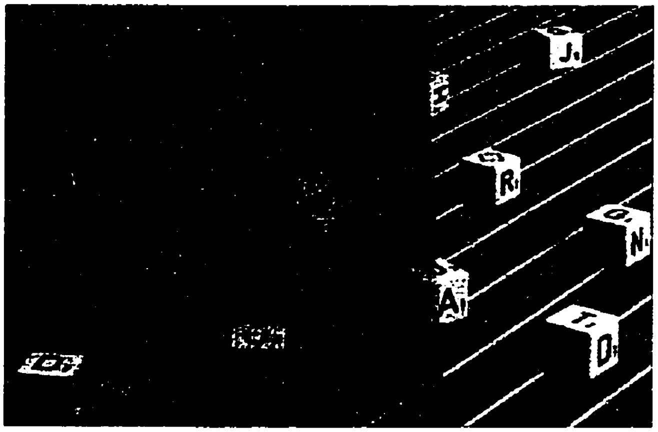

Figure 1-6: Visualization of clarity: loss of fine details

1.3.3 Gloss

Another important aspect in the appearance of polymer films is gloss. Gloss is concerned not with the visibility of a body viewed through a sample, but rather with the quality of the image formed by reflection of its surface. It is on the basis of such assessments that we differentiate between a high gloss and a matte paint, regular paper and photographic papers. It should be noted that transparency is influenced both by the surface and the interior of the specimen, whereas gloss is a property dominated by surface features. Physically, it represents the specular reflection of the surface as defined by industrial standards [6]. For a perfectly smooth surface, incident light is completely reflected in the specular direction and there is no light reflected in the other directions. In this case, the surface appears to be clear and mirror-like. At the other extreme, for a very rough surface, the specular reflection is diffused completely and the surface appears matte.

1.4 Motivations and Scope of the Thesis

The optical properties of polymer thin films are important criteria in determining their applications. Thus, the study of appearance is of great importance, both commercially and scientifically. At the simplest level, the concern is to understand the relationship between the transmitted and reflected light intensity due to an object, and its visual appearance, in order that the physical appearance may be related to the structure of the object. At a higher level, the manufacturer may wish to exercise control over the microstructure of the product, so as to achieve the desired appearance. Like other macroscopic physical properties, the optical properties of polymer films are determined by film morphology and resin composition. The former is strongly influenced by processing conditions. Previous experimental studies, as reviewed in detail in later sections, focused on empirical studies of the effect of resin compostions and processing conditions on the optical properties. Due to the complexity of resin compositions and processing conditions, it is very difficult to obtain fundamental relationship describing the optical properties of films. Since the optical properties of plastic films are strongly influenced by the morphology, it is reasonable to deal with the issue of the transparency of films in relation to morphological factors.

The goal of this project is to obtain an understanding of the relationship between the morphology and optical properties. Such an understanding would help to determine the processing and compositional factors that influence the optical properties of plastic films. Ultimately, this should enhance the optimization of compositions and processing conditions in order to obtain desirable transparency and gloss characteristics.

Light emanating from an object is characterized by its state of polarization, its directional distribution, and by the combination of wavelengths that it contains. Since the eye is insensitive to polarization differences, this aspect will not be considered in this project. The directional distribution determines both the transparency and gloss of the object. It is specifically these geometric aspects that will be considered. The appearance of color is also an important optical property. The differences in color arise from the differential absorption of the wavelengths present in the incident light. However, since the materials concerned in this project are mostly colorless, the focus shall be placed on the transmission and reflection of light by the material.

1.5 Thesis Objectives

The main objectives of the research carried out in this thesis are listed below:

1. To predict the refractive index of polyethylene films from the chemical composition of resins and to verify the predictions using experimental methods

2. To characterize the surface and bulk morphologies of polyethylene blown films using Atomic Force Microscopy and Near-field Scanning Optical Microscopy
3. To develop a quantitative mathematical description of the morphology in polyethylene blown films
4. To employ optical theory to predict the gloss of a collection of polyethylene blown films
5. To develop a realistic model of light transmission and scattering for polyethylene blown films
6. To validate the models developed in (5) by comparing the predictions from the models with experimental data.

1.6 Thesis Organization

Chapter 2 deals with the refractive index of the materials. The prediction of refractive index is made based upon the resin composition information. An alternative method to measure the refractive index is introduced to measure the refractive indices of polymer thin films. Comparisons are made between the refractive indices computed from the structural information of the resins with those measured from the film samples.

In Chapter 3, a thorough study of film morphology using various microscopic methods is presented. Both the experimental observations and the characterization of these observations are presented.

A model of gloss, based on the Beckmann theory of reflection of electro-magnetic waves by a rough surface is presented in Chapter 4. This model is used for computing the reflection field intensity for simulated rough surfaces as well as for surfaces of film samples. The gloss of film samples is computed from the surface morphology derived in Chapter 3. The results are compared with experimental measurements.

Light scattering by polymer films is discussed in Chapter 5. The scattering geometry is identified based upon the observations made in Chapter 3. Computations for forward light transmission are made for simulated geometries and film samples as well.

Chapter 6 presents the general conclusions of the thesis, suggestions for future work and contributions to knowledge.

Chapter 2

Refractive Index

2.1 Refraction and Extinction

A light beam can be considered either as an electro-magnetic wave or a stream of photons. The wave description is most often used in describing the propagation of light. A simple harmonic plane wave traveling in the z direction can be described by a complex disturbance $U(t, z)$ at any given time t,

$$U = U_0 exp[i(\omega t - kz)] \tag{2.1}$$

where U_0 is the amplitude of the electro-magnetic wave. ω and k are the angular frequency ($rads^{-1}$) and wave number, respectively. The wave number can also be written as:

$$k = \frac{2\pi}{\lambda} \tag{2.2}$$

where λ is the wavelength. The phase velocity of the wave is given by:

$$v = \frac{\omega}{k} \tag{2.3}$$

Maxwell's theory of the propagation of electro-magnetic wave shows that a coherent, linearly polarized, plane wave consists of a transverse vibrating electric field vector **E** and a transverse vibrating magnetic field vector **H**, **E** and **H** being perpendicular to each other [7]. These vectors are related by $\mathbf{E} = Z\mathbf{H}$ where Z is the wave impedance given by $\sqrt{\mu_r \mu_0 / \epsilon_r \epsilon_0}$. The medium is described by the relative permeability μ_r and relative permittivity ϵ_r. μ_0 and ϵ_0 represent the permeability and permittivity of free space, respectively. At optical frequencies, $\mu_r = 1$ is very close to physical reality and $\epsilon_r = n^2$, where n is the refractive index and is defined as the ratio of velocity of light in free space to the velocity of light when passing through the medium. For transparent media, i.e. there is no attenuation when light passes through, n and Z are real and **E** and **H** are in phase. For attenuating materials, the refractive index takes a complex form of $\mathbf{n} = n - i\kappa$ where n and κ represent the refraction and extinction, respectively. Z is also a complex quantity and **E** and **H** are out of phase by $\arctan(\kappa/n)$. The intensity of the wave is then given by the time average of Poynting's vector $\mathbf{E} \times \mathbf{H}$. In optics, the amplitude U is usually taken to represent the electric field E because optical materials are predominantly dielectric rather than magnetic at optical frequencies and also because most of the optical effects are related to E rather than to the magnetic field H. The intensity of light is thus proportional to $|U|^2$.

Consider a coherent plane wave incident on a slice of material, with its two surfaces parallel to each other. Assume the incident amplitude to be U_0, and the existing amplitude to be U. Light undergoes a change of phase when it passes through the material. In addition, some light may be lost due to extinction, either from scattering or from absorption by the material. This phase change and extinction can be represented by a complex refractive index $\mathbf{n} = n - i\kappa$. The existing amplitude is then given by:

$$U = U_0 exp(-ik_0 nz) exp(-k_0 \kappa z) \tag{2.4}$$

where k_0 is the free space wave-number. This describes a harmonic wave whose amplitude is decreasing exponentially as it passes through the material. The intensity I of the existing light beam is obtained from $|U|^2$:

$$I = I_0 exp(-2k_0\kappa z) \tag{2.5}$$

The attenuation or extinction coefficient $2k_0\kappa$ is composed of the contributions of scattering and absorption: $2k_0\kappa = a + k$. Here a and k are the absorption coefficient and scattering coefficient, respectively.

The basic law of refraction was found by Snellius (1618). It represents the significance of refractive index in geometric optics. It is known as Snell's law:

$$n = \frac{\sin i}{\sin r} \tag{2.6}$$

where i and r are the incident angle and refraction angle of the light beam, respectively.

2.2 Group Contribution Theory

2.2.1 Dielectric Description of Refraction

The refraction and extinction of polymers may be described by dielectric polarization at optical frequencies [8]. For an assembly of N objects per unit volume, each of size much smaller than the wavelength λ, and sufficiently separated to be non-interacting, the dielectric polarization P in the applied field E is given by $P = N\alpha E$. Here α is defined as the average optical polarizability. The dielectric displacement D is given by $D = \epsilon_0 E + P$ where ϵ_0 is the permittivity of free space. The relative permittivity ϵ_r of the assembly defined by $D = \epsilon_0 \epsilon_r E$. It follows that

$$\epsilon_r = 1 + \frac{N\alpha}{\epsilon_0} \tag{2.7}$$

The polarizability α is generally complex, being written as $\alpha = \alpha' - i\alpha''$. The real part of α describes refraction and the imaginary part describes extinction. Thus, ϵ_r is generally complex and related to the complex refractive index by $\epsilon_r = \mathbf{n}^2$. It follows that

$$n^2 + \kappa^2 = 1 + \frac{N\alpha'}{\epsilon_0} \tag{2.8}$$

2.2.2 Lorenz-Lorentz Relationship

It is from the dielectric description of refraction theory that Lorenz [9] and Lorentz [10] independently formulated the following relationship,

$$\frac{\epsilon_r - 1}{\epsilon_r + 2}\frac{M}{\rho} = \frac{4n}{3}N\alpha' = P = \frac{n^2 - 1}{n^2 + 2}\frac{M}{\rho} = R_{LL} \tag{2.9}$$

Here, M is the molecular weight and ρ is the density of the compound. R_{LL} is the Lorenz-Lorentz molar refraction.

2.2.3 Gladstone-Dale Relationship

For organic liquids, Gladstone and Dale found that the ratio $(n-1)/\rho$ is a characteristic constant of the substance when measured at a standard wavelength [11]. They also established the relationship:

$$\frac{M}{\rho}(n - 1) = R_{GD} \tag{2.10}$$

where R_{GD} is the Gladstone-Dale molar refraction. It should be noted that the Lorenz-Lorentz relation is largely a theoretical one, whereas the Gladstone-Dale relation is empirical.

2.2.4 Predicting Refractive Index of Polymers

Goedhart [12] used the above two molar refractions to study the index of refraction for over 100 different organic compounds with 43 different functional groups. He was able to assign a molar refraction value to individual functional groups. Using these groups to predict n yielded a precision of ±0.4% (standard deviation). The values of Lorenz-Lorentz molar refraction R_{LL} and Gladstone-Dale molar refraction R_{GD} for different functional groups at $\lambda = 589nm$ are listed by van Krevelen [4]. van Krevelen also used these values to calculate the index of refraction of 51 polymers. The R_{LL} and R_{GD} group values yield refractive index values within ±0.5% (standard deviation) from experimental measurements. Since most of the group contributions for R were developed from data on liquid organic compounds rather than polymers, its applicability for crystalline polymers is not clear. This is because the long chain is regularly folded and the functional groups are much closer to each other than they are in solutions. As shown by van Krevelen, however, these group contributions can be used to calculate the refractive indices of crystalline polymers with reasonable accuracy. The reason for this transferability of R values from liquid organic compounds to high polymers is that the intrinsic refractive power of a given structural unit is only affected very slightly by whether this structural unit is located in a small molecule or in a polymer chain. Changes in the molar volume account for most of the differences between the refractive indices of liquid organic compounds and polymers containing the same structural units. The refractive index of the crystalline phase polymer is usually higher than that of the amorphous phase. For example, the refractive index n at 298K of polyethylene is 1.476 in the limit of 0% crystallinity (completely amorphous), and 1.565 in the limit of 100% crystallinity [13]. Since the density of the crystalline phase is also higher, however, the molar refraction in both the Lorenz-Lorentz relationship and Gladstone-Dale relationship remains constant. An alternative approach to predict the refractive index of all polymers constructed from elements (C, N, O, H, F, Si, S, Cl and Br) is also proposed using group contribution theory [14].

The refractive index n of a polymeric material is computed from functional groups as follows. From equations (2.10) and (2.9), the refractive index is given as:

$$n_{LL} = (\frac{M + 2\rho R_{LL}}{M - \rho R_{LL}})^{1/2} \tag{2.11}$$

and

$$n_{GD} = 1 + \frac{\rho R_{GD}}{M} \tag{2.12}$$

where M is the molecular weight of the repeating unit of polymer molecules.

From the above equations the value of n is defined by the combined effect of two key physical factors:

1. The value of n increases with increasing intrinsic refractive power of a material, as quantified by its molar refraction R. Since $R_{CH} < R_{CH_2} < R_{CH_3}$ [4], increasing contents of comonomers (butene, hexane and octane groups) will increase the molar refraction and therefore increase the refractive index n; on the other hand, increasing amount of total unsaturation will decrease the molar refraction and decrease the refractive index.
2. The value of n increases with amount of material per unit volume, as quantified by decreasing molar volume. Since crystalline polymers normally has higher density than amorphous polymers of the same molecular composition, higher crystallinity will result in an increase of the refractive index n.

R_{LL} and R_{GD} have relatively little dependence on temperature and percent crystallinity, while M/ρ changes significantly with changing temperature and/or crystallinity. $M/\rho(T)$ normally increases with increasing temperature and decreases with increasing crystallinity due to the change in density. Consequently, n normally decreases with increasing temperature and increases with increasing crystallinity.

The resins included in this study are polyethylene copolymers. Once the detailed information about the resin composition is known, the refractive index can be derived using the above relationships. For example, for the poly(ethylene-butene) copolymer, the molar refraction is given by:

$$R_{LL} = (1-P_{cm})R_{LL_{C_2H_4}} + P_{cm}R_{LL_{but}} + P_{tu}(R_{LL_{CH}} - R_{LL_{CH_3}}) \tag{2.13}$$

$$R_{GD} = (1-P_{cm})R_{GD_{C_2H_4}} + P_{cm}R_{GD_{but}} + P_{tu}(R_{GD_{CH}} - R_{GD_{CH_3}}) \tag{2.14}$$

where P_{cm} and P_{tu} are the mole percentage of comonomer and total unsaturation, respectively. Molar refractions R_{LL} and R_{GD} for ethylene, butene and carbon double bond are listed in [4]. In addition,

$$M = (1-P_{cm})M_{CH_2} + P_{cm}M_{but} \tag{2.15}$$

The refractive index is thus given by equation (2.11) and (2.12).

For Sample B in Table 2.1, a poly(ethylene-butene) resin. The molecular weight of the repeating unit M is given by:

$$M = (1-0.0403)\mathrm{C_2H_4} + 0.0403\mathrm{C_4H_8} = 29.0478$$

the molar volume v is given by:

$$v = \frac{M}{\rho} = \frac{29.0478}{0.9194} = 31.5943$$

The molar refraction for $-CH_2-$, $-CH_3$ and $=CH-$ groups are listed in [4]. The Lorentz-Lorenz molar refraction for these groups are 4.649, 5.644 and 3.616, respectively. The

Gladstone-Dale molar refraction for the same groups are 7.831, 8.82 and 6.80, respectively. The molar refractions for the monomers are:

$$\begin{aligned}
R_{LL} &= (1-P_{cm})R_{LL_{C_2H_4}} + P_{cm}R_{LL_{but}} + P_{tu}(R_{LL_{CH}} - R_{LL_{CH_3}}) \\
&= (1-0.0403)*(2*4.649) + 0.0403*(2*4.649+3.616+5.644)+ \\
&\quad (0.0286/1200)*(2*3.616-(4.649+5.644)) \\
&= 9.6711 \\
R_{GD} &= (1-P_{cm})R_{GD_{C_2H_4}} + P_{cm}R_{GD_{but}} + P_{tu}(R_{GD_{CH}} - R_{GD_{CH_3}}) \\
&= (1-0.0403)*(2*7.831) + 0.0403*(2*7.831+6.80+8.82)+ \\
&\quad (0.0286/1200)*(2*6.80-(7.831+8.82)) \\
&= 16.2914
\end{aligned}$$

The refractive index n of a polymeric material is computed from functional groups as follows. From equations (2.11) and (2.12), the refractive index is given as:

$$\begin{aligned}
n_{LL} &= (\frac{M+2\rho R_{LL}}{M-\rho R_{LL}})^{1/2} \\
&= (\frac{29.0478+2*0.9194*9.6711}{29.0784-0.9194*9.5711})^{1/2} \\
&= 1.5243 \\
n_{GD} &= 1+\frac{\rho R_{GD}}{M} \\
&= 1+\frac{0.9194*16.2914}{29.0478} \\
&= 1.5156
\end{aligned}$$

2.3 Experimental

2.3.1 Materials

The resins used in this study were supplied by Dr. Joo Teh from NOVA Chemicals, Calgary, Canada. Structural data regarding these resins were also supplied by NOVA Chemicals. The data are shown in Table 2.1. Also, films made from these resins, under similar conditions were supplied by NOVA Chemicals. The materials included in this study are provided by NOVA Chemicals (Calgary, AB). A number of polyethylene copolymer resins are employed. Detailed information on the resin compositions was provided by NOVA. Sample films included here were made by NOVA from these resins under similar processing conditions.

Table 2.1: Structural information of resins

Resin	Sample Number	Como Type	Como molar %	Density (g/cm^3)	Total Unsaturation	M (g/mol)	v (cc/mol)
B	P972403:978586	BUT	4.03	0.9194	0.0286	29.0	31.5
H	P971664:975866	BUT	3.8	0.919	0.06451	28.9	31.5
A	P972403:978585	HEX	3.94	0.9208	0.03792	30.1	32.7
C	P972403:978587	HEX	3.77	0.9234	0.03896	30.0	32.5
D	P972403:978582	HEX	3.08	0.9192	0.04474	29.6	32.2
E	N/A	HEX	2.56	0.9194	0.03245	29.3	31.9
M	P9807250:9807251	HEX	4.5	0.9192	N/A	30.4	33.1
G	P972403:978583	OCT	3.2	0.92	0.07435	30.6	33.2
I	N/A	OCT	5	0.907	0.07725	32.1	35.3
J	N/A	OCT	3.2	0.918	0.06524	30.6	33.3
L	P970268:970703	OCT	2.8	0.9212	N/A	30.2	32.8
F	P971351:974751	LDPE	N/A	0.9190	N/A	28	30.4
K	P971351:974752	LDPE	N/A	0.9203	N/A	28	30.4

Como: Comonomer. M: Molecular weight of the repeating Unit. v: Molar volume.

2.3.2 Traditional Methods

Three methods are commonly used in the measurement of the refractive index of plastic materials [15].

Refractometric Method

The refractometric method requires the use of the refractometer. The Abbé refractometer is the most widely used refractometer in practice. It requires a source of white light and a contacting liquid that will not attack the surface of the plastic. The contacting liquid must also have a higher refractive index than that of the plastic being measured. The test is carried out by placing a specimen in contact with the prism using a drop of contacting liquid. The polished edge of the specimen is kept towards the light source. The refractive index is determined by moving the index arm of the refractometer so that the field seen through the eyepiece is half dark. The compensator is adjusted to remove all color for the field. The value of refractive index is read out from the refractometer.

Becke Line Method

The Becke Line Method requires an optical microscope having a magnifying power of 200x [1] together with a range of liquids of known refractive index. The material to be tested is mounted in a liquid of known refractive index and examined in monochromatic light with the condenser adjusted to give a narrow axial beam. When the test pieces and the liquid have different refractive indices, each particle is surrounded by a narrow luminous halo (the Becke Line) which moves as focus is adjusted. If the focus is lower, then the Becke line moves towards the medium having the lower refractive index. The test is repeated with particles mounted in other immersion liquids until a match is found or until the index of the test sample lies in between two of the known indices in the series

---

[1] ISO R489

of liquid standards. If the Becke line phenomenon does not appear, then the refractive index of the material being examined is equal to that of the immersion liquid. The test pieces should have a thickness significantly less than the working distance of the 8 mm microscope objective. Its linear dimensions shall also be sufficiently small and so distributed that simultaneous observation of approximately equal areas of sample and surrounding field is possible.

Microscopic Method

The Microscopic method only requires a microscope of magnifying power of 200x or more. A specimen of convenient size, having a fair polish and two parallel surfaces, is used. The test is carried out by alternately focusing the microscope on the top and the bottom surface of the specimen and reading the longitudinal displacement of the lens tube accurately. The difference between the two readings is considered the apparent thickness of the specimen. The refractive index is determined by:

$$\text{Refractive index} = \frac{\text{Actual thickness}}{\text{Apparent thickness}} \tag{2.17}$$

Among these three methods, the refractometric method is more accurate since the other two methods require the precise focus point on the surfaces of the specimen, which is subject to the operator's skill.

2.3.3 Method of Transmission Spectrum

The method of transmission spectrum is employed here to determine the refractive indices of sample films. The transmission spectrum method was first introduced to calculate the refractive index, absorption coefficient and thickness of a thin layer of amorphous silicon on a substrate for the transmission interference fringes of the spectrum [16].

The transmission spectra of film samples are obtained using a Hewlett-Packard 8453 UV-Visible Spectrophotometer. The UV-Visible Spectrophotometer is able to measure the spectrum over a range of wavelengths from $200nm$ (UV) to $1100nm$, including the visible light spectrum $400nm \sim 800nm$. A section of the transmission spectrum of film sample A is shown in Figure. 2-1. The interference fringes are the peak formations on the spectrum.

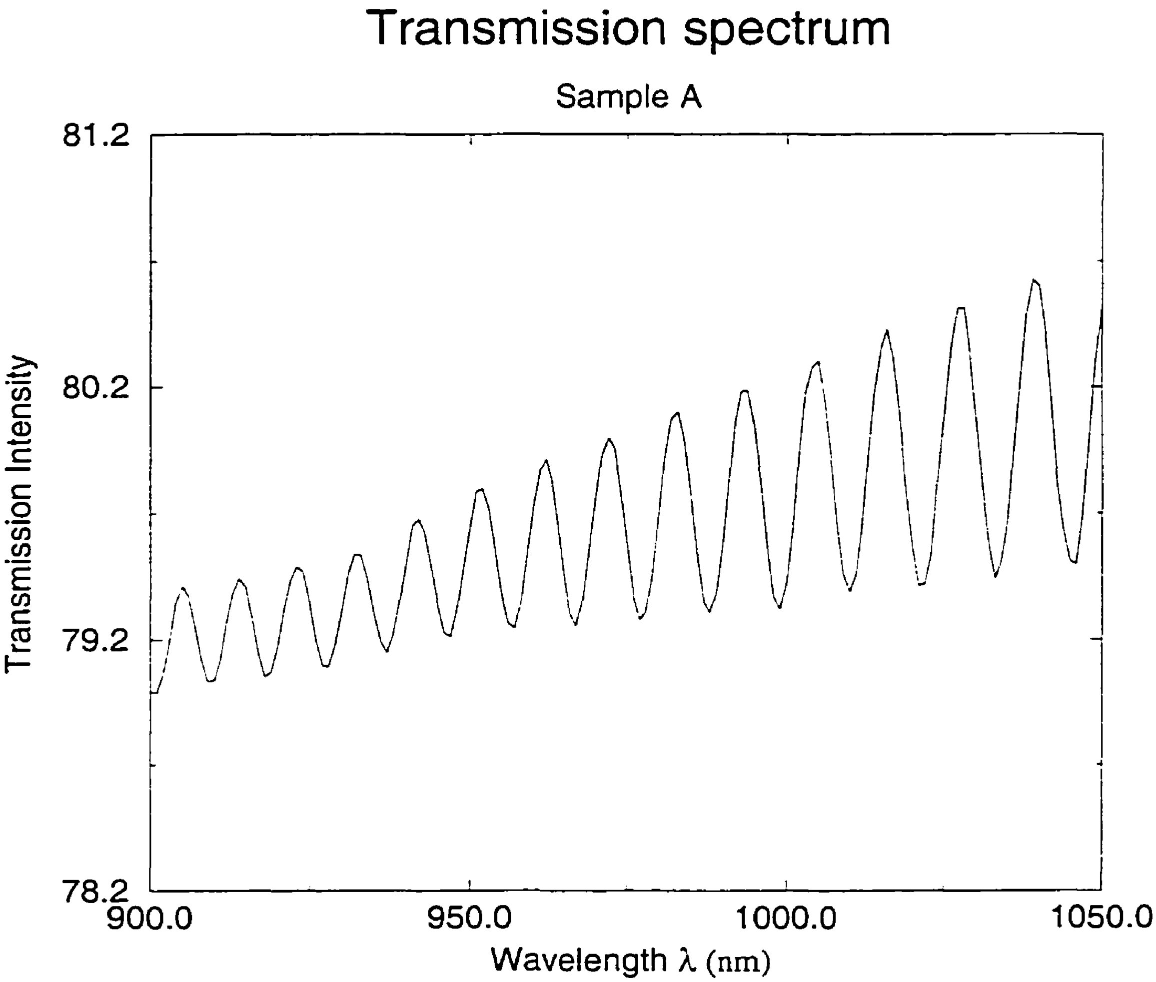

Figure 2-1: Transmission spectrum of Sample A

Assuming a film of thickness d and refractive index n, the basic equation for interference fringes is

$$2nd = m\lambda \tag{2.18}$$

where m is the order number, which is an integer for maxima and half integer for minima; λ is the corresponding wavelength. The transmission spectrum can be expressed as [16]:

$$T = \frac{Ax}{B - Cx\cos\phi + Dx^2} \tag{2.19}$$

where

$$\begin{aligned} A &= 16n^2 s && (2.20)\\ B &= (n+1)^3(n+s^2) && (2.21)\\ C &= (2(n^2-1)(n^2-s^2) && (2.22)\\ D &= (n-1)^3(n-s^2) && (2.23)\\ \phi &= \frac{4\pi nd}{\lambda} && (2.24)\\ x &= exp(-ad) && (2.25) \end{aligned}$$

Here, a is the absorption coefficient and s is the refractive index of the substrate that supports the sample film. In this case, the substrate is BK7 glass, so $s = 1.5185$ at $n = 550nm$. The extremes of the interference fringes can be written as

$$\begin{aligned} T_M &= \frac{Ax}{B - Cx + Dx^2} && (2.26)\\ T_m &= \frac{Ax}{B + Cx + Dx^2} && (2.27) \end{aligned}$$

where T_M and T_m are the maxima and minima on the transmission spectrum. Next, T_M and T_m are to be transformed into continuous functions of wavelength λ, and thus of $n(\lambda)$. This transformation is achieved by fitting all T_M values with a smooth curve, usually polynomials, such that T_M will have a value for each and every value of λ. Similarly, a curve of the same order is fitted to all T_m values.

From equations (2.26) and (2.27), we have:

$$\frac{1}{T_m} - \frac{1}{T_M} = \frac{2C}{A} \tag{2.28}$$

Solving this equation for n gives:

$$n = [N + (N^2 - s^2)^{1/2}]^{1/2} \tag{2.29}$$

and

$$N = 2s\frac{T_M - T_m}{T_M T_m} + \frac{s^2 + 1}{2} \tag{2.30}$$

Equation (2.29) can be used to derive the refractive index.

Once $n(\lambda)$ is known, x can be calculated in a variety of ways. Solving for x by T_M from equation (2.26) gives:

$$x = \frac{E_M - [E_M^2 - (n^2 - 1)^3(n^2 - s^4)]^{1/2}}{(n - 1)^3(n - s^2)} \tag{2.31}$$

where

$$E_M = \frac{8n^2 s}{T_M} + (n^2 - 1)(n^2 - s^2) \tag{2.32}$$

Similarly, solving for x using T_m from equation (2.27) gives:

$$x = \frac{E_m - [E_m^2 - (n^2 - 1)^3(n^2 - s^4)]^{1/2}}{(n - 1)^3(n - s^2)} \tag{2.33}$$

where

$$E_m = \frac{8n^2 s}{T_m} - (n^2 - 1)(n^2 - s^2) \tag{2.34}$$

Combining these two solutions, one arrives at,

$$x = \frac{F - [F^2 - (n^2 - 1)^3(n^2 - s^4)]^{1/2}}{(n-1)^3(n - s^2)} \tag{2.35}$$

where

$$F = \frac{8n^2 s}{T_i} \quad \text{and} \quad T_i = \frac{2T_M T_m}{T_M + T_m} \tag{2.36}$$

From the values of x, the absorption coefficient $a(\lambda)$ can be obtained using equation (2.25).

In Figure 2-1, the interference fringes are defined by:

T_M and λ_{max}: transmittance and wavelength of maxima

T_m and λ_{min}: transmittance and wavelength of minima

These data must be corrected because of the slit width of the spectrophotometer: l. The HP 8453 UV-Visible spectrophotometer has a slit width of $l = 1nm$.

$$T_{Mcor} = T_{Mexp} + (T_{Mexp}\frac{l}{w_M})^2 \tag{2.37}$$

$$T_{mcor} = T_{mexp} - (T_{mexp}\frac{l}{w_m})^2 \tag{2.38}$$

and

$$w_{M(i)} = \lambda_{min_{i-1}} - \lambda_{min_{i+1}} \tag{2.39}$$

$$w_{m(i)} = \lambda_{max_{i-1}} - \lambda_{max_{i+1}} \tag{2.40}$$

In the following discussion, T_M and T_m refer to the corrected values. The envelopes of T_M and T_m are computed as follows. For each value of λ_{max}, a T_m is interpolated from all of the λ_{min} and T_m pairs using a $5th$ order polynomial. The values of T_M at each λ_{min} are obtained using the same method. So, for all the values of λ_{max} and λ_{min}, both T_M and T_m values are available. Hence T_M and T_m are continuous functions of wavelength λ. Figure 2-2 shows both the values of the measured transmission spectrum of Sample

A and the corrected transmission spectrum.

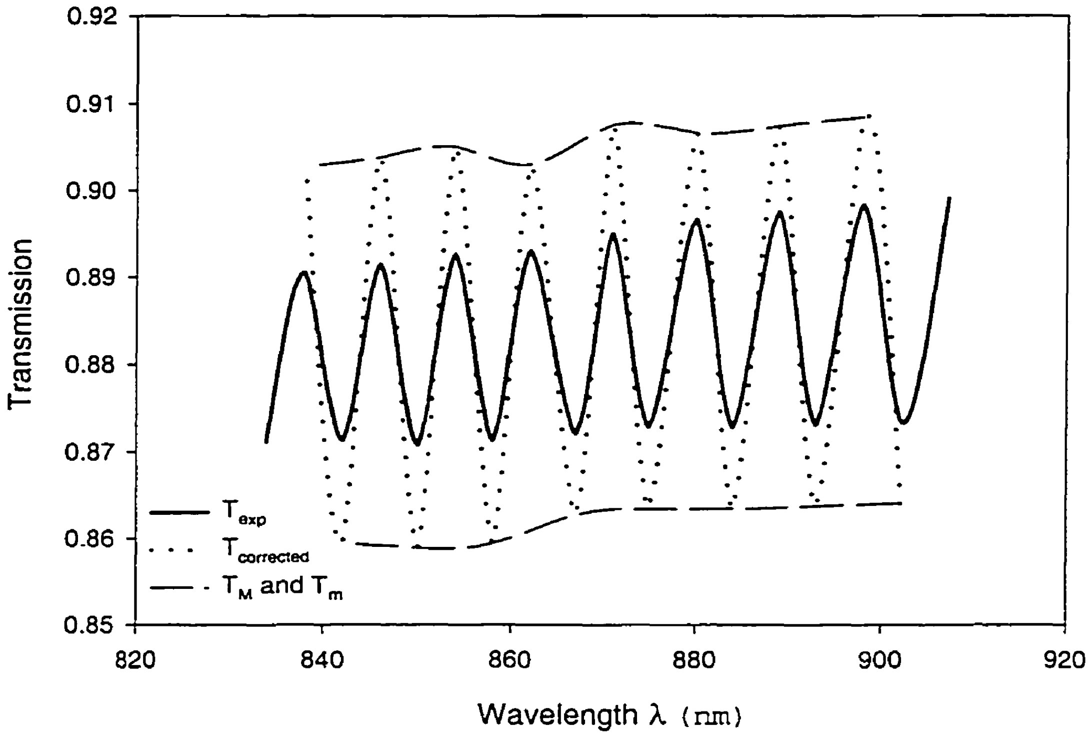

Figure 2-2: Transmission intensity and Transmission intensity corrected by slit width of the spectrophotometer as functions of wavelength

The refractive index of the film is thus given by equation (2.29). Using the least-square method, the obtained values of n at different wavelength are fitted to the curve

$$n = n_0 + (\frac{a_d}{\lambda})^2 \tag{2.41}$$

where n_0 is the refractive index at infinite wavelength and a_d is by definition the dispersion of the curve.

The thickness of the film can be derived independently from the transmission spectrum as well, using equation (2.17).

$$d = \frac{\lambda_1 \lambda_2}{4(\lambda_1 n_2 - \lambda_2 n_1)} \tag{2.41}$$

with $\lambda_1 > \lambda_2$. Thickness d is expected to be constant and does not depend on wavelength.

To increase the accuracy of computation, more iterations to compute the refractive index n and the thickness d are performed. From equation (2.17), the order of interference m is:

$$m = \frac{2nd}{\lambda} \tag{2.42}$$

and m is an integer for maxima, and half integer for minima. When m is known, the thickness can also be obtained as:

$$d_2 = \frac{m\lambda}{2n} \tag{2.43}$$

The average of d_2 is taken as the thickness of the film. m is thus taken when the difference between d and d_2 reaches minimum. From the values of m and d_2, we have:

$$n_2 = \frac{m\lambda}{2d_2} \tag{2.44}$$

Table 2.2 shows the values of T_M and T_m after being corrected by the slit width of the spectrophotometer. The values of n and n_1 are functions of wavelength. The thickness is determined independently at each wavelength. As can be seen, the thickness d_2 shows a large improvement from d. The standard deviation decreased from $3755nm$ to $27nm$. This is achieved by finding the right order number m such that σ_{d_2} is minimum.

A general flow chart of the computation steps is shown in Figure 2-3.

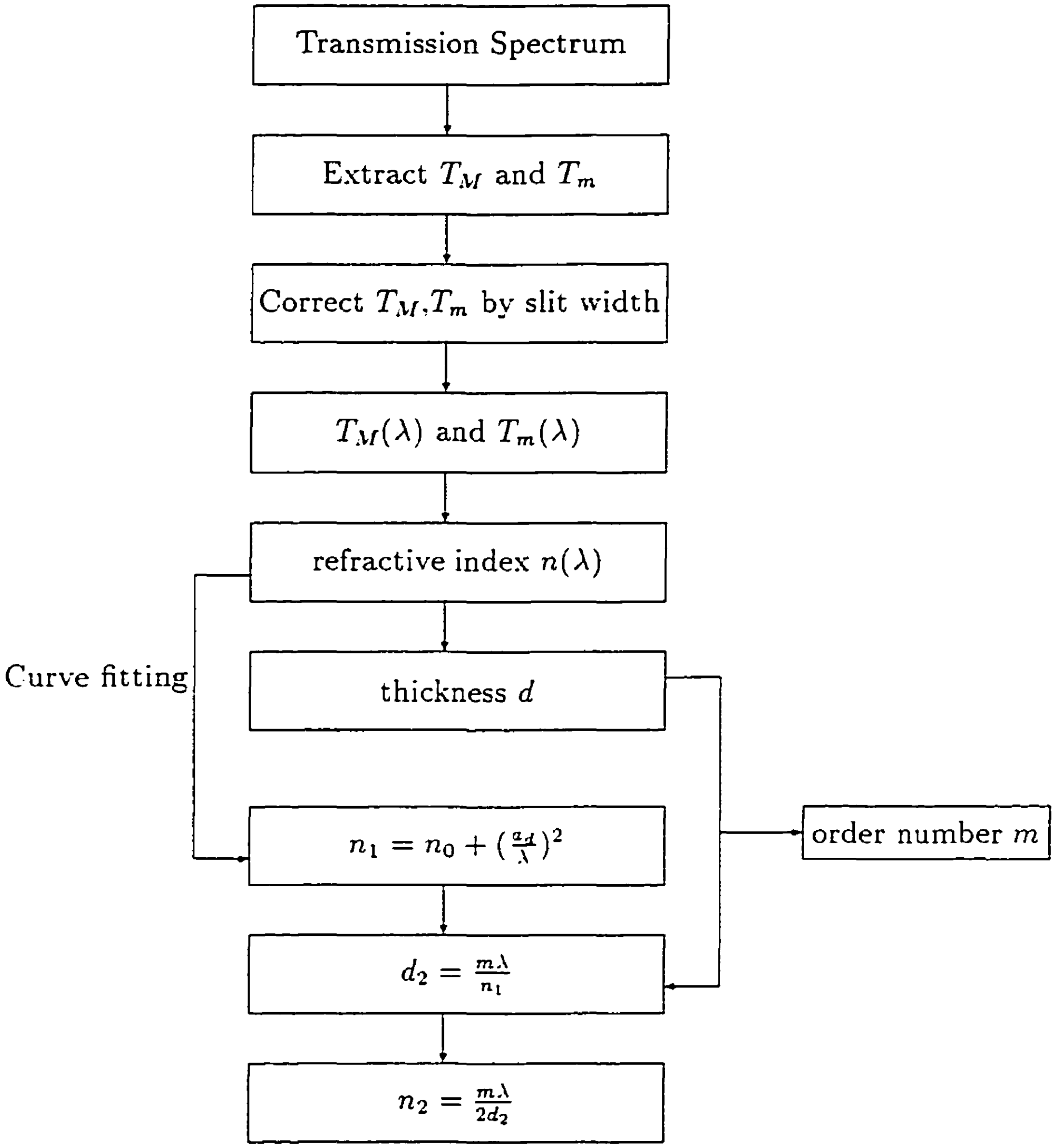

Figure 2-3: Flow chart of the computation of the refractive index from transmission spectra

Table 2.2: Values of λ, T_M and T_m for the spectrum of Figure 2-1. Calculation of n and d.

λ	T_M	T_m	n	d	m	d_2	n_2
881	0.7988	0.7846	1.516	33.52	94	27.32	1.513
877	0.7983	0.7843	1.515	28.10	94.5	27.35	1.513
872	0.7978	0.7841	1.514	34.91	95	27.35	1.513
868	0.7974	0.7839	1.512	33.49	95.5	27.38	1.514
864	0.7970	0.7838	1.512	31.50	96	27.40	1.514
860	0.7967	0.7836	1.511	23.32	96.5	27.42	1.514
855	0.7964	0.7833	1.511	27.09	97	27.40	1.514
851	0.7961	0.7829	1.511	25.71	97.5	27.40	1.514
847	0.7959	0.7826	1.512	24.85	98	27.39	1.514
843	0.7956	0.7821	1.513	24.60	98.5	27.37	1.514
839	0.7954	0.7817	1.514	25.15	99	27.36	1.514
835	0.7951	0.7813	1.515	26.83	99.5	27.35	1.514
831	0.7947	0.7809	1.515	30.48	100	27.34	1.514
827	0.7943	0.7807	1.514		100.5	27.36	1.514

d_{ave}=28.43μm σ_d= 3.75μm d_{2ave}=27.4μm σ_{d_2}=27nm

The dependence of x on wavelength λ is determined from experimental data for T_M and T_m by equation (2.34). The absorption coefficient as a function of wavelength $a(\lambda)$ can be calculated from $x(\lambda)$ and the thickness d from equation (2.24):

$$a = -\frac{\log x}{d} \tag{2.45}$$

The computed value of a for sample A from the spectrum in Figure 2-1 is listed in Table 2.3.

Once a is known, the extinction coefficient κ, in the absence of light scattering, is determined by:

$$\kappa = \frac{a\lambda}{4\pi} \tag{2.46}$$

Table 2.3: Values of E_M and x for the spectrum of figure 2-1. Calculation of absorption coefficient a.

E_M	x	a (μm^{-1})	
39.804	0.8802	4.671E-06	
39.845	0.8796	4.694E-06	
39.881	0.8791	4.710E-06	
39.914	0.8786	4.723E-06	
39.948	0.8782	4.738E-06	
39.985	0.8776	4.755E-06	
40.023	0.8771	4.776E-06	a_{ave}=4.78E-6
40.062	0.8765	4.800E-06	
40.101	0.8760	4.826E-06	
40.129	0.8756	4.841E-06	
40.156	0.8753	4.860E-06	
40.171	0.8753	4.869E-06	
40.169	0.8756	4.858E-06	
40.144	0.8765	4.829E-06	

2.4 Results and Discussions

Figure 2-4 shows another measurement of the transmission spectrum of sample A. The computation based upon this measurement is listed in Table 2.4

Each film sample is measured over a different area. The calculation for each measurement is made following the same procedure. All measurements of the transmission spectra of samples films are listed in the Appendix A. The computation of refractive indices are also listed in corresponding tables.

Based on the structural information listed in Table 2.1 and the computation method described in Section 2.2.4, the refractive indices for all resins were calculated. The predicted values are shown in Table 2.5.

The final values of the refractive index are the average of the results from each measurement. Comparison between the refractive index derived from the chemical composition of the resins with that obtained from the experimental measurements is made in

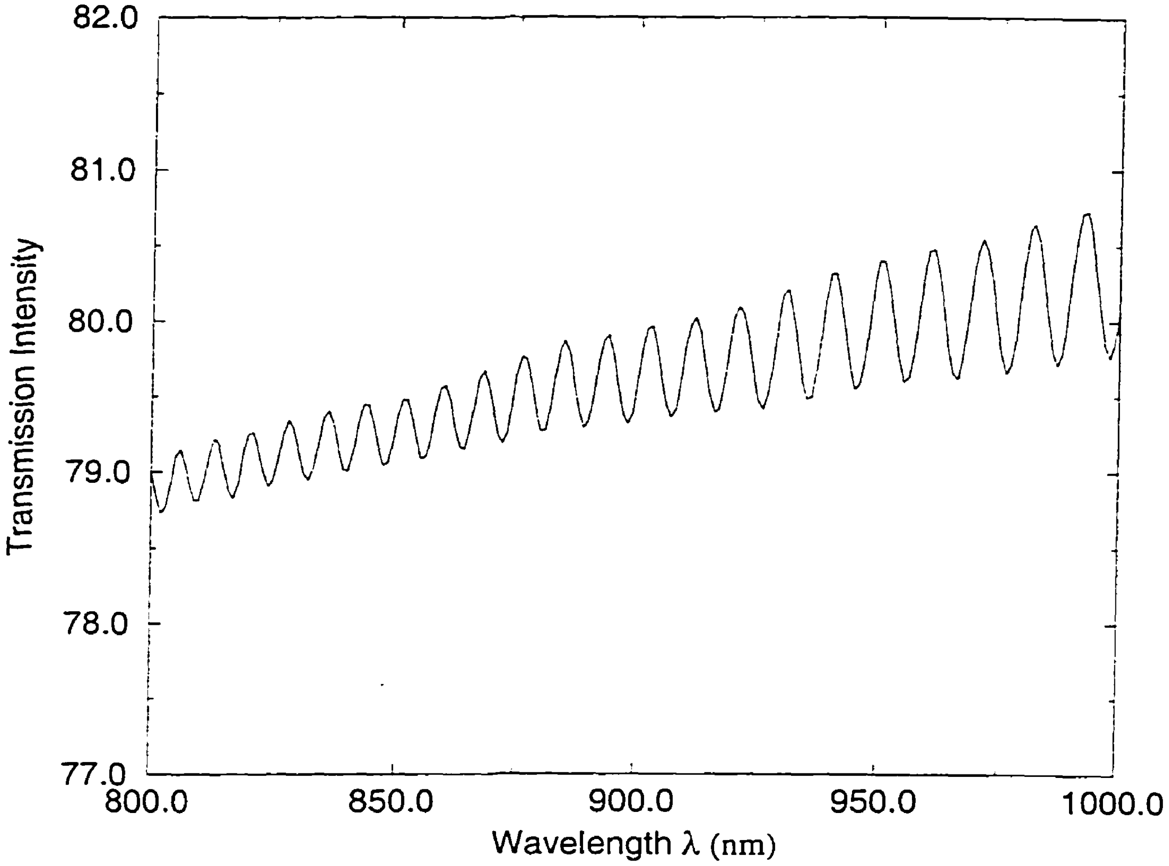

Figure 2-4: Transmission spectra of Sample A

Table 2.4: Values of λ, T_M and T_m for the spectrum of Figure 2-4. Calculation of n and d.

λ	T_M	T_m	n	d	m	d_2	n_2
961	0.8100	0.7900	1.511	27.87	87	25.78	1.513
955	0.8105	0.7897	1.514	23.65	87.5	25.72	1.513
950	0.8105	0.7894	1.515	25.04	88	25.70	1.513
945	0.8102	0.7890	1.516	32.24	88.5	25.70	1.513
941	0.8099	0.7886	1.517	21.74	89	25.73	1.513
935	0.8094	0.7880	1.517	32.49	89.5	25.70	1.514
931	0.8090	0.7877	1.517	25.66	90	25.73	1.514
926	0.8086	0.7872	1.518	25.17	90.5	25.73	1.514
921	0.8083	0.7868	1.518	24.65	91	25.72	1.514
916	0.8080	0.7865	1.518	30.26	91.5	25.74	1.514
912	0.8078	0.7862	1.519	23.83	92	25.73	1.514
907	0.8076	0.7859	1.519	29.41	92.5	25.75	1.514
903	0.8074	0.7856	1.520	23.30	93	25.74	1.514
898	0.8072	0.7853	1.520		93.5	25.73	1.514

d_{ave}=25.79μm σ_d= 4.07μm d_{2ave}=25.73μm σ_{d_2}=20nm

Table 2.5: Refractive indices computed from structural information using Lorentz-Lorenz and Gladstone-Dale relationships

Resin	R_{LL}	R_{GD}	n_{LL}	n_{GD}
B	9.6711	16.2914	1.5243	1.5156
H	9.6497	16.2554	1.5239	1.5153
A	10.0291	16.8944	1.5251	1.5163
C	9.9975	16.8412	1.5268	1.5178
D	9.8695	16.6254	1.5237	1.5152
E	9.7730	16.4627	1.5237	1.5151
M	10.1331	16.0697	1.5242	1.5156
G	10.1892	17.1640	1.5243	1.5156
I	10.6906	18.0090	1.5161	1.5089
J	10.1892	17.1640	1.5229	1.5145
L	10.0780	16.9764	1.5250	1.5162
F	9.298	15.662	1.5224	1.5140
K	9.298	15.662	1.5233	1.5148

Table 2.6. Because the molar refractions are available at $\lambda = 589nm$, all of the refractive indices are computed at this wavelength. Since the dispersion a_d is comparatively small at different wavelengths, n does not change greatly over different wavelengths in the visible spectrum as shown in Table 2.2 and Table 2.4.

As shown in Table 2.6, the predictions of the Lorenz-Lorentz relationship and the Gladstone-Dale relationship are fairly close to each other. Of all the resins, B and H are poly(ethylene-butene); A, C, D, and E are poly(ethylene-hexane); G, I and J are poly(ethylene-octane). The compositions for samples in the same group are very similar to one another, hence, the refractive indices are also very close. When comparing with experimental measurements, agreement within ±2% is generally found, with the exception of sample J. The instrument error is estimated at ±1%. The main reason for the discrepancy, aside from the instrument error, is the variance in thickness of the film. Since the polyethylene films in the study are quite soft, it is difficult to keep the film perfectly flat on the focal plane of the spectrophotometer during measurements without any stretching. For very soft film such as sample J, the variance in thickness due to stretching is more significant than those of the stronger films. By using a glass slide as support, the effect of streching has been greatly reduced in most cases. It cannot, however, completely eliminate the stretching for sample J because of its softness. Hence, the error in the measurements of sample J is larger than those of the other films.

For future calculation of gloss, light transmission and haze presented in later sections, the experimental data of refractive indices are used.

2.5 Summary

The refractive index is the most important optical property of polymer films and the foundation to other optical properties. Unlike transparency and gloss, it is not influenced by the processing conditions during the manufacturing, but is only a function of the

Table 2.6: The refractive indices of resins at $\lambda = 589nm$

Sample	n_{LL}	n_{GD}	n_{exp}	$a_{exp}\ m^{-1}$
B	1.52	1.52	1.53	4.58
H	1.52	1.52	1.50	5.55
A	1.53	1.52	1.54	5.00
C	1.53	1.52	1.50	5.70
D	1.52	1.52	1.51	2.13
E	1.52	1.52	1.50	6.97
G	1.52	1.52	1.51	3.68
I	1.52	1.51	1.51	6.46
J	1.52	1.51	1.57	5.81
L	1.52	1.52	1.52	4.54

composition of the resin. Once the properties of the resin are known, refractive index can be estimated from available group contribution theories. The important factors in determining the refractive index of a polymer material are the chemical composition, i.e. the monomer and comonomer, comonomer percentage, total unsaturation and the density. For LLDPE, high crystallinity leads to higher density and lower molar volume, if all other parameters are made constant. This decrease in molar volume will increase the refractive index n. Furthermore, increasing comonomer contents will increase the molar refraction R, which leads to larger values of n. On the other hand, increasing total unsaturation will decrease the molar refraction and decrease the refractive index.

Notice here that the molecular weight, M_w, polydispersity, M_w/M_n and chain branching of the polymer are not directly included in the group contribution theory. Although the influence of these parameters on the refraction by polymer materials still awaits further study, it is possible to qualitatively speculate from the crystallization point of view. For crystalline polymers, such as polyethylene, polyethylene copolymers and polypropylene, M_w, M_w/M_n and long chain branching have a strong influence in the crystallization during solidification. Since the density of the final product is dependent upon crystallinity and is a strong factor in group contribution theory, the refractive index is indirectly being influenced by M_w, M_w/M_n and chain branching. However, whether the density alone can account for the influence of M_w, M_w/M_n and chain branching in determining the refractive index is not certain. Further study in this area requires advanced understanding of crystallization kinetics and the effects of molecular weight, polydispersity and chain branching on the refractive index.

In addition, the Method of Transmission Spectrum is adopted to measure the refractive indices of sample films. The results show good agreement with predictions based upon the chemical compositions of resins. The advantage of this method lies in its simplicity in operation and sample preparation. The formulations are rigorous and in closed form. In addition, it provides a method to determine the thickness of the sample film independently. It can either serve as a method of measuring thickness for very thin films or as a validation of the results of refractive index when comparing to the known thickness of film.

Chapter 3

Morphology of Polyethylene Blown Films

3.1 Introduction

Morphology of polythethylene blown films is the center of this study. It serves as the intermediate step between molecular structure and the macroscopic physical properties. The goal here is to determine the surface and the bulk morphologies of the sample films included in this study using various microscopy methods. In addition, various characterization methods are applied to quantitatively describe the morphology of sample films. These characteristics will not only be used in determining the light reflection and transmission behavior of the sample films but also provide parameters in future studies to describe the morphology development as a result of molecular structure and thermo-mechanical history during the film blowing process.

3.2 Apparatus

The apparatus used in the characterization of film morphology is the TopoMetrix Aurora 2100 Near-field Scanning Optical Microscope/Atomic Force Microscope, shown in Figure 3-1, including the laser source, microscope and viewing monitor. The microscope is placed on an air-pressure table for vibration isolation. The air pressure of the table is maintained at 100 psi. Figure 3-2 shows the layout of the microscope. The scan sizes of this apparatus range from $1\mu m \times 1\mu m$ to $35\mu m \times 35\mu m$. The maximum resolution of the scan can attain 1000 lines per μm.

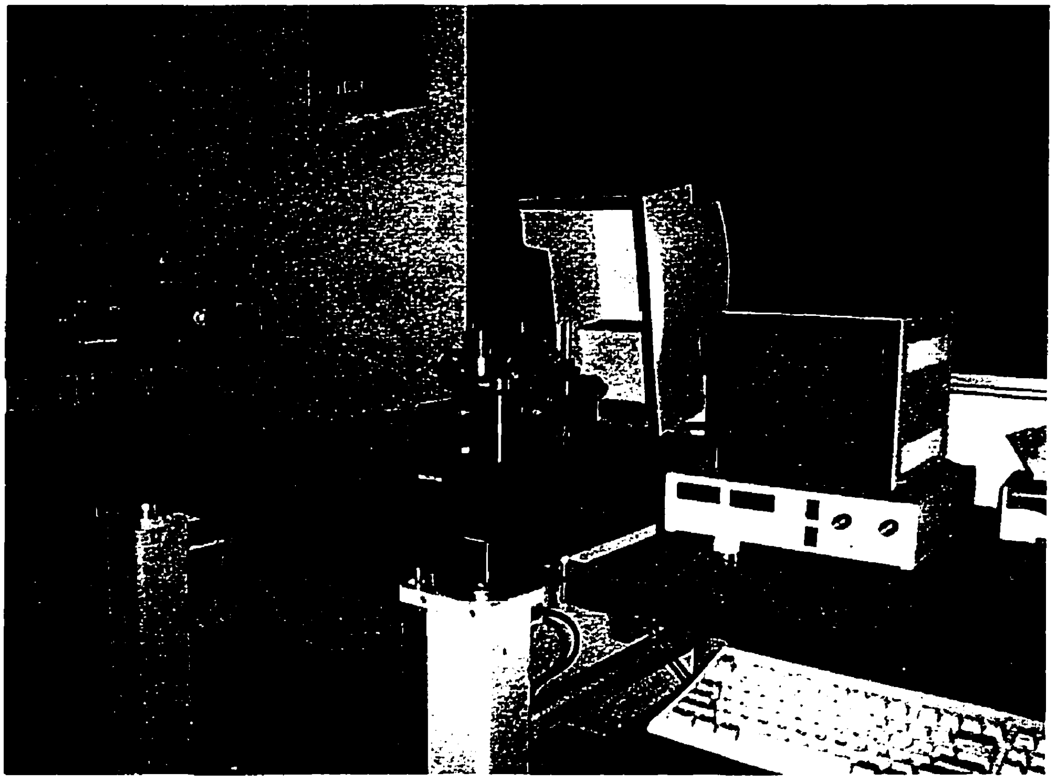

Figure 3-1: Experimental setup, including laser source, microscope and viewing monitor

The concept of near field scanning optical microscopy was first proposed in 1986 by IBM Zürich [17] and at Cornell University [18]. Near-field scanning optical microscopy

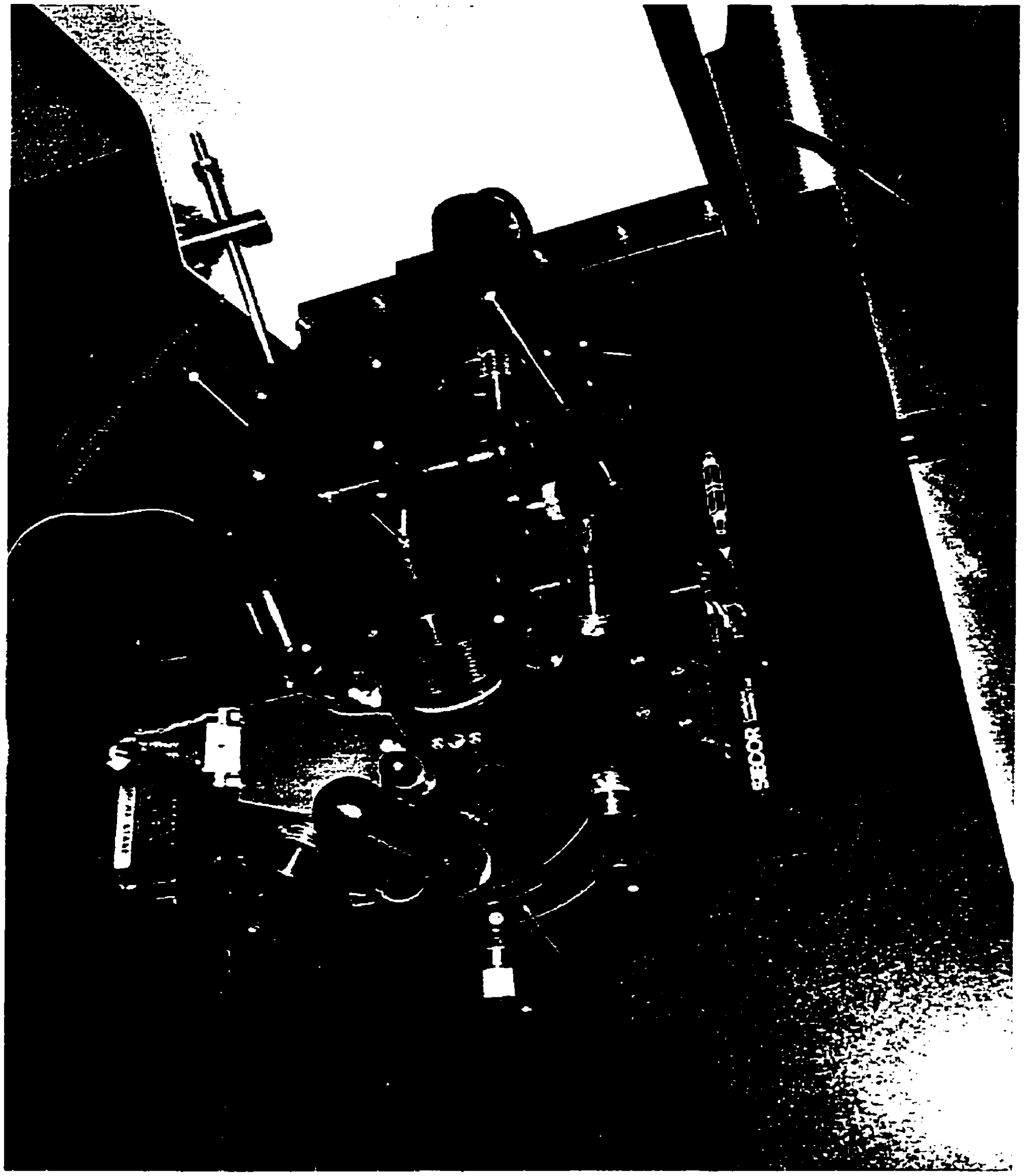

Figure 3-2: TopoMetrix Aurora 2100 NSOM/AFM apparatus mounted on a compressed air vibration-isolation table from Integrated Dynamics Engineering

(NSOM) allows the user to map the optical appearance of a sample using a probe that is smaller than the wavelength of visible light. It breaks the diffraction barrier so that a person can see features that are smaller than wavelength of visible light and thus are invisible in conventional optical microscopes [19]. The resolution of NSOM is limited primarily by the probe size and the probe to sample separation. The probe is a very sharp tip made from single-mode fiber optic. The aperture is $\sim 50nm$. The fiber optic is coated with aluminum to prevent light loss, thus ensuring a focused beam from the tip.

In order to expand the NSOM capability to samples with arbitrary surfaces, a distance regulating system must be employed to ensure that the tip-to-sample separation distance is sufficiently small to allow near-field imaging. In the Aurora system used in this study. a shear-force feedback system is used.

Shear-Force Feedback

To analyze a sample in the optical near field, the aperture of the optical fiber used to illuminate the sample must be brought into close proximity of the sample. Because most samples exhibit some topography, a feedback mechanism, which maintains a constant tip to sample distance, has to be used. In 1992 two groups proposed independently a method known as shear-force microscopy, as shown in Figure 3-3 [19][20]. This method has become the standard for NSOM. The Aurora system is built following the same concept. Practically all NSOM publications up to now have been done on instruments using the shear-force distance regulation method.

As shown in Figure 3-4, the tip of the fiber is mounted on a rigid vertical piezo, unlike the cantilever used in normal Atomic Force Microscopy. In contrast to ordinary Shear Force Microscopy, the spring constant is low parallel to the surface and high perpendicular to it. Consequently, when a dither piezo is used to drive the probe at or near its resonance frequency, very small shear forces between the tip and the sample can produce a resonance shift sufficient to generate substantial changes in the amplitude and phase of oscillation.

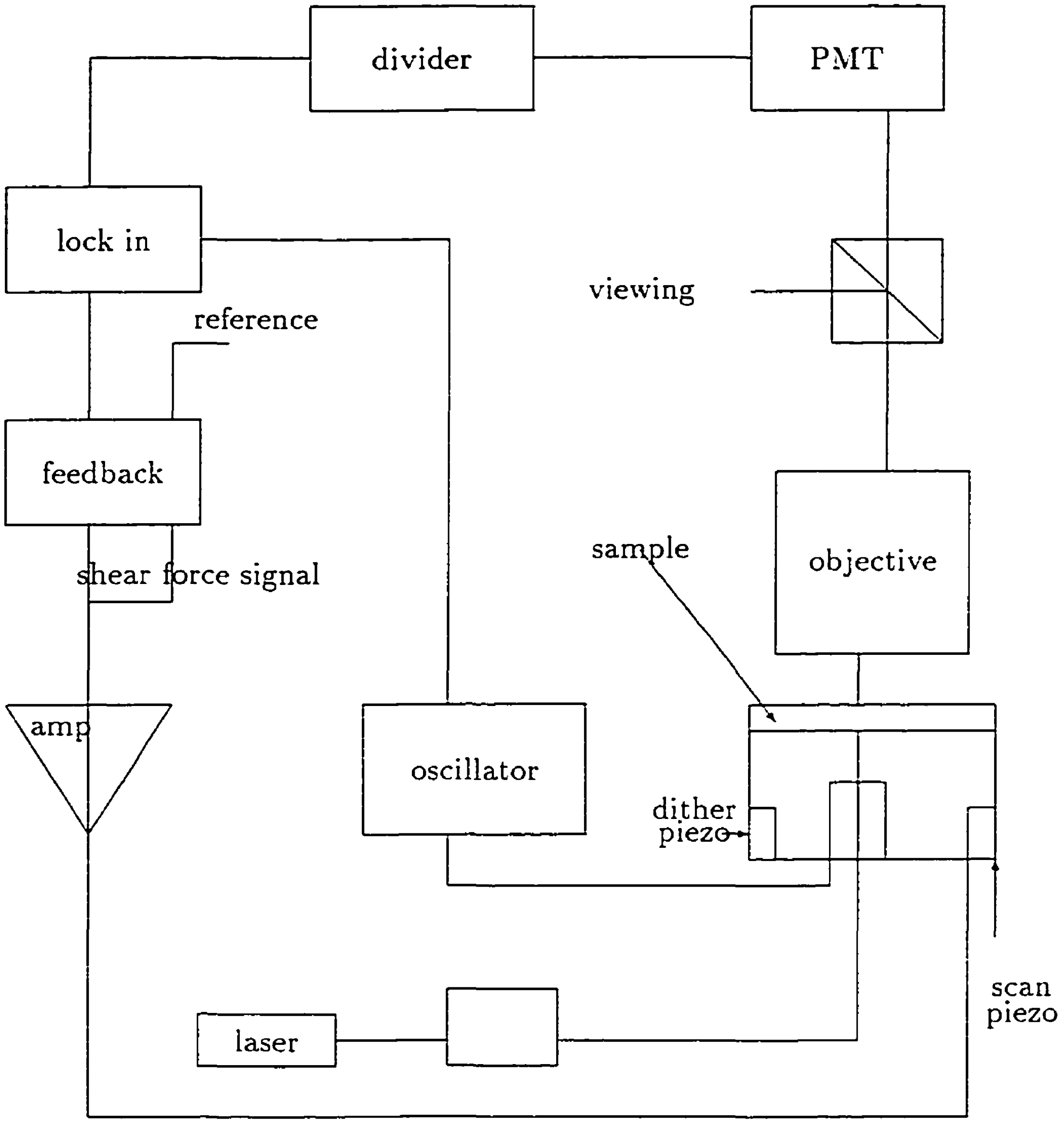

Figure 3-3: Schematic of a combined shear force and near-field scanning optical microscope.

This change can be measured optically [19] or non-optically. The most reliable and commonly used non-optical sensor incorporates a tuning fork [21]. Here the probe is attached to a tuning fork. Any change caused by surface-to-tip interactions is measured electrically. The advantages over the optical method are i) lack of interference between the feedback laser with the observation light, ii) no time consuming adjustments, and iii) higher sensitivity. In the Aurora system, the amplitude dampening or phase shift while the probe is oscillated at its resonance frequency are recorded by projecting a magnified image of the light reflected off the tip onto a position sensitive detector. In operation, a guidance laser ($633nm$) is shined on the tip during the scan. The reflection off the tip is collected by a photo detector. The reflected intensity is detected by the four quadrants of the photo detector and the direction of changes is accurately produced. The resulting ac signal can be normalized and demodulated to yield an amplitude and/or phase sensitive signal. This signal is then compared with a reference level in a standard feedback circuit linked to the vertical motion of the scan piezo. The system will then adjust the absolute probe position to maintain a constant shear force and, presumably, a fixed relative distance from the sample. The change in amplitude is monotonic with the distance and can be used for distance regulation. Although the name suggests some highly destructive mechanism, it is actually a non-contact technique [22], and therefore very gentle. Hard samples, like glass, can be scanned for hours without any damage to the fragile aperture. At the same time, the tip will not cause any damage or modification to the surface morphology of the soft sample films. Another advantage is that while the system is able to determine the surface profile of a sample by tracing the tip position and movement, light emitted from the aperture will pass through the sample and be picked up by the Photonmultiplier tube (PMT) at the same time. The PMT has a filter of $488nm$ to clear all of the ambient noise. The resulting dc signal from the PMT can be used to generate the NSOM image. This mechanism can be simultaneously used for both near-field and shear-force microscopy, or for shear force imaging alone.

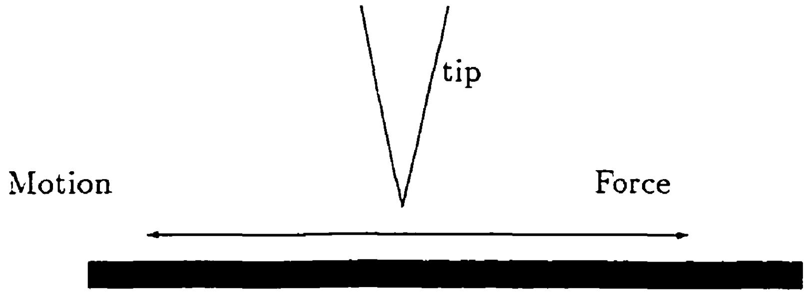

Figure 3-4: Tip oscillating horizontally above a surface, i.e. shear-force motion

Surface Imaging

For AFM imaging, the apparatus behaves similarly to ordinary shear-force microscopy. The resolution and accuracy of the surface profile is determined by the scan rate and scan size. For NSOM imaging, the achievable resolution degrades with increasing distance from the probe [23]. Thus, although it may be possible to obtain super-resolution information in three dimensions within a few tens of nanometer of the surface, more deeply buried structures in transmissive samples can not be sufficiently studied using NSOM without using the optical sectioning techniques of conventional optical microscopy. For this reason, the NSOM images only show the top layer of the surface structure.

Sample Thickness

The boundary conditions that exist in the immediate vicinity of the probe play a dominant role in determining both the resolution and contrast in NSOM, because they determine the degree to which the electro-magnetic energy in the near field is coupled to the far-field detector. Consequently, high-resolution surface information can be obtained in transmission even from thick specimens [24].

Flat Surface Condition

Since the probe is controlled by a distance regulation system, the shear-force feedback system that reacts to the atomic force between the surface and the probe can accurately trace the profile of the surface to maintain constant distance. As a result, the relative z height of the surface roughness cannot be determined from NSOM images. However, the geometrical characteristics of these roughness such as size, shape and aggregation or clustering, can be seen clearly using NSOM. The surface height profile is provided by shear-force imaging.

Detailed technical information regarding this instrument is listed below.

Photonmultipler Tube

Cathode: Bi-Alkali detector

Voltage: 0 to 1200 V

NSOM Probe

Type: Single-mode fiber optic

Diameter: 125 μm

Aperture: 50 nm (nominal)

Output: 10nW (nominal)

Force Feedback

Detection: Phase

Frequency: 45 to 120 kHz

Resolution: 1 nm vertical

Tip-to-sample Separation: 2 to 15 nm

X-Y Sample Positioner

Type: Piezoelectric

Travel: 7 mm, X and Y

Resolution: 0.1 μm

Laser Excitation Source
Type: Argon ion
Wavelength: 488 nm
Output power: 15 mW
Power source: 100 to 120 V, 10 A, 50 to 60 Hz
Cooling: Air

3.2.1 Experimental Techniques

Samples for AFM/NSOM scanning are cut from the sheets of films into $10mm \times 3mm$ sections. They are then placed on a drop of embedding liquid on a glass slide. The purpose of having embedding liquid is to prevent the sample from sliding while being scanned and to eliminate air pockets trapped beneath the sample. The type of liquid being used as embedding media is determined after many trials of different kind of liquid. The selection of embedding liquid is also very important in eliminating the static charges on the sample surface. In this work, a leak detection compound from Cantesco, CA is used as the embedding media for most sample films. The embedding media contains mostly non-ionic surfactant. The sample is then placed on the scanning stage of the apparatus and ready for AFM imaging.

First of all, the guidance laser (Photo Diode laser $633nm$) that controls the feedback is focused on the tip of the scanning probe. The direction of the photo detector is then adjusted to maximize the sensor feedback from the reflection by the tip. The next step is to establish the resonance frequency of the scanning probe. This is achieved by scanning the frequency space from 45 kHz to 120 kHz. The resonance frequency is the one that gives the maximum sensor feedback. The resonance frequency is different for each probe and can also change due to different probe-sample interaction, which requires the resonance frequency to be determined each time when either the probe or the sample is changed. Once the resonance frequency is determined, the probe is then lowered to the surface of the sample and entered into feedback.

Once the probe is stabilized in feedback, it is then possible to start line scan for any line in the area of interest. During the line scan, the probe will repeatedly scan over one single line. The purpose of line scan is to allow user to adjust the feedback control parameters such as proportional, integral and derivative, so that the surface profile is repeatable and accurate. In addition, the proper scan rate and scan range are determined at this stage. This is when various artifacts in AFM imaging occur. These artifacts are discussed in detail in the following section with respect to their origin. When the line scan is stable and repeatable for a randomly selected line, the surface scan can start. The result is monitored in real time and recorded in the end.

Because of the high-sensitivity of the instrument, this seemingly simple procedure can be complicated by a wide range of factors. The most common problem in AFM imaging is the artifacts caused by various sources. It is imperative to identify these artifacts and eliminate them to ensure the authenticity of the image. The main sources for the artifacts are probe geometry and non-ideal performance of piezoelectric ceramics, which are used in controlling the probe position and move the sample for raster scanning and static electric charges.

Probe Geometry

When imaging steep or thin convex features, the sharpness of the probe tip has a significant effect on the image. A probe with a large radius will begin to interact with the surface features well before the center axis of the probe reaches the feature. After the probe begins to interact with the feature it traces a rounded edge rather than a sharp edge. Furthermore, the image will be much wider than the actual sample.

Another kind of artifact associated with tip geometry is tip asymmetry. If the probe is not uniform, artifacts will be seen in the resulting image. For instance, a spherical shape of a surface domain may appear elongated if the shape of the tip is asymmetrical. Normally for asymmetrical tip, the artifact is independent to the direction of scanning. Therefore this artifact can not be eliminated by changing scanning direction.

To correct this artifact, repeated experiments on the same sample are done using different probes. The shape of probe tip is also closely monitored during the scanning to ensure the sharpness and symmetry at the tip.

Piezoelectric Ceramics and Scanner Stage

The mechanical construct of the AFM/NSOM apparatus can introduce artifacts to images as well. These distortions can be separated into horizontal and vertical, since the scanner stage is driven in the $x - y$ (horizontal) plane and the z (vertical) axis is dynamic.

Horizontal distortions include non-linearity and drift. Non-linearity of the piezoelectric ceramics can result in horizontal image distortions. There are several manifestations of piezo non-linearity in the horizontal plane. The most noticeable effect is that straight lines on the sample will appear to be curved in the image. Crosstalk between the x and y ceramics results in horizontal and vertical lines which should be perpendicular being at an incorrect angle. Creep also results in horizontal image distortions, and is most commonly seen in AFM images when features in repeated scans are shifted in position. Drift is the shift from desired position because of non-linearity of the piezoelectric ceramics. This distortion is significant especially when zooming in on small features on the image. In order to prevent these artifacts, repeated scans over the same area are performed, and the image is recorded only when no drift or distortion is found during the scanning.

Vertical distortions include bowing, vertical creep distortions and dynamic range artifacts. Bowing is a common vertical distortion that occurs because the scanner moves out of the plane of the sample when it is scanning. Bowing may occur due to two factors: the scanner geometry and the angle between tip and sample. Creep distortions in the vertical dimension can be seen when a rapid large change in height is encountered. A large step is an example of such a feature. In this case, the top of a steep feature will appear to be sloped, since the z ceramic will continue to distort after the top of the feature is reached.

Another type of creep distortion is the discontinuity in scanning neighboring lines. This is a combined effect of horizontal distortion and the creep of z ceramic. It results in the sudden change in surface height during scanning. Although the surface profile is kept the same, the entire line appears much higher or lower than the previous line. There is also shift in x position when this jump occurs. The third kind of vertical distortion, dynamic range artifacts is because piezoelectric ceramics have a limited physical range. If the change in sample height exceeds this range, due to sample tilt, warp, surface feature size, and objects on the surface, no meaningful data will be collected for the sample beyond the dynamic range. This is called the dynamic range artifacts and will appear as a flat spot on the sample. Common treatment for vertical distortions include increasing driving amplitude for the tip to ensure sharper response and limit creep in vertical movement and careful sample preparation to ensure the sample area is flat and smooth to reduce possible dynamic range artifacts.

Static Electric Charge

The most common artifact in the AFM/NSOM study of film morphology is due to the static electric charge accumulated on the surface of sample films. These static charges may be the result of ambient air, friction between film and other objects prior to sample preparation, or the additives in the film itself. Because of the static electric build-up, the surface will have enough static to attract the tip to the surface. On the viewing monitor, the tip will have sudden vertical movements even if it is not in scanning mode or the tip will tap the surface at regular interval. Because of the static build-up, no meaningful data regarding the surface profile can be collected. It is not possible to neutralize the charge by spraying on the sample any kind of liquid, in order to preserve the surface profile. Since polymer itself is dielectric, grounding is not a feasible way either. Various embedding liquid were used in order to minimize the electric charge on the sample surface. It is found that sugar water has a significant effect in reducing the electric charge of samples.

Typical artifacts that result from static charges are sharp peaks on the surface profile that are not repeatable, the low frequency noise on the internal sensor feedback, linear or triangular surface profiles, and so on. These deformations of the surface profile are not responsive to the changes in feedback control parameters, i.e. the PID values. In extreme cases, it can be observed from the viewing monitor the vertical oscillation of the scanning probe in its initial state. The static charge cannot be avoided completely. To reduce its effect, one can improve the shielding and grounding of the scanning stage. The selection of embedding media is also important so that there is no ion added to the film samples.

Other type of artifacts include vibration and feedback control. The vibration is reduced to minimal by placing the apparatus on a compressed-air vibration isolation table from Integrated Dynamics Engineering. The table is kept afloat at $100psi$ input air pressure. Feedback control requires many trials to determine the optimum combination of control parameters.

In general, to ensure the quality and reproducibility of the images, repeated scans are done for the same sample at different areas. In addition, different probes are used for the scanning of the same sample. The apparatus is regularly calibrated using a standard sample of semiconductor grid, to test the performance of $x-y$ piezo and z piezo.

3.3 Surface Morphology Observations

3.3.1 AFM images

The samples studied here are of different resin compositions, produced under similar processing conditions. The AFM scan size is 35μm × 35μm. Scan rates varied from 10% to 50% of the range per second. Although the AFM apparatus used in the study has the ability to scan at 1μm × 1μm range, it is the selected large scan size which is of great interest. It contains a large number of data points for the surface and offsets the statistical bias and thus, produces a more accurate statistical representation of surface characteristics. This was demonstrated by repeatedly scanning the same region of interest at different ranges and scan rates. It was seen that 35μm × 35μm would produce the optimum effect. For smaller scan ranges, the images obtained contained random noise generated by the tip, and repeated scans were unlikely to reproduce identical surface profiles because of the hysteresis of the x and y piezos that controls the raster scan. In addition, the smaller scan range results in surface profiles that depend largely upon the location on the surface. Therefore, surface roughness values obtained from these images will be more prone to statistical bias. In general, a smaller scan range adds more noise into the surface roughness, and renders the final results less dependable. All aspects considered, the scan range of 35μm × 35μm was selected as the desirable scan range for all of the samples.

Morphology of Sample Films

Figure 3-5 shows the AFM images of the surface topography of various samples. In all of the scanned images, the draw direction during film blowing process (i.e. machine direction) is vertical upwards with respect to the page. The stacked three-dimensional domain structure is apparent on the images for all samples. It is believed that such

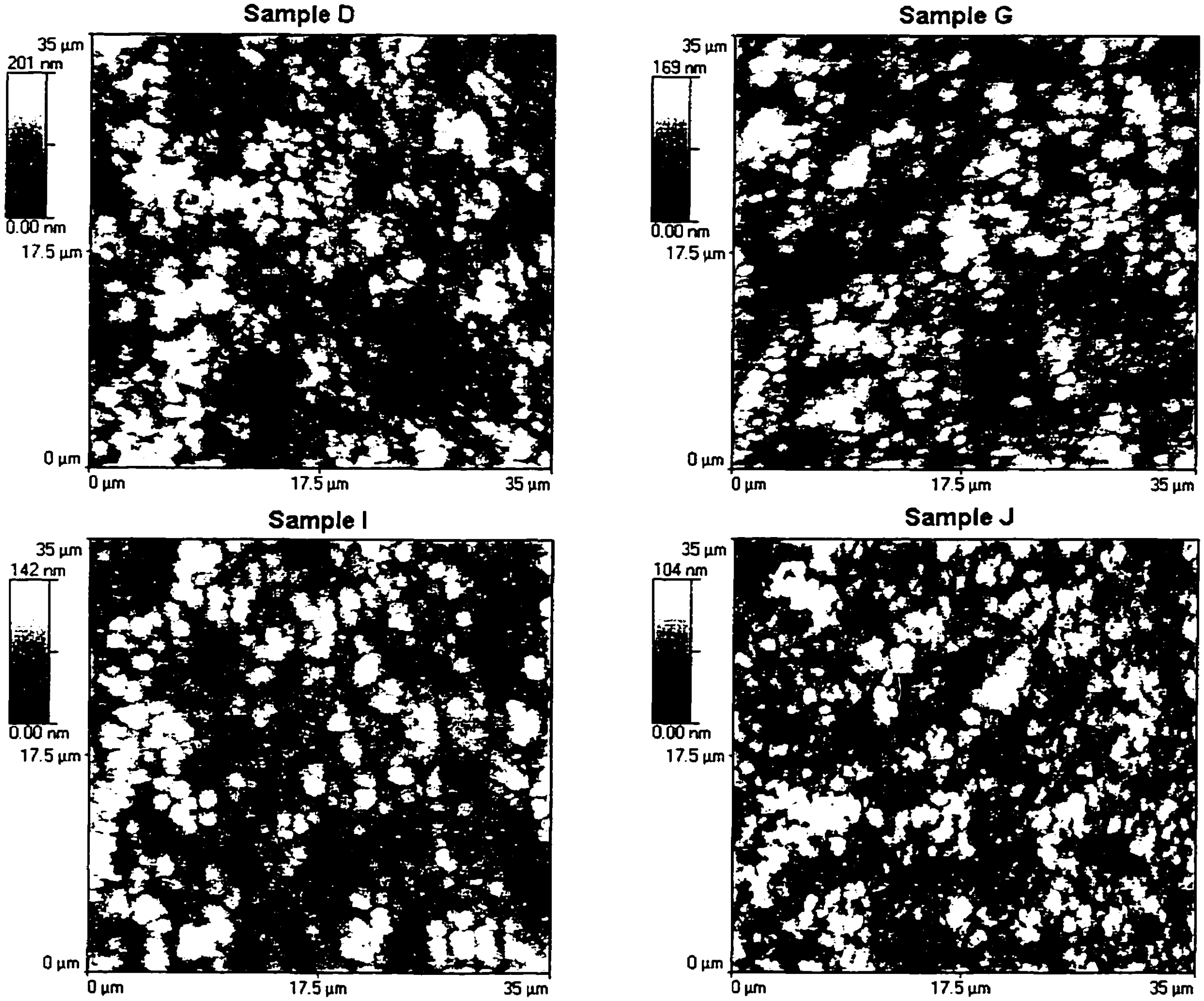

Figure 3-5: Surface AFM images of Sample D, G, I and J.

roughness domains observed on the samples are spherulites, mainly the result of crystallization on and beneath the surface during the film blowing process. In the following discussion of surface morphology, the term "domain" is used to refer to the spherical entities observed on the film surfaces.

The major difference among different sample surfaces is the size of the domain structure. For Sample D, the average and dominant domain size is of 200 to 300 nm in diameter. Whereas for Sample I, the dominant domain size is 1μm in diameter. It is generally agreed that surface morphology is also affected by the biaxial extensional flow and shear deformation that occur in the blowing process. The effect of the mechanical history in the blowing process is reflected in the shape of the domains as well as their arrangements. Since all sample films are produced at similar processing conditions, it is considered that the effect of the mechanical history during the process on the differences in surface morphology between sample films are less significant than the effect of crystallization behavior, which strongly depends on the thermal history, the resin compositions and the polymer structure, i.e. molecular weight distribution, long chain branching, comonomer type and content. A quantitative assessment of the effect of crystallization during the film blowing process on the surface morphology of films must await detailed crystallization kinetics study of the different resins.

The surface profile of sample film I is shown in Figure 3-6. The left side is the top-view of surface morphology and the right side is the three-dimensional view of the same surface. There is no significant variance in the shape of the domains. This observation suggests that the influence of the mechanical history, such as the biaxial extensional flow and the shear deformation in the melt flow during the blowing process, may not have a significant influence on the morphology of the films studied. Of all the sample films studied, none exhibited strong orientation preference with respect to machine direction, neither in the shape of the domain nor in the aggregation of clusters. Setting aside

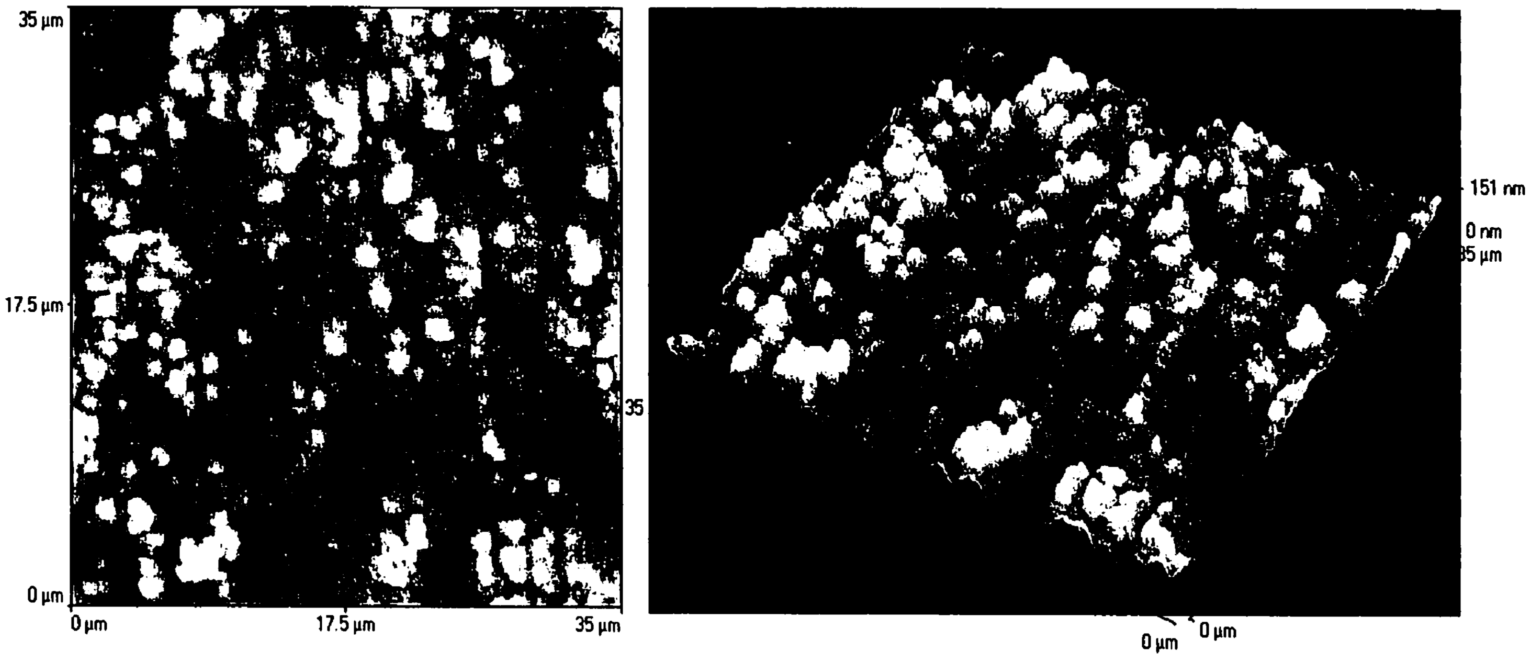

Outside Surface of Sample I

Figure 3-6: AFM image of Sample I outside surface by non-contact AFM; scan size: $35\mu m \times 35\mu m$.

the effect of impingement during the development of domain structure, all samples show similar randomly distributed structures. Comparing the images to the other sample films presented in Figure 3-5, the domains of Sample I appears to be more uniform in size. On average, the domains in Sample I appear to be larger than the domains observed for other film surfaces. Since the processing conditions were identical in producing these films, the difference in surface morphology is attributed to the different resin compositions.

The surface topography of all samples are shown in Appendix B. The outside and inside surface topography of all samples exhibit spherulitic structures to some degree. There is no regular clustering, nor preferred orientation in either distribution or the shape of individual spherulites on all the samples. Since all sample films are produced under similar processing conditions, it suggests that the biaxial flow in the process does not have a significant influence on the formation and growth of spherulites on the film surface.

Morphology of Inside and Outside Surfaces

Figure 3-7 shows images of the inside and outside of sample D of Set I. The difference in the physical conditions on the outside and the inside surfaces of polymer films during the film blowing process is a natural result of the film blowing process. The outside surface is cooled by air flow from an air ring placed outside the die, whereas in most instances, the inside surface is cooled with stagnant air inside the film bubble. Due to this difference, the temperature on the outside surface is lower than that of the inside surface. From Figure 3-7, it can be seen that both sides exhibit similar domain structures. The outside surface, however, noticeably has a more diversified domain size distribution and smaller domains on average than the inside surface. This observation is in contradiction to the conclusion in Smith et al [25], who found no difference between the surface morphology of the outside and inside surfaces of polymer blown films. This difference in surface morphology of the

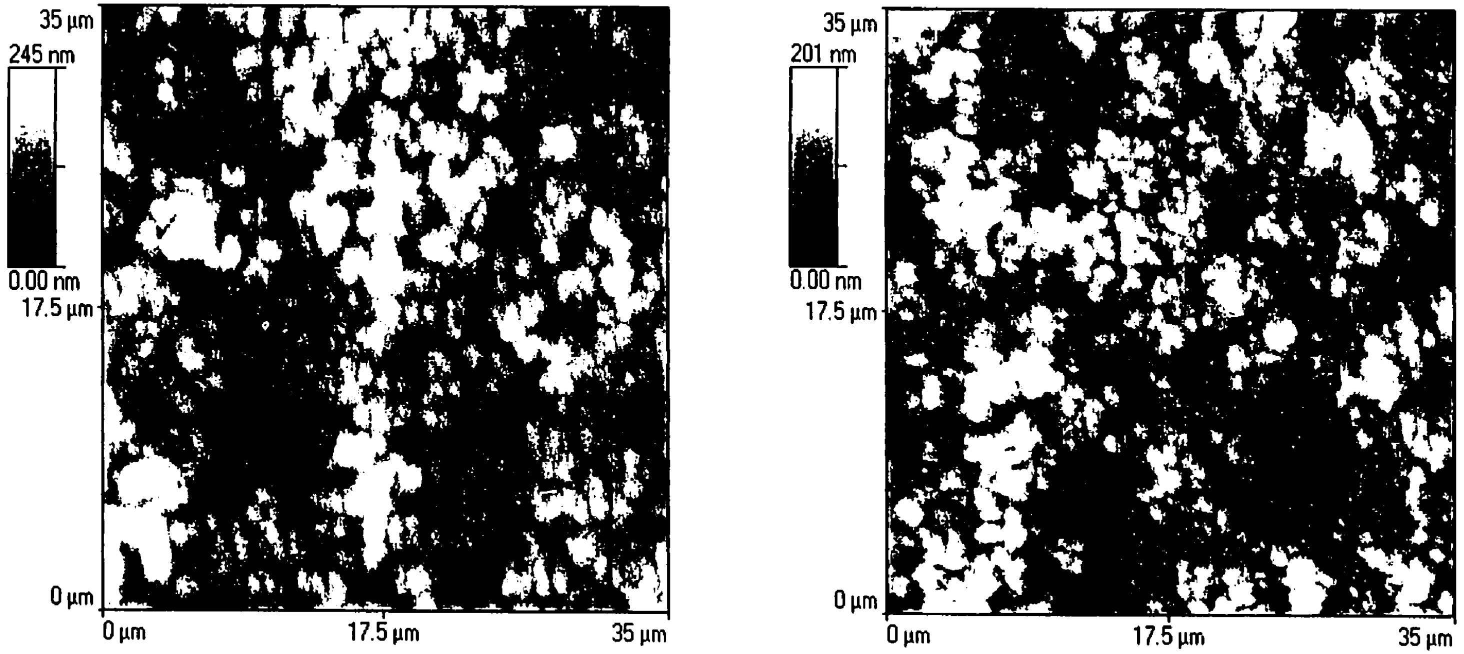

Inside Surface

Outside Surface

Figure 3-7: Inside and Outside Surfaces of Sample D Set I

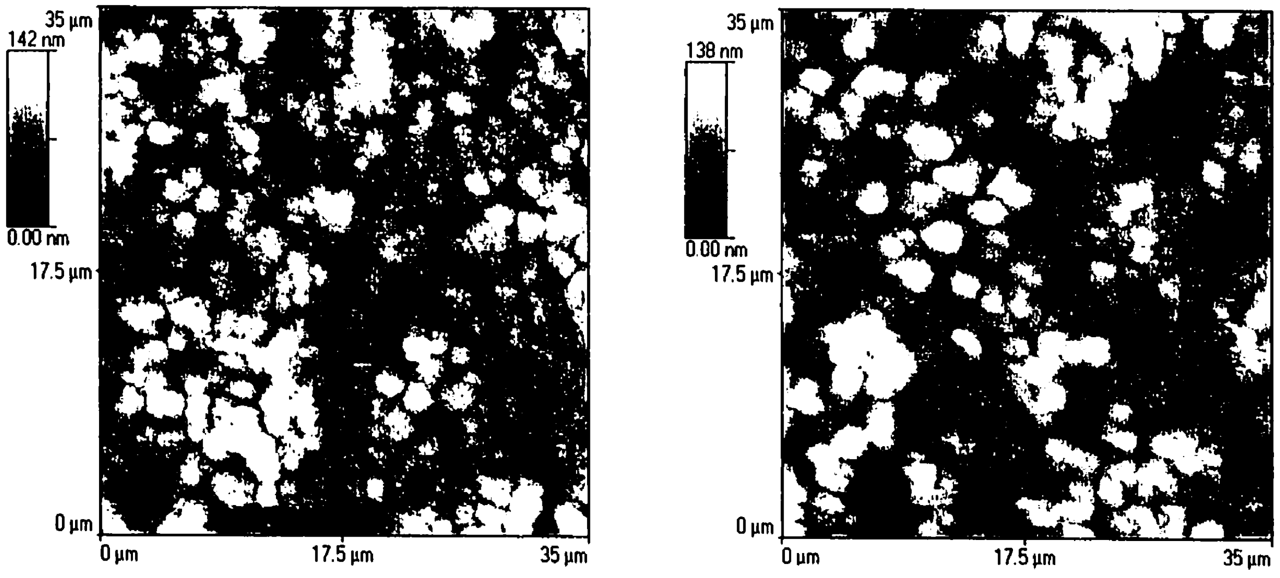

Outside Surface **Inside Surface**

Figure 3-8: Inside and Outside Surfaces of Sample D_{82} Set II

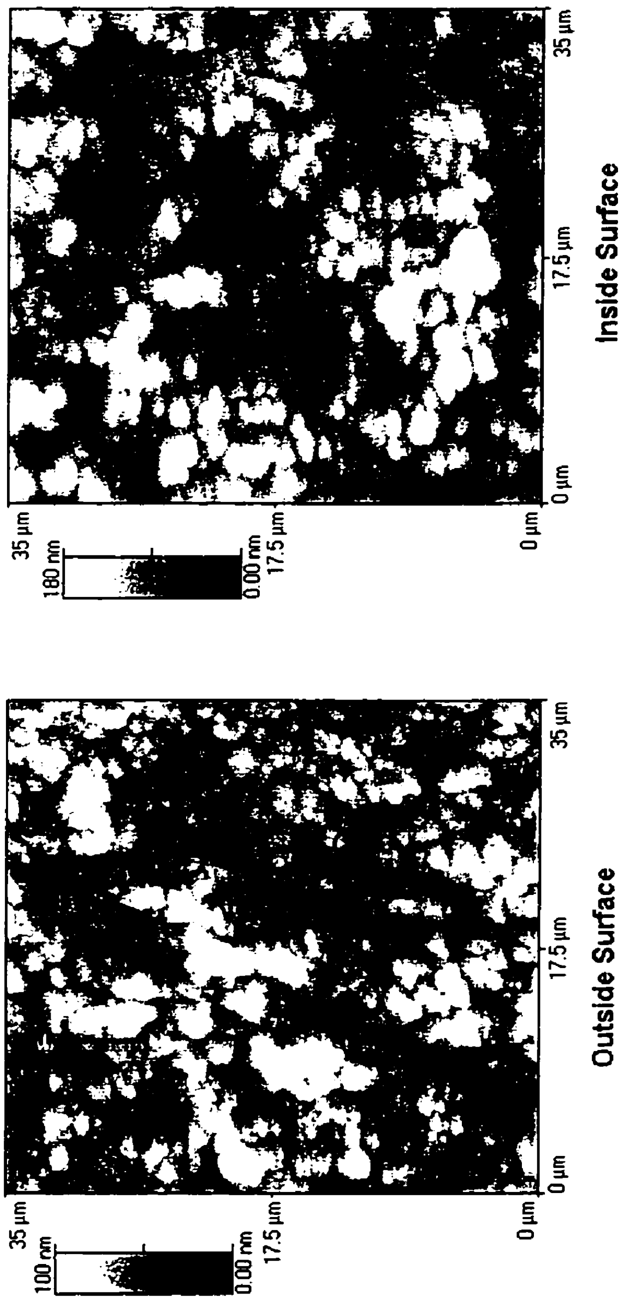

Figure 3-9: Inside and Outside Surfaces of Sample D_{84} Set II

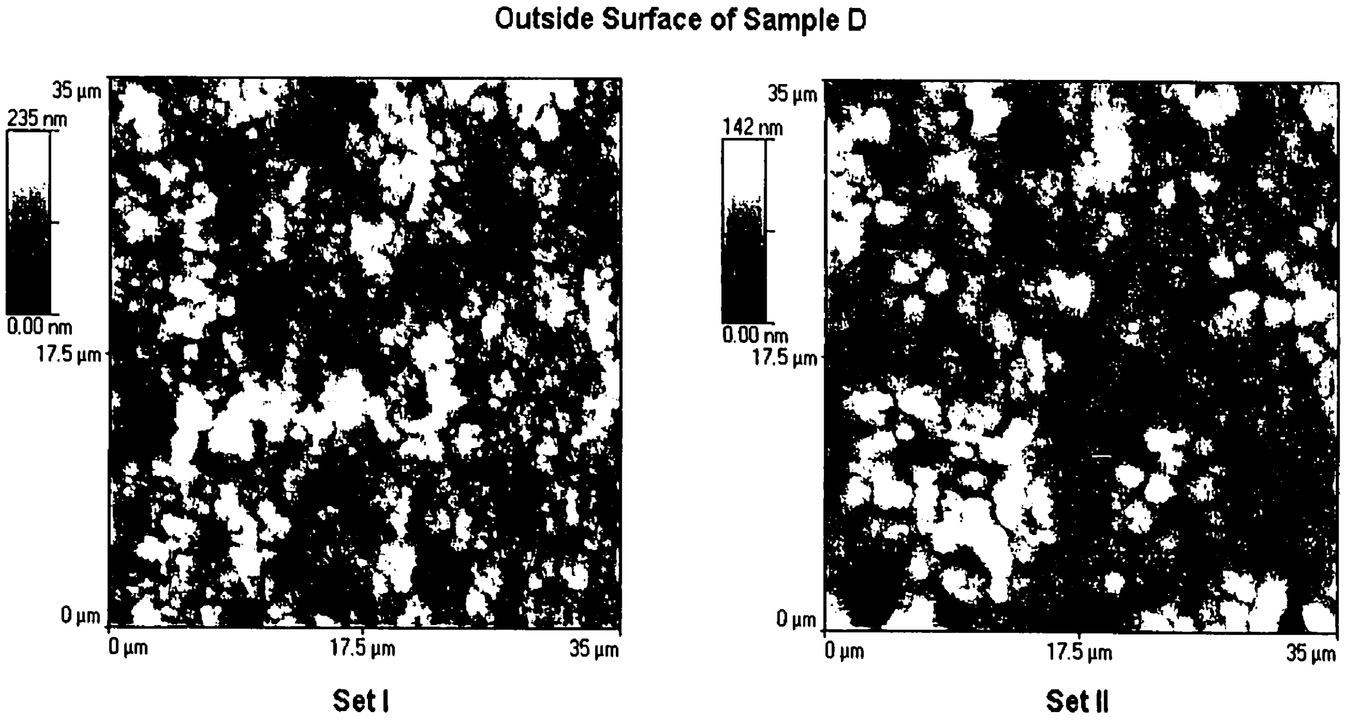

Figure 3-10: Outside Surfaces of Sample D Set I and Sample D_{82} Set II

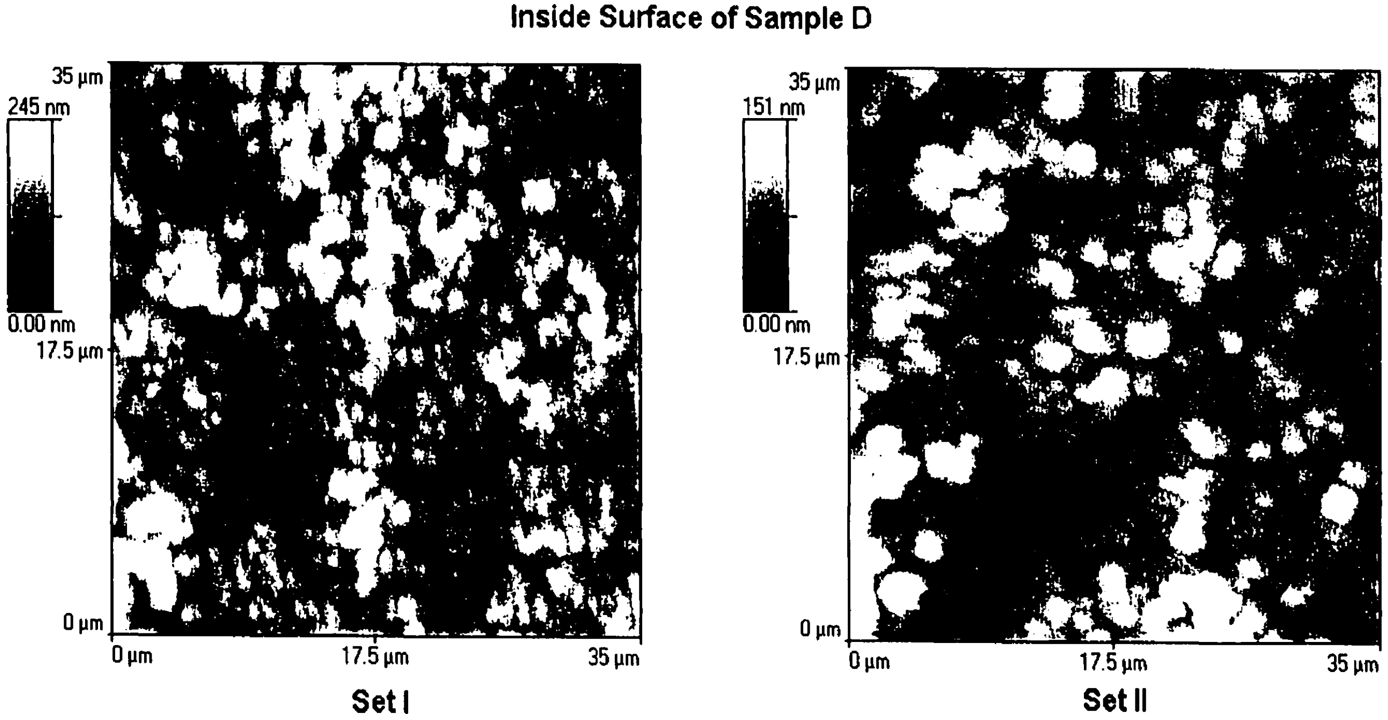

Figure 3-11: Inside Surfaces of Sample D Set I and Sample D_{82} Set II

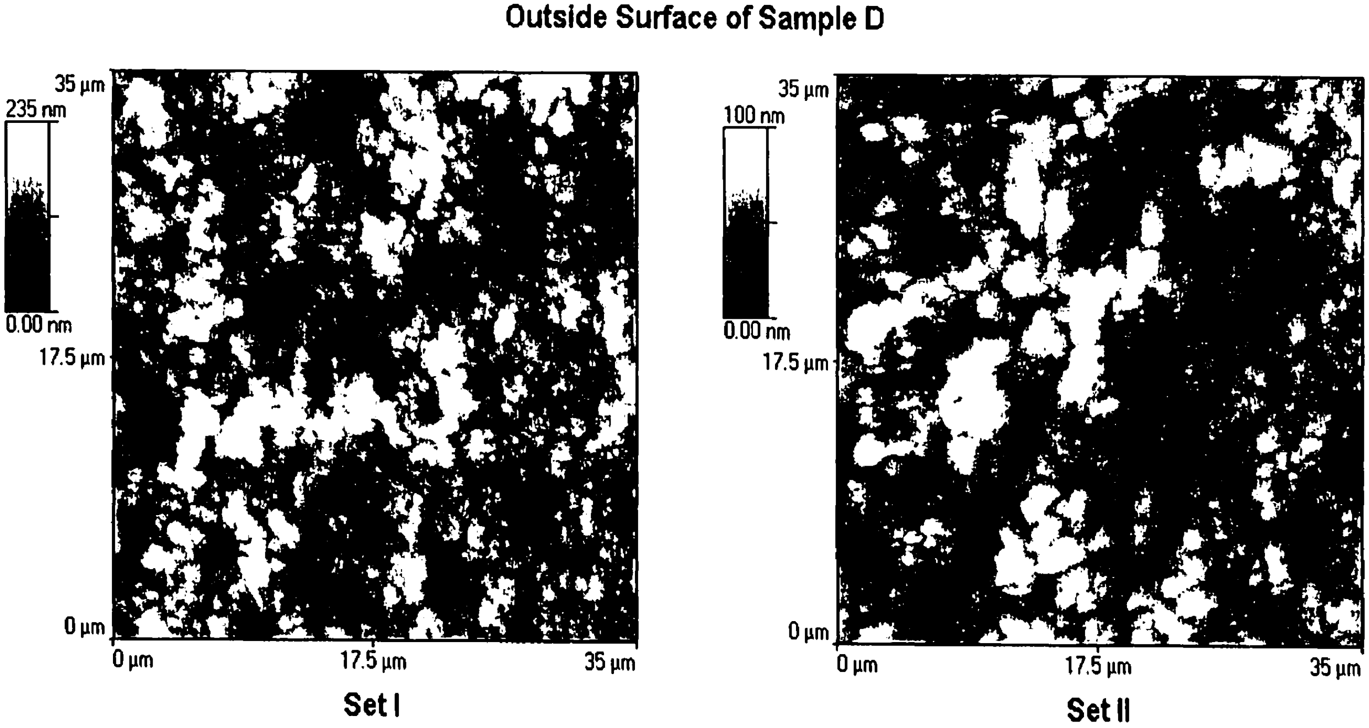

Figure 3-12: Outside Surfaces of Sample D Set I and Sample D_{84} Set II

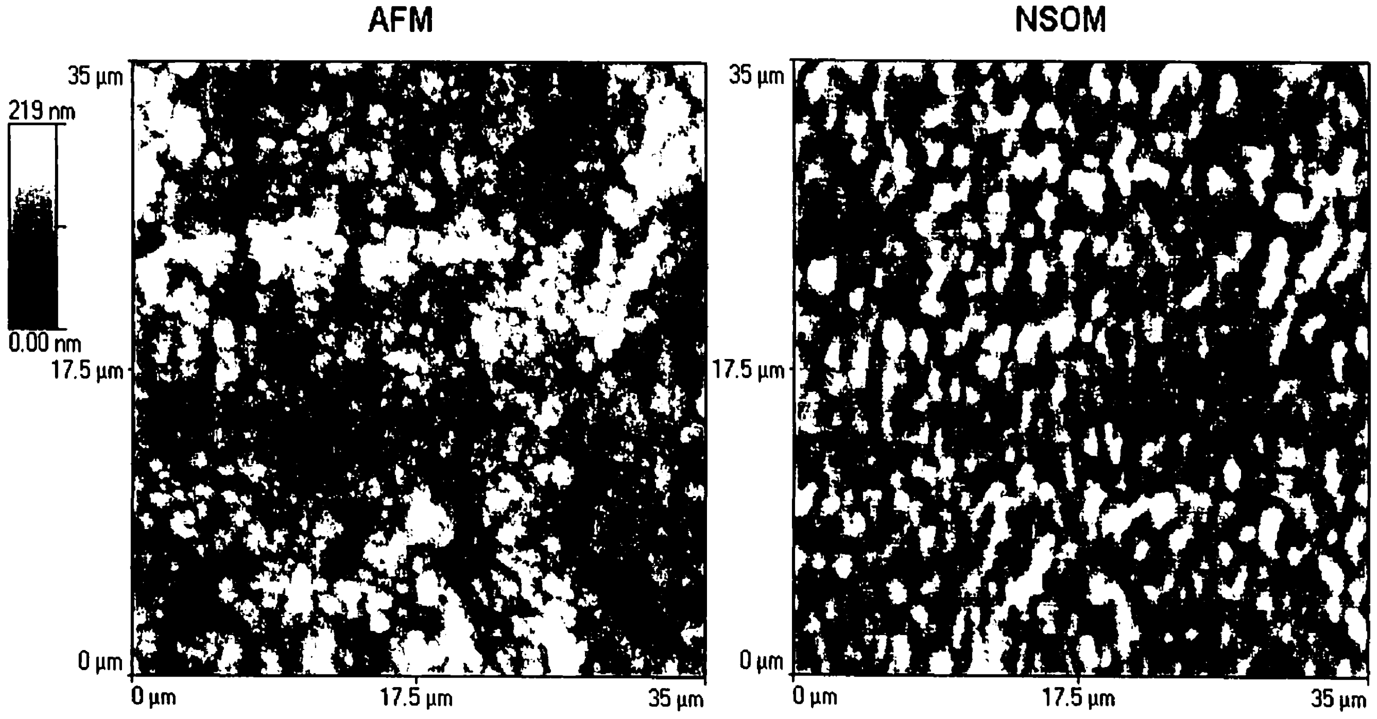

Figure 3-13: AFM and NSOM images of the outside surface of Sample D Set I

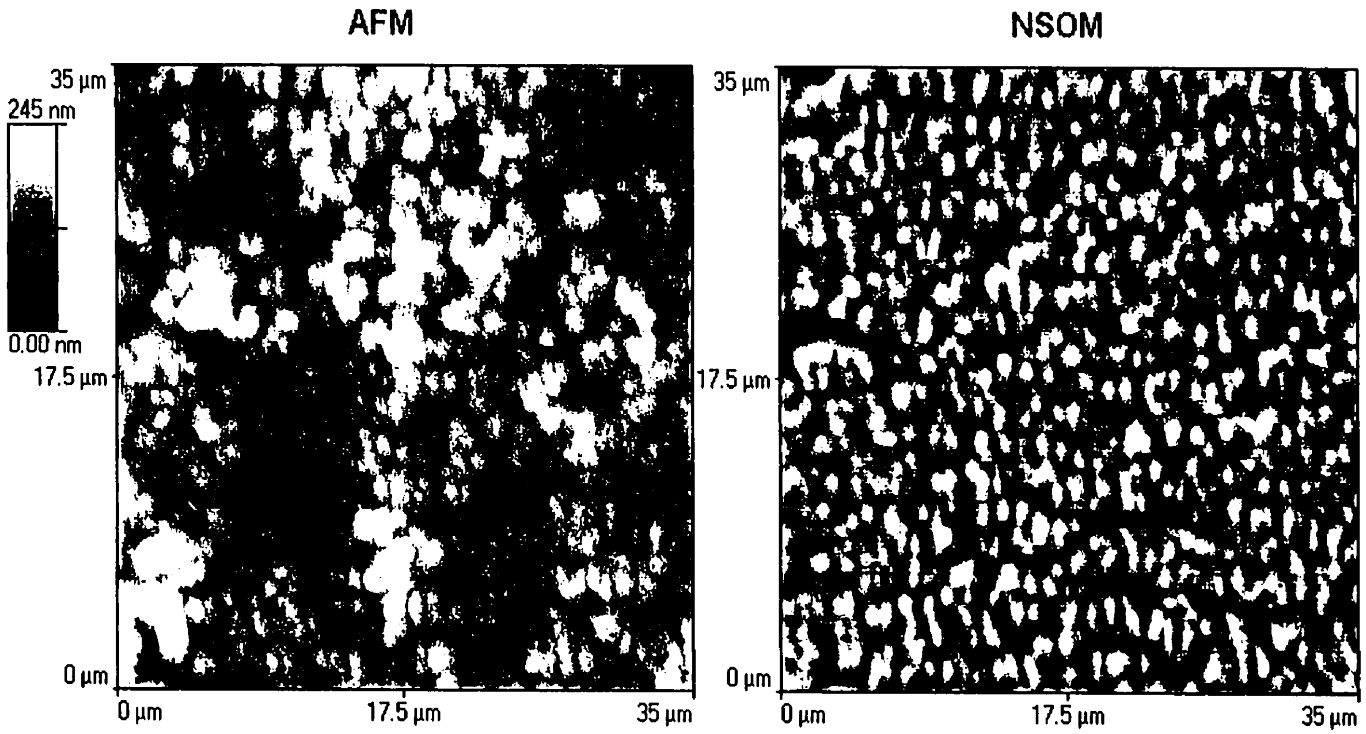

Figure 3-14: AFM and NSOM images of the inside surface of Sample D Set I

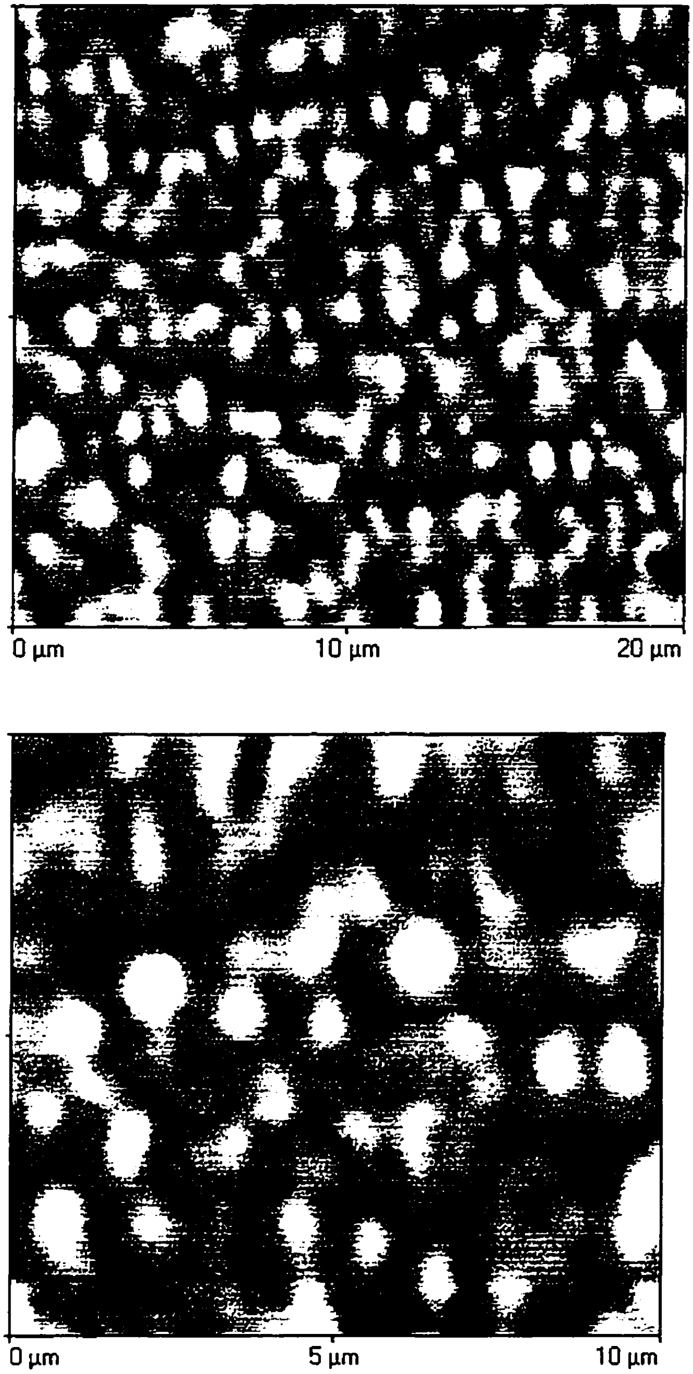

Figure 3-15: NSOM images of outside surface of Sample D $20\mu m \times 20\mu m$ and $10\mu m \times 10\mu m$

Figure 3-13 and Figure 3-14 show the AFM and NSOM images of the outside and inside surfaces of Sample D. It can be observed that there is good correlation between the images of the top layer of spherulites by AFM and NSOM. The relative z position of the spherulites is not clear in the NSOM image because during the scan the tip-to-sample distance is maintained constant. Hence, the optical image does not reveal the relative height of the spherulites. The boundaries of the spherulites, however, are more clearly defined in the NSOM image.

Figure 3-15 shows the NSOM image of the outside surface of Sample D at the ranges of $20\mu m \times 20\mu m$ and $10\mu m \times 10\mu m$.

In Figure 3-15, the top layer of the surface shows separate domains that agree with the findings from the AFM images of the same surface. Comparing with AFM images, the boundaries of the spherulites are more clearly defined. The spherulites appear to have similar shape and size, indicating a more or less uniform nucleation and growth of spherulites at the top layer of the film surface where there is no impingement. There is no segregation or clustering of spherulites on the surface.

3.3.3 TEM images

Other microscopy methods were employed to characterize film morphology. Among them, Transmission Electron Microscopy (TEM) is a relatively well established method [26].

By passing a beam electron through a thin slice of sample, the electrons are deflected by the molecules inside the sample. The resulting pattern will then accurately describe the internal structure of the sample. TEM has the highest resolution among all of the microscopy methods used in this study. Its application, however, is limited due to the difficulty in sample preparation. For successful TEM imaging, the sample cannot be more than a few tens of angstroms thick. The method used to prepare a polyethylene blown film for TEM involves producing an accurate replica of the surface. This is done

Figure 3-16: TEM image of outside surface of Sample G

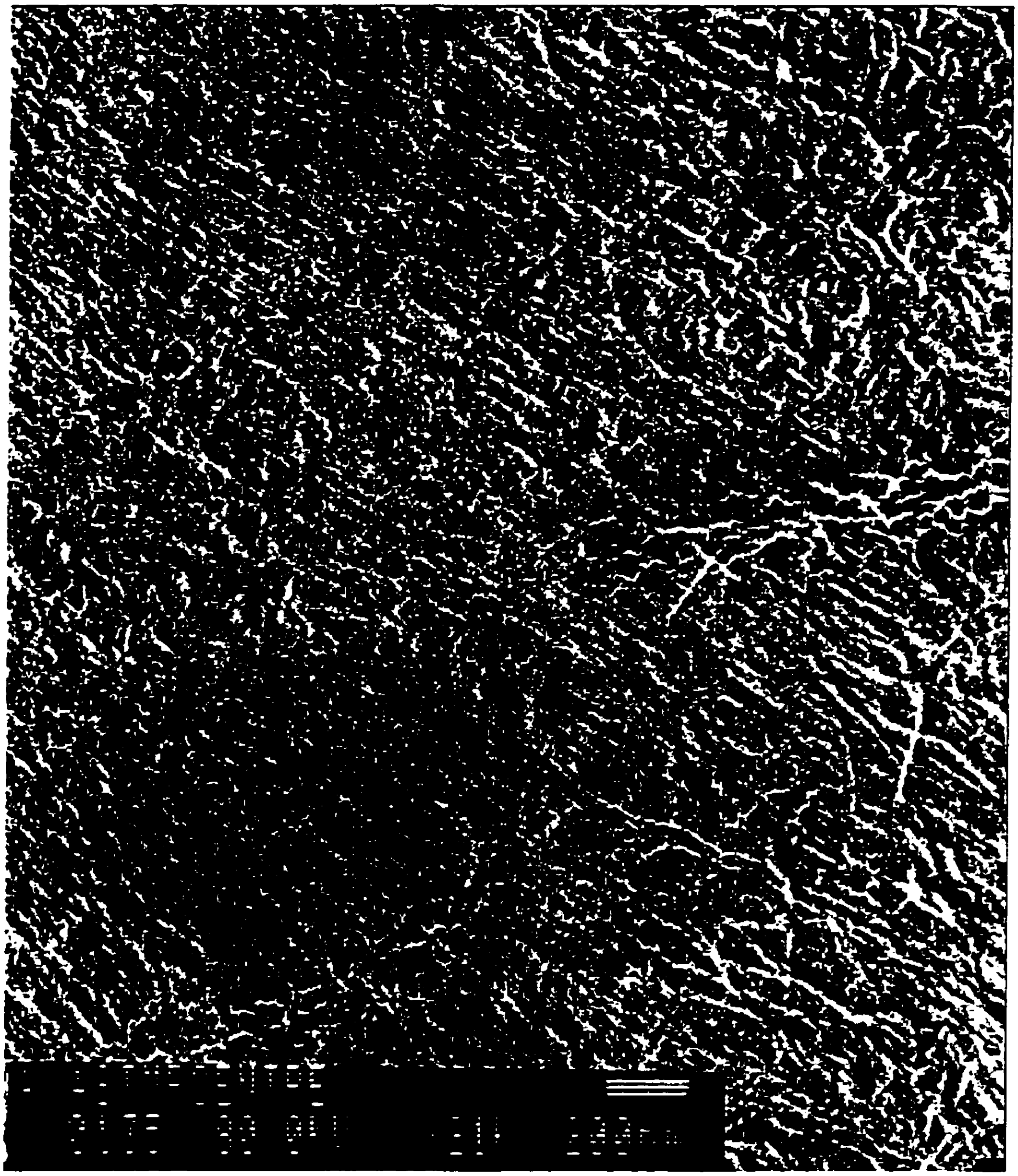

Figure 3-17: TEM image of outside surface of Sample G

by depositing a layer of platinum atoms on the surface of the film in a vacuum chamber. First, the platinum is heated to its vaporizing temperature. The floating atoms in the vapor are then freely deposited on the film sample which is positioned on the bottom of the oven. The thickness of the replica is determined by measuring the deposit thickness at a reference point next to the film sample. The replica must be separated from the film without any damage to its profile before it can be successfully imaged using TEM. The film sample with the replica deposited on its surface is sandwiched between two glass slides and immersed in boiling xylene. After the polyethylene film is completely dissolved, the replica is preserved on one of the glass slides and is ready for TEM imaging.

The TEM image of the outside surface of sample G is shown in Figure 3-16 and Figure 3-17. The humps clearly visible on the surface are identified as spherulites. The lamellar structure of these spherulites is clearly visible on the finer scale TEM image. The dimensions of the spherulites observed here roughly matches the dimension of those from the AFM images shown above. This confirms that the roughness of the film surface is due to the presence of spherulites.

3.4 Cross-section Morphology

The bulk morphology is determined by an examination of the cross-section of the film sample.

3.4.1 Sample Preparation: Ultramicrotomy

Ultramicrotomy is very commonly used in the preparation of biological specimens and polymer materials for microscopy. The materials must be carefully fixed, stained and embedded prior to sectioning. The purpose is to provide sections with visible fine structure that represent the original material. Polymer materials are generally easy to prepare prior to sectioning. Due to the softness of the material, however, some polymer materials are very difficult to section at room temperature. Therefore, they must be hardened either chemically, or by cooling below room temperature during microtomy. This process is called cryosectioning.

The ultramicrotome used here is the Leica Reichert Ultracut S with Reichert FCS chamber system attachment. The Ultracut system includes:
Ultracut S Microtome
Stereomicroscope
Drive system

The FCS chamber system is an attachment specifically designed for ultrathin frozen sectioning. It includes:
Cryochamber
Control Unit
Dewar vessel for liquid nitrogen on mobile trolley
Liquid Nitrogen pump

The material is polyethylene blown thin films. Since the sample is often too soft for sectioning at room temperature, it is cooled below its glass transition temperature for better results. The sectioning operation is conducted at $-160^{o}C$. Typical sample cutting directions (PL direction, VL direction and 45°) are shown in Figure 3-18.

A section ($4mm \times 4mm$) of the sample film is inserted into a drop of embedding media liquid on a sample holder. The embedding media used here is the Frozen Tissue Embedding Media from FisherDiagnostic. It contains water, polyvinyl alcohol, 2-phenoxyethanol, polyoxpropylene-polyoxyethylene block copolymer. The sample is then immersed in liquid nitrogen until the film sample and the embedding media are frozen. The frozen sample is then placed into the frozen chamber of the microtome that has been cooled to $-160^{o}C$ and positioned according to the required section direction. A 45° glass knife is used in the sectioning.

The sample in the PL direction is trimmed using the side edge of the glass knife. After trimming, it is turned into the VL direction and moved to the center of the knife edge. The sample is then sectioned in either VL direction or 45° direction for different thicknesses (1μm ~ 5μm) at various speeds ($1mm/s$, $5mm/s$, $8mm/s$). The results are viewed through the stereomicroscope attached to the microtome. Finally, the slice is placed on a thin glass slide for further analysis.

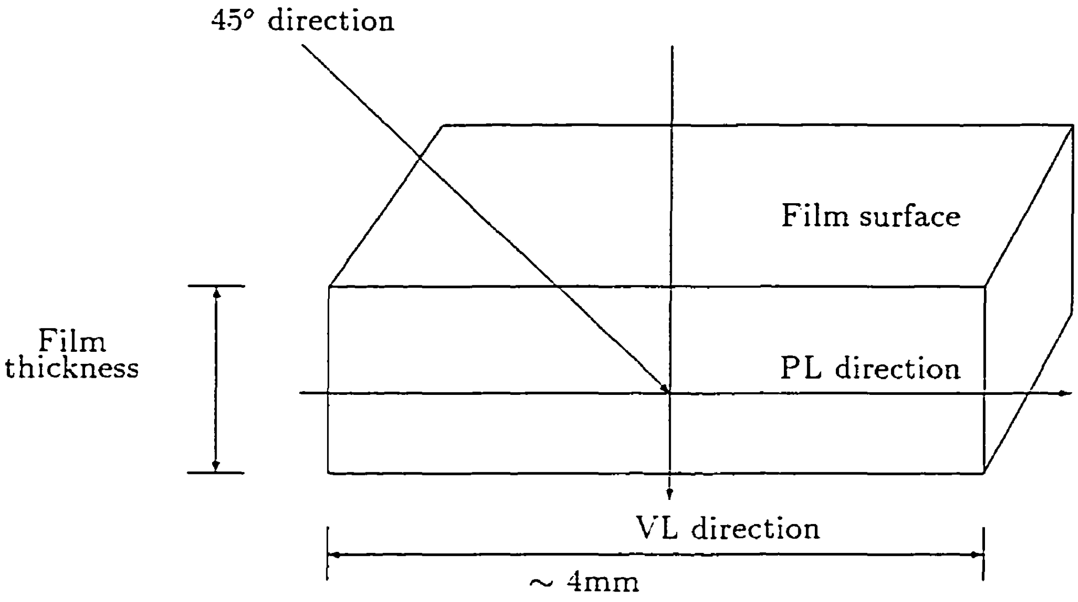

Figure 3-18: Sample cutting direction

3.4.2 Cross-section Morphology of Sample Films

Figure 3-19 shows the cross-section of film G. The cutting direction is vertical. The scan range here is 10μm × 10μm. Slices with varying thickness were also examined by AFM and it was found that the slices with different thicknesses exhibit the same morphology, which means that the layer structure in the sample slices is not influenced

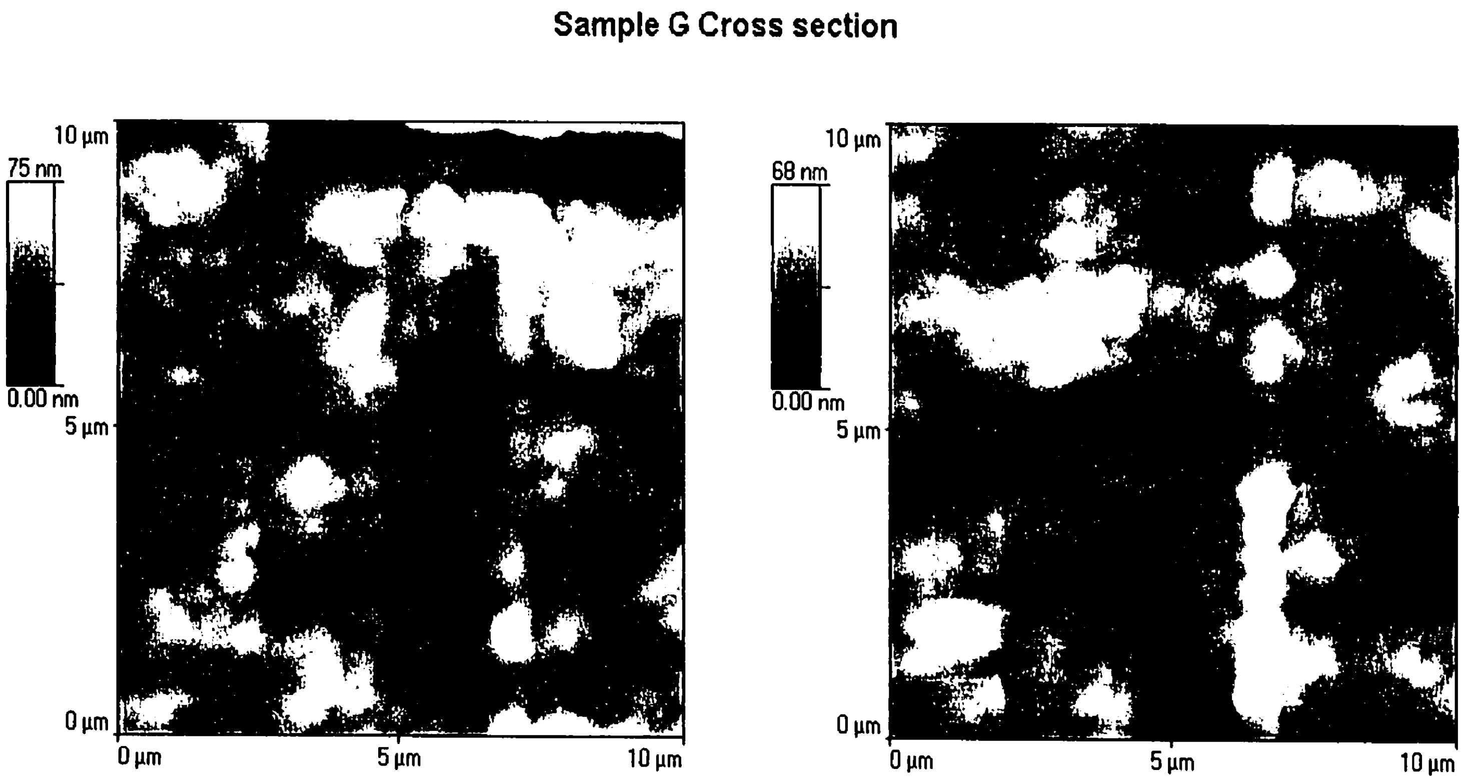

Sample G Cross section

Figure 3-19: AFM images of the cross-section of Sample G.

by the preparation conditions. The domain structures are densely packed in the bulk of the film sample. The size of these domains appears to be uniform. When compared to the domains of the surface, the size of the domain in the bulk is generally much smaller. This is because the nucleation occurs first on the surface because it is cooled before the bulk. The nucleation in the bulk immediately follows. Due to the large amount of nucleation points, however, the spherulites in the bulk will be fully impinged, while the spherulites on the surface are allowed a longer time to develop with a free boundary. As a result, the spherulites on the surface are larger in comparison with those in the bulk.

3.5 Characterization of Morphology

The AFM and NSOM images presented above give us qualitative knowledge of the film morphology. These observations, however, would not be useful without a quantitative analysis. In this project, a number of methods have been employed in the characterization of the morphology of films.

3.5.1 Surface Roughness

Surface roughness is best described by the statistical distribution of its deviation from a certain mean level. The average height of a rough surface $\xi(x,y)$, i.e. its mean level, is defined as:

$$\sigma_{ave} = \frac{1}{4XY}\int_{-X}^{X}\int_{-Y}^{Y}\xi(x,y)dxdy \tag{3.1}$$

where $2X$ and $2Y$ are the dimensions of the boundaries of the rectangular region under consideration, and the area A is given by $A = 4XY$. Let $\sigma_{ave} = 0$, then the standard deviation is given by:

$$\sigma = \sqrt{\frac{1}{N}\Sigma(\xi(x_i,y_j))^2} \tag{3.2}$$

As defined here, the standard deviation σ is the root-mean-square value of ξ, which describes the surface roughness. A large σ corresponds to large roughness; on the other hand, when $\sigma \to 0$, the surface ξ will cease to be a random variable and become a smooth surface. In the present work, the value of the surface roughness from experimental images is obtained by:

$$\sigma = \sqrt{\frac{1}{N}\sum_{k=1}^{N} z_k^2} \tag{3.3}$$

where $z_k, k = 1, 2, \ldots$ are the surface heights of discrete points on the surface. With the surface profile, the surface height average and the standard deviation are easily computed.

Area roughness measurements can characterize how "rough" a surface is and make quantitative comparison among sample surfaces. It cannot, however, represent any orientational preference or clustering of the roughness on the surface. Therefore, in addition to area roughness, line roughness is also measured and compared. On the AFM image of a surface profile, horizontal and vertical lines are randomly picked. Their average height and standard deviation are computed from the line profile. The results show that the surface roughness distribution has no orientational preference of spherulites, i.e. the average height and standard deviation for lines in x and y directions are mostly identical, suggesting the surface roughness is one-dimensional. For different horizontal or vertical lines, the parameters are also identical. This shows that there is no clustering on the surface and all the roughness is uniformly randomly distributed.

The standard deviation of surface roughness, i.e. σ, of all film samples are presented in Table 3.1.

Table 3.1: Surface Roughness of Sample Films (nm)

	A	B	C	D	E	F	G	H	I	J	K	L	M
O	29.8	20.4	32.2	36.9	34.6	109.1	41.7	24.3	32.4	27.8	58.5	27.0	26.9
I	27.9	19.4	38.9	39.3	34.9	85.0	45.2	28.6	33.7	28.1	42.9	23.6	28.7

3.5.2 Lateral Correlation Function and Correlation Length

For a simple one-dimensional case, the surface is given by a random stationary process $\eta(x)$ and is constant in the y direction. Let $\eta(x)$ be a random variable assuming the values z with a probability density $w(z)$; let the mean value be zero:

$$<\eta>=0 \tag{3.4}$$

For a purely random function $\eta(x)$, any two values $\eta(x_1)$ and $\eta(x_2)$ are independent, i.e. the function does not contain any non-random periodic spatial patterns. The separation parameter is defined as:

$$\tau = x_1 - x_2 \tag{3.5}$$

When τ is small, i.e. when x_1 and x_2 are close to one another, then $\eta(x_1)$ and $\eta(x_2)$ may be correlated. The apparent extreme case is that the two points will be identical when $\tau = 0$. Thus, the probability density function $w(z)$ is not able to amply describe the rough surface η. In addition, we must know the correlation function of η, defined as:

$$B(\tau) = \lim_{L\to\infty} \frac{1}{2L} \int_{-L}^{L} \eta(x)\eta(x+\tau)dx \tag{3.6}$$

or the normalized correlation function, also known as the autocorrelation function, defined from the correlation function $B(\tau)$ as:

$$C(\tau) = \frac{<\eta_1\eta_2> - <\eta_1><\eta_2>}{<\eta_1^2> - <\eta_1>^2} = \frac{<\eta_1\eta_2>}{<\eta_1^2>} \tag{3.7}$$

It follows that for a purely random surface:

$$\lim_{\tau\to 0} C(\tau) = 1 \tag{3.8}$$

(full correlation, linear dependence) and

$$\lim_{\tau\to\infty} C(\tau) = 0 \tag{3.9}$$

(independence). For a pure random surface, $C(\tau)$ will decrease monotonically from its maximum $C(0) = 1$ to $C(\infty) = 0$. Should there be a weakly repeating pattern, however, embedded in the random surface, a local maximum would occur at $C(T)$ and T is defined as the correlation length.

The autocorrelation function of surface height is also an important factor in statistically characterizing the surface roughness, which is the indicator of whether the roughnesses on the surface form clusters, are far from each other, or form other regular or irregular distribution patterns. Many researchers assume a Gaussian correlation function, which represents a normally distributed random surface, and others assume the correlation function to be simply exponential [27]. An improved approximation [28] is applied here. The lateral correlation function $C(\tau)$ given by

$$C(\tau) = exp(-|\frac{\tau}{T}|^{\alpha}) \tag{3.10}$$

where τ is the spatial distance. T is the lateral correlation length and α is a constant. To determine the values of T and α, different values of $C(\tau)$ are calculated from discreet data points C_j from the surface height profile with

$$C_j = \frac{1}{\sigma^2(N-j)} \sum_{k=1}^{N-j} z_k z_{k+j}, \quad j = 0, 1, \ldots, N \tag{3.11}$$

and $C(0) = 1$. N, the number of data points, is given by the size and resolution of the surface height image. After determining the values of C_j from the surface topography extracted from the experimental AFM images, the correlation length T is determined by the value of τ at the first peak on $C(\tau)$. The value of $C(T)$ indicates the strength of this correlation. Small values $C(T)$ represents a weak correlation. On the other extreme $C(T) = 1$ represents a purely periodic surface. Once T is determined from $C(\tau)$, α is then fitted from C_j using the least-square method.

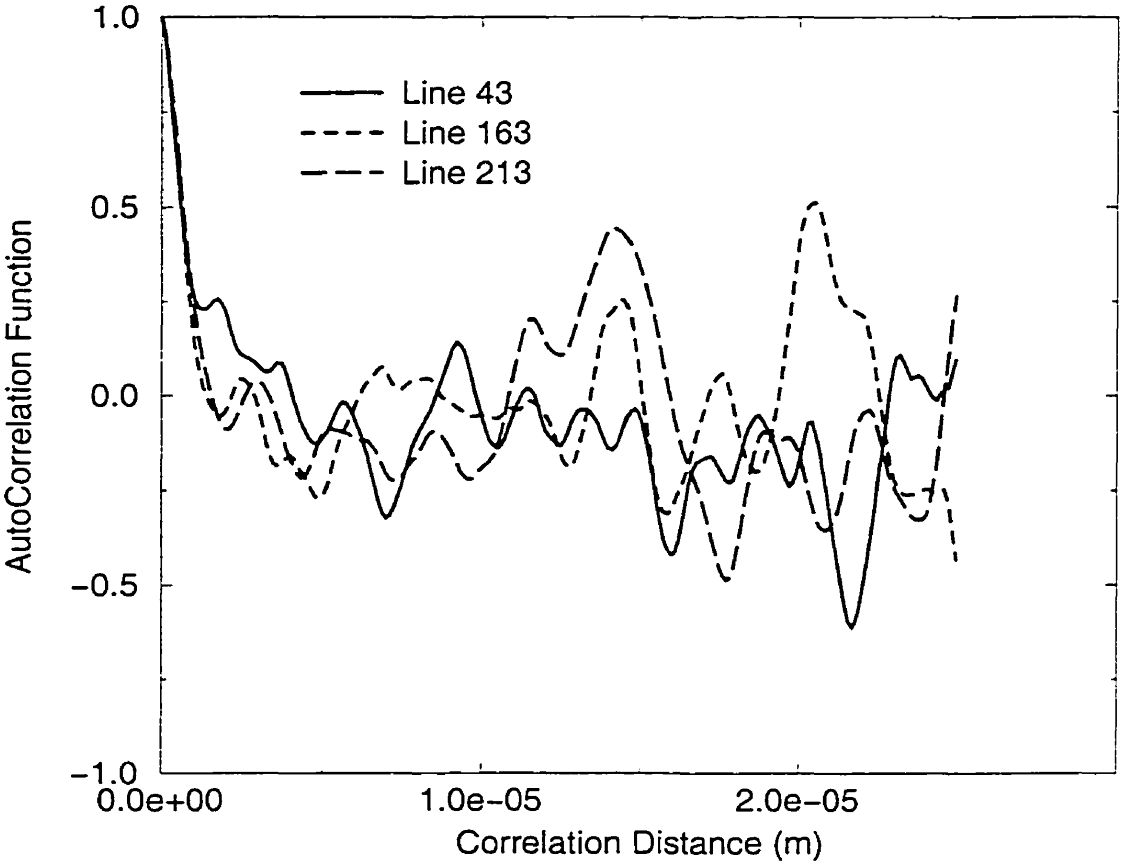

Figure 3-20: Lateral correlation functions for Lines 43, 163 and 213 of Sample I.

Figure 3-20 shows a plot of the correlation functions for the lines 43, 163 and 213 of sample I outside surface. The correlation lengths $T = 3.929\mu\text{m}, 3.504\mu\text{m}, 3.908\mu\text{m}$ are

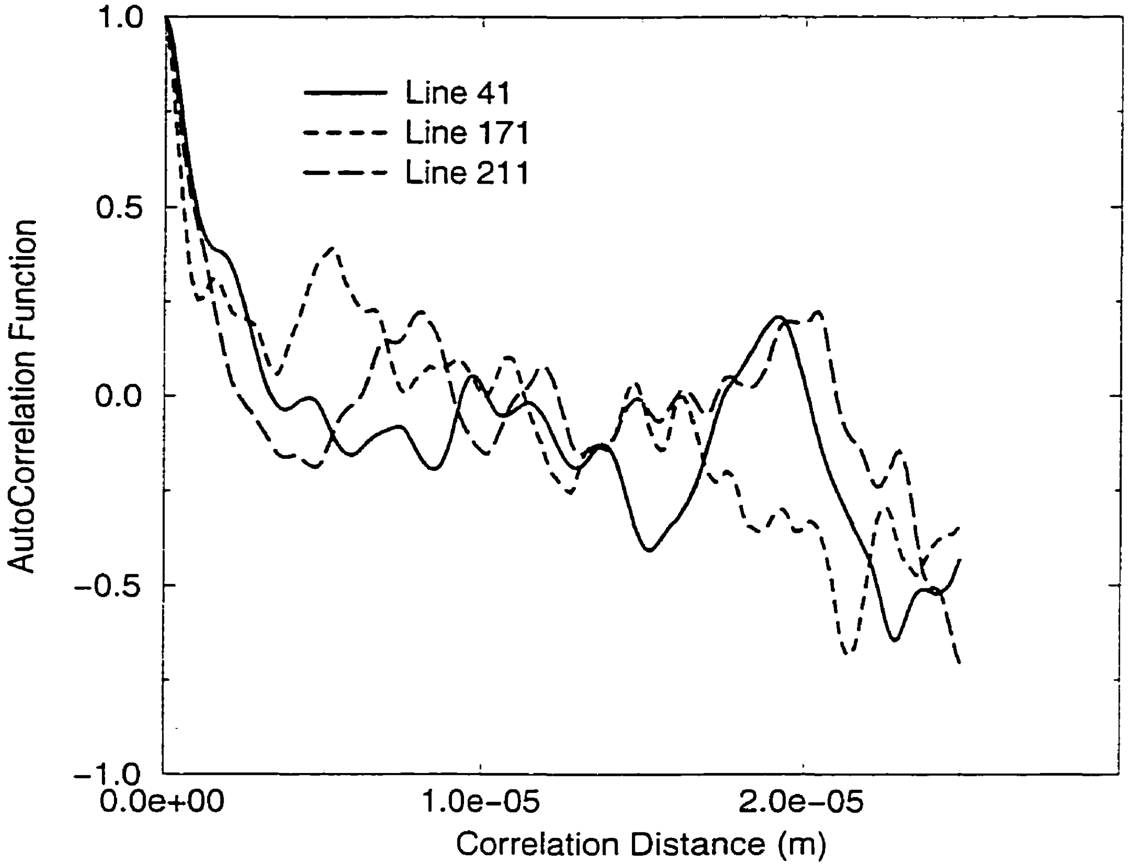

Figure 3-21: Lateral correlation functions for Lines 41, 171 and 211 of Sample D.

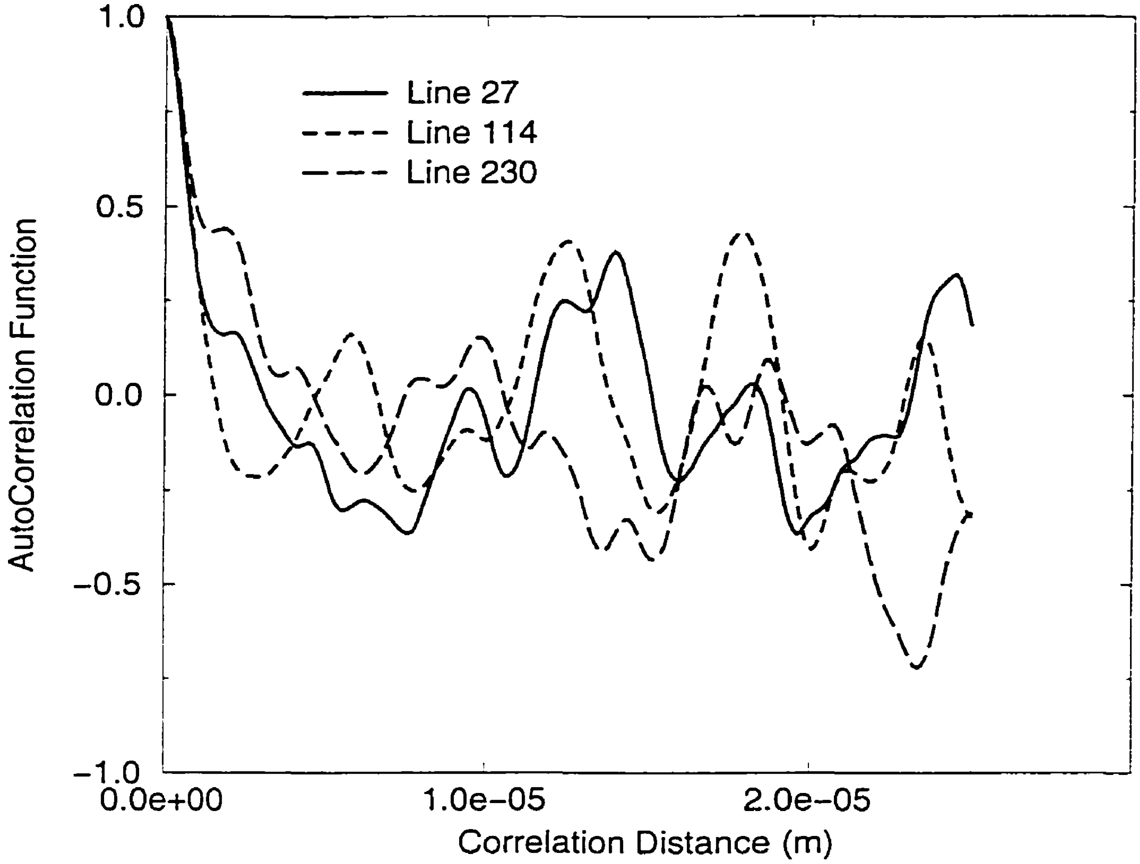

Figure 3-22: Lateral correlation functions for Lines 27, 114 and 230 of Sample G.

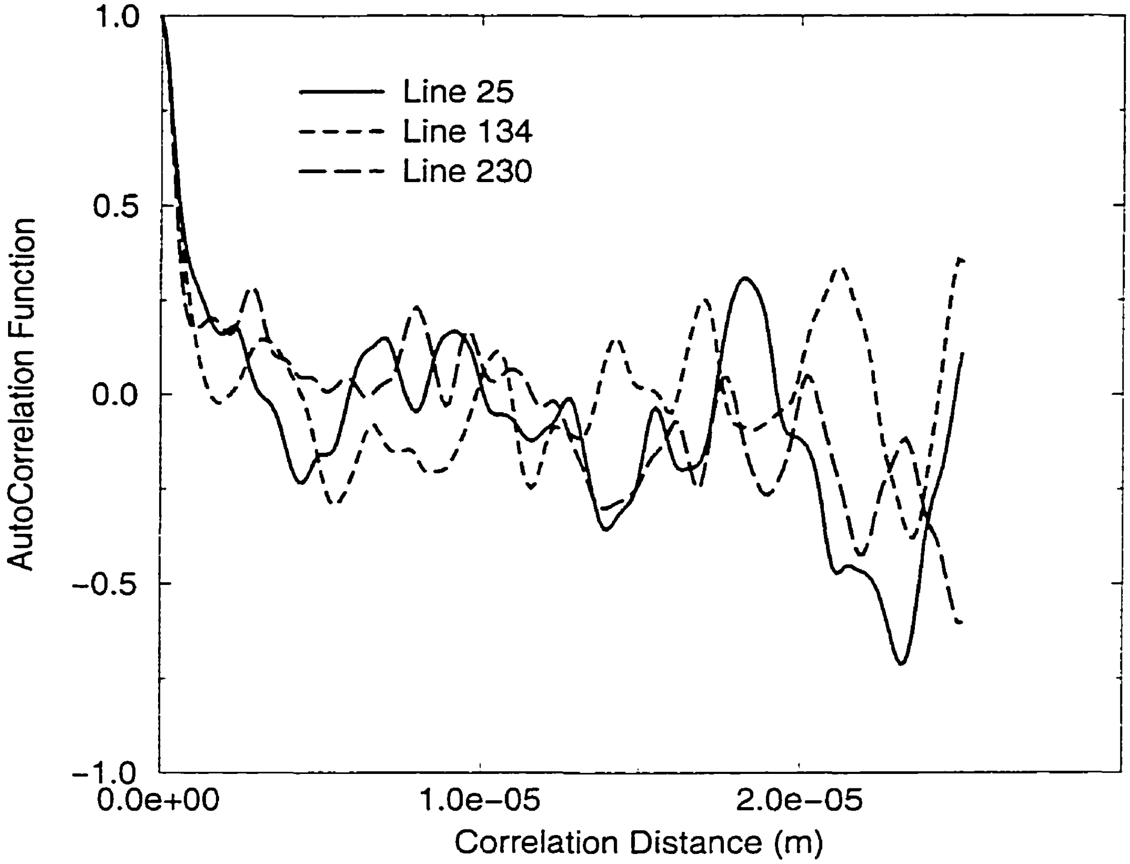

Figure 3-23: Lateral correlation functions for Lines 25, 134 and 230 of Sample J.

found for lines 47, 126 and 235, respectively. In physical terms, the correlation function represents how the roughness is distributed laterally, i.e. either they are segregated in certain areas of the surface or equally distributed over the surface. The lateral correlation length is the indicator of how regularly a pattern does repeat itself in a neighboring pattern that resembles its characteristics. In the case of Sample I, whose surface has domains of one micron in size on average, the local pattern that covers the surface is of the dimension of $3 \sim 4\mu$m. Figure 3-21 shows the lateral correlation function for Sample D outside surface at lines 41, 171 and 211. Using the same computing scheme, the lateral correlation length T was found to be $T = 3.05\mu\text{m}, 2.57\mu\text{m}, 3.30\mu\text{m}$. These values indicate that the local repeating pattern on the surface of Sample D is of the dimension of $2 \sim \mu$m, and is smaller than that of Sample I. The comparison is observed from the experimental images shown in Figure 3-5. Similarly, Figure 3-22 shows the lateral correlation function of Sample G at lines 27, 114 and 230. Figure 3-23 shows the lateral correlation function of Sample J at lines 25, 134 and 230.

The lateral correlation length T of all sample films are listed in Table 3.2.

Table 3.2: Lateral Correlation Length of Sample Films μm

	A	B	C	D	E	F	G	H	I	J	K	L	M
O	3.44	3.55	3.74	2.97	3.11	12.11	3.03	4.31	3.78	4.08	8.38	3.92	3.8
I	3.68	3.83	3.86	3.17	3.27	10.21	3.50	4.43	3.91	3.84	8.09	3.38	3.62

3.5.3 Line Fractal Dimension

Surface roughness can be evaluated in a variety of ways. The above mentioned standard deviation of roughness and lateral correlation function are among the most commonly used characterization methods for rough surfaces. These conventional characterization methods usually reduce all of the complex surface characteristics to one number and that frequently fails to capture all of the details and leads to a poor correlation between measurements and observations. The approach of fractal analysis is an attempt to describe the features of the rough surface in addition to conventional characterization methods.

The dimensions of Euclidean geometry are non-negative integers. The dimensions 0, 1, 2 and 3 correspond to dots, lines, planes and bodies, respectively. This simple classification is not able to capture all of the complex geometries observed in natural and artificial objects, especially for very irregular shapes. Fractal dimension was first introduced by Mandelbrot [29], to describe coast lines, which, unlike any other complex curves in mathematics, cannot be approximated by continuous line segments, regardless of the length of line segments. Such observation leads to the conclusion that coast lines have a dimension that lies between 1 and 2, i.e. a straight line and a plane.

Assume a continuous function $f(x)$. It follows that $|f(x+\Delta) - f(x)| \rightarrow 0$ as $\Delta \rightarrow 0$. This expresses the fact that over a short spatial distance Δ, the change in the function $f(x)$ can be arbitrarily small. The continuous property of $f(x)$, however, does not guarantee that it is differentiable. A differentiable function $f(x)$ requires not only continuity, but also that as $\Delta \rightarrow 0$, there exists a finite value $f'(x)$ such that:

$$f'(x) = \lim_{\Delta \rightarrow 0} \frac{f(x+\Delta) - f(x)}{\Delta} \tag{3.12}$$

The derivative has another meaning as the slope of the function f at point x.

The Lipschitz condition for a random process $f(x)$ limits the variation of the increments of f [29]:

$$var(f(x+\Delta) - f(x)) \sim \Delta^{2\alpha}, \quad \text{as} \quad \Delta \rightarrow 0 \tag{3.13}$$

Here the symbol $\sim$ means that the left hand side asymptotically approaches a constant times the right hand side as some limit is approached. α is referred to as the Lipschitz exponent and $0 < \alpha \leq 1$. If the profile of $f(x)$ is smooth, $\alpha = 1$.

The line fractal dimension is calculated from the so-called box-count algorithm given by Chesters [30]. The roughness profile is analyzed in terms of a "roughness spectrum", which gives the fractal dimension as a function of feature size. This method overlays the profile with a uniform grid or a set of boxes of height b. A count is made of the "non-empty" boxes (N) for which any portion of the profile falls within the box. The box size is then divided in half and the count repeated. The box dividing process continues until the box size is very close to the pixel size. The slope of the count as a function of box size on a log scale represents the Fractal Dimension value, R_f. Generally, if a profile is perfectly smooth and level (i.e., a straight line) then the dimension equals 1. This is because the number of boxes required to cover such a flat profile changes in exact linear proportion to the box size.

$$N \propto b^{-1} \tag{3.14}$$

If the profile is a rough curve, the boxes needed to cover it will increase more quickly when the size of the boxes decreases.

$$N \propto b^{(-R_f)} \tag{3.15}$$

The line fractal dimension R_f is used to measure the smoothness of surface profile with $1 < R_f < 2$. A higher value of line fractal dimension represents a very "broken" line. As $R_f \to 2$, the line is closer to a two dimensional area, meaning a dense distribution of roughness on the line. On the other end, a lower value of R_f represents a smoother line with less and sparsely distributed roughness. At the extreme when $R_f = 1$, the line is straight. It should be noted that in the graph for polyethylene film surface profiles, the lateral units are in μm, whereas the height is in nm. If presented in the same units, the surface is very close to being perfectly flat and it would be difficult to observe the surface profile.

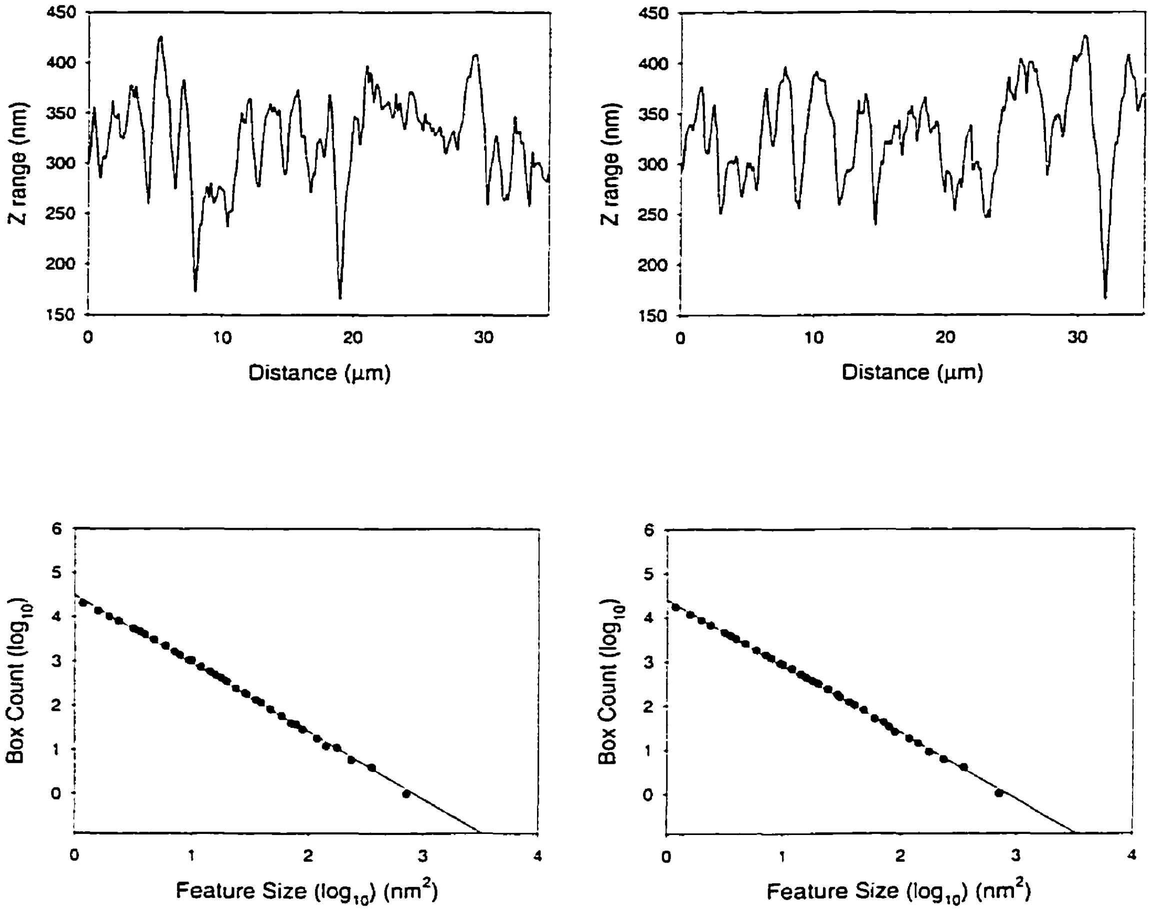

Figure 3-24: Surface profiles of line 133, and vertical line 153 of Sample D outside surface; their fractal dimensions are $R_{f133} = 1.52$ and $R_{fv153} = 1.51$.

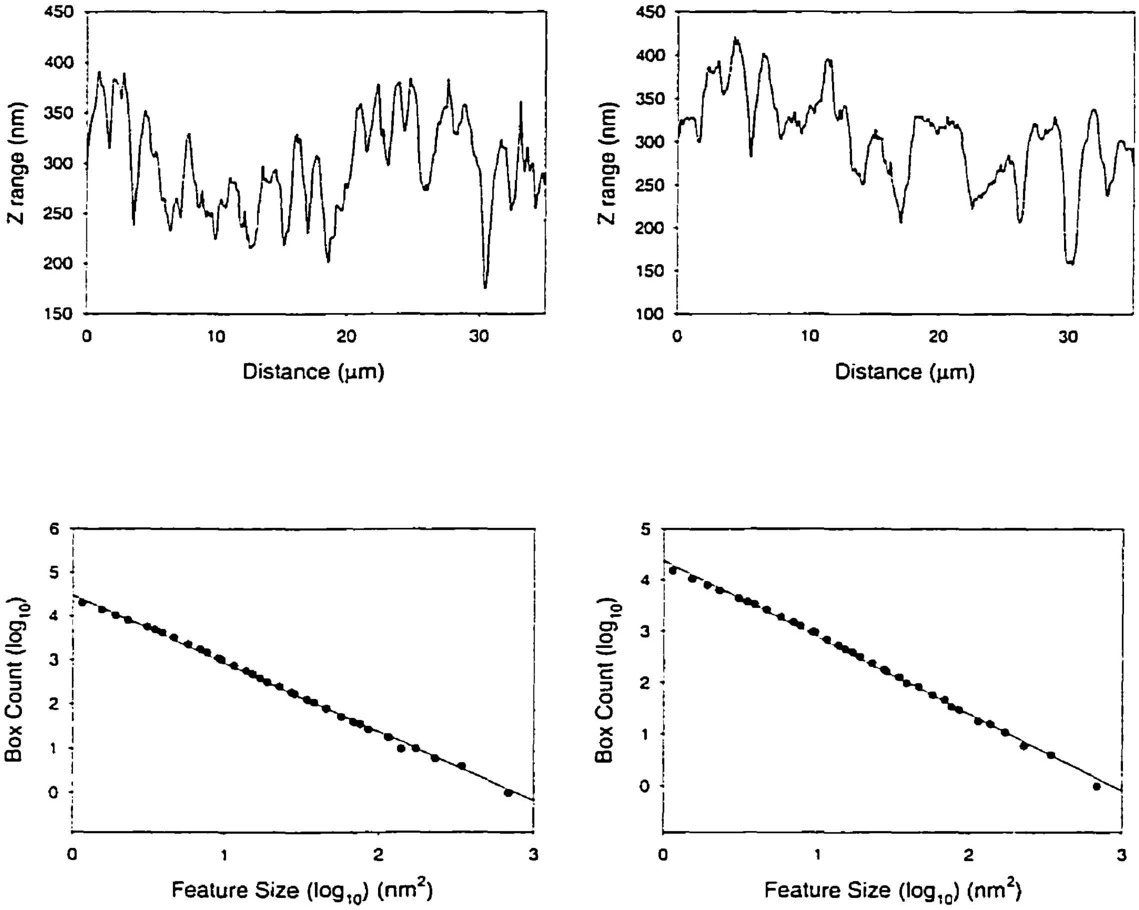

Figure 3-25: Surface profiles of line 140, and vertical line 166 of Sample D inside surface; their fractal dimensions are $R_{f140} = 1.48$ and $R_{fv166} = 1.49$.

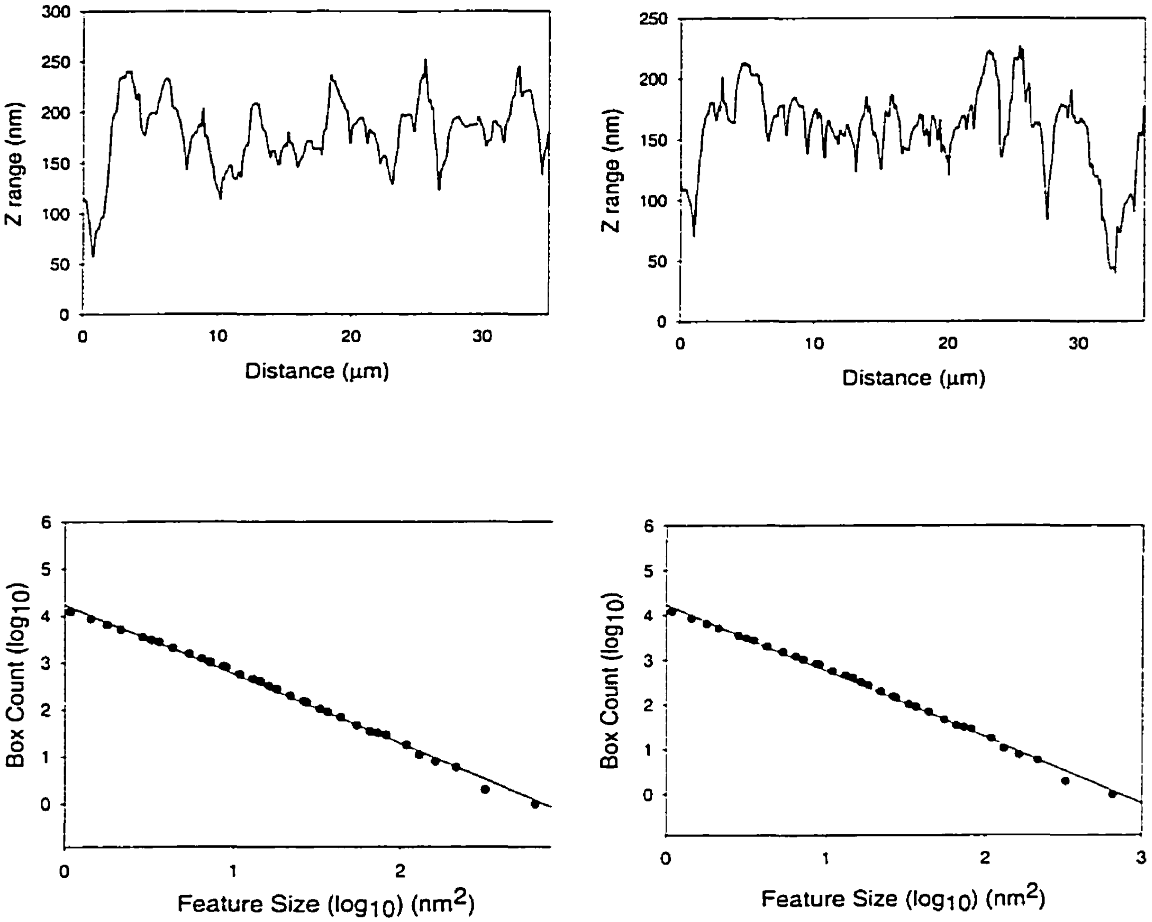

Figure 3-26: Surface profiles of line 123, and vertical line 135 of Sample I outside surface; their fractal dimensions are $R_{f123} = 1.48$ and $R_{fv135} = 1.48$.

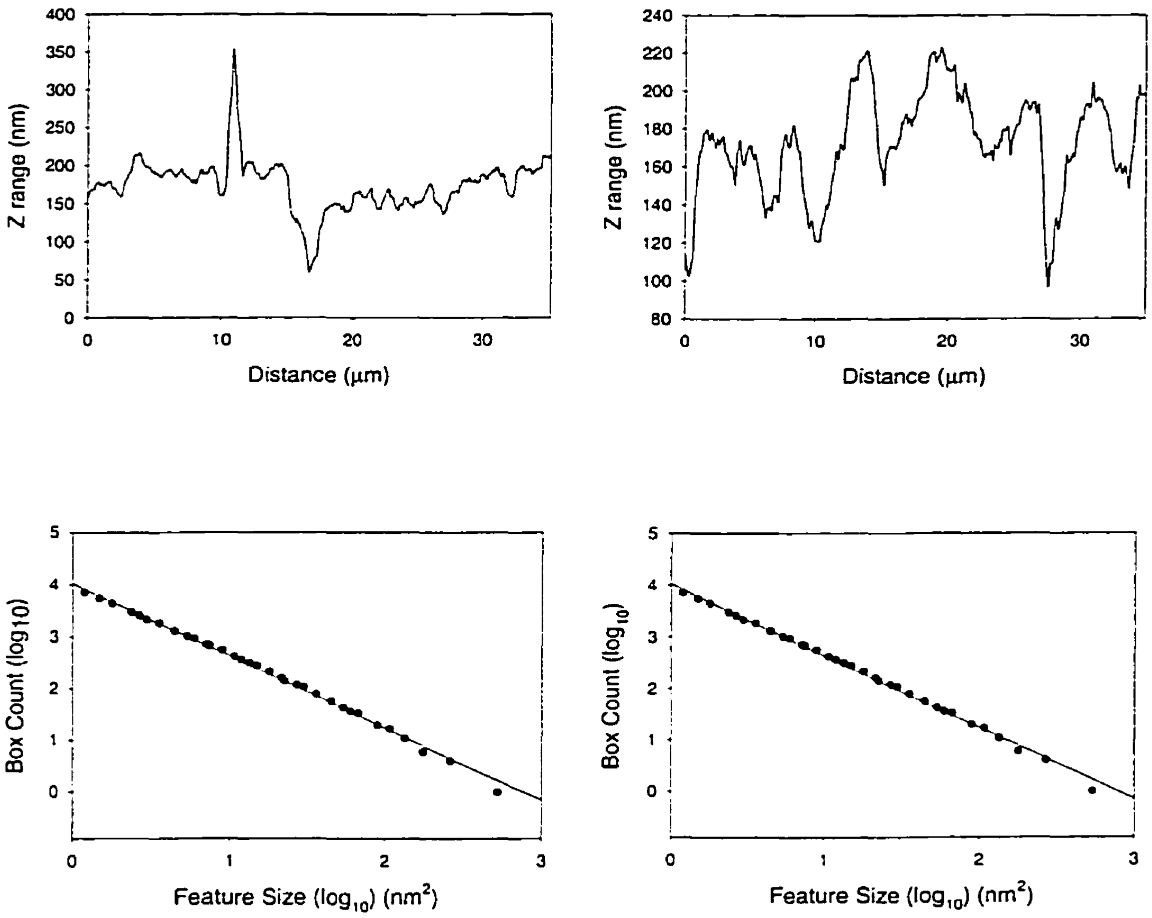

Figure 3-27: Surface profiles of line 107, and vertical line 121 of Sample I inside surface; their fractal dimensions are $R_{f107} = 1.44$ and $R_{fv121} = 1.44$.

As seen from Figures 3-24 to 3-27, the line fractal dimensions for horizontal and vertical (x and y) lines are the same for any sample. Similar to line roughness measurement earlier in this section, this suggests that the surface roughness distribution is the same in x and y directions and that there is no orientational preference of spherulites due to the extensional flow during the film blowing process.

The line fractal dimension of sample films are listed in Table 3.3.

Table 3.3: Line Fractal Dimension of Sample Films

	A	B	C	D	E	F	G	H	I	J	K	L	M
O	1.43	1.59	1.55	1.52	1.55	1.43	1.53	1.54	1.48	1.57	1.39	1.55	1.57
I	1.54	1.57	1.56	1.49	1.51	1.38	1.48	1.50	1.53	1.63	1.46	1.56	1.51

3.5.4 Two-Dimensional Fractal Dimension

A variety of surface structures such as aggregates, porous and highly dispersed materials exhibit rough surfaces that are best described in terms of fractal rather than Euclidean geometry [29].

The algorithm for 2D surface fractal dimension is given in Gomez-Rodriguez [31][32]. This method is called "Lake Pattern", since the analysis is based on lake patterns recognized on a Z plane intersecting the image. The relationship between two variables of each lake (the perimeter (L) as a function of area (A)) is evaluated. The fractal dimension D_f will be defined as:

$$L = \alpha D'_f A^{D'_f/2} \tag{3.16}$$

$$D_f = D'_f + 1 \tag{3.17}$$

where α is a constant, and D'_f is the fractal dimension of the lakes' coastline. D_f is the fractal dimension of the three dimensional surface.

Theoretically, the 2D fractal dimension indicates the extent to which the surface is "broken". Similar to the case of the one-dimensional fractal dimension, larger values of fractal dimension indicate a rougher surface in terms of smaller distributed roughness zones separated from each other. The boundaries of these roughness zones appear more randomly formed. On the other hand, a smaller fractal dimension, i.e. $D_f \approx 2$, represents a close-to-flat surface that has very slow changes in surface roughness and the boundaries of the roughness zones are smoother. $D_f = 2$ indicates a smooth surface that has no irregular roughness in Euclidean geometry.

Figure 3-28 and Figure 3-29 show the surface profiles of the outside and inside surfaces of Sample D of Set I. The spherulites on the outside surface appear to be smaller than the ones on the inside surface. Typical spherulite size of the outside surface is $0.2 \sim 0.4\mu$m and $0.4 \sim 0.7\mu$m for the inside surface. The sizes of the spherulites on the inside surface appear more diversified whereas the outside surface appears to be more uniform. The lakes found on the outside surface are smaller in circumference than those on the inside surface. Consequently, the fractal dimensions of the two surfaces are $D_{f\ out} = 2.57$ and $D_{f\ in} = 2.50$.

Similarly, Figure 3-30 and Figure 3-31 show the outside and inside surfaces of Sample D_{82} of Set II. Figure 3-32 and Figure 3-33 show both surfaces of Sample D_{84} of Set II.

The fractal dimensions of the two surfaces of sample D_{82} are $D_{f\ out} = 2.46$ and $D_{f\ in} = 2.44$. For sample D_{84}, $D_{f\ out} = 2.49$ and $D_{f\ in} = 2.43$. Between the two samples in Set II, the two surfaces of sample D_{82} are closer in terms of surface profile. In addition, D_f of Sample D of Set I is larger than those of the corresponding ones in Set II. This is in agreement with the observations that the spherulites on the surfaces of samples in Set II are considerably larger than those of Sample D in Set I.

The surface fractal dimensions of sample films are listed in Table 3.4.

Conclusions can be drawn from the 2-D fractal dimension measurements of various

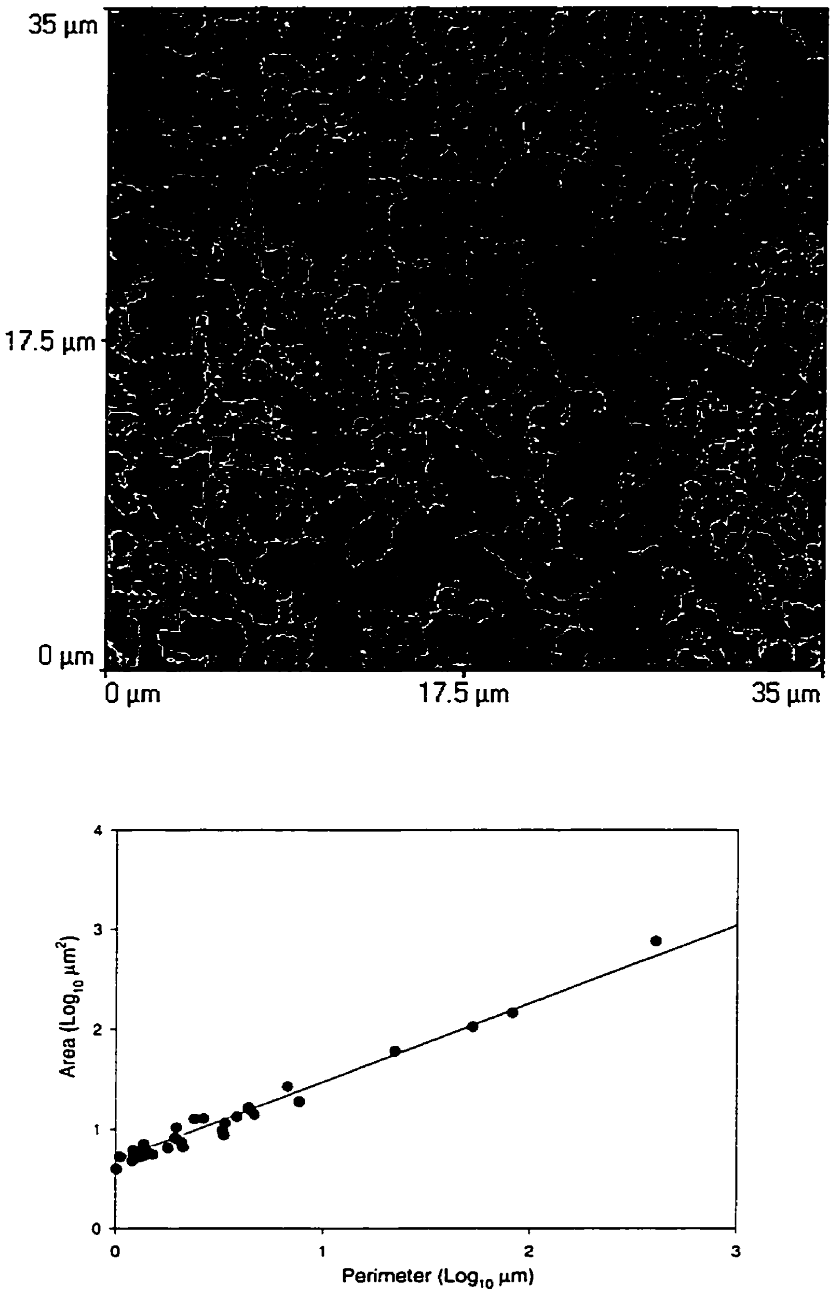

Figure 3-28: Lake Pattern of Set I Sample D outside surface; $D_f = 2.57$

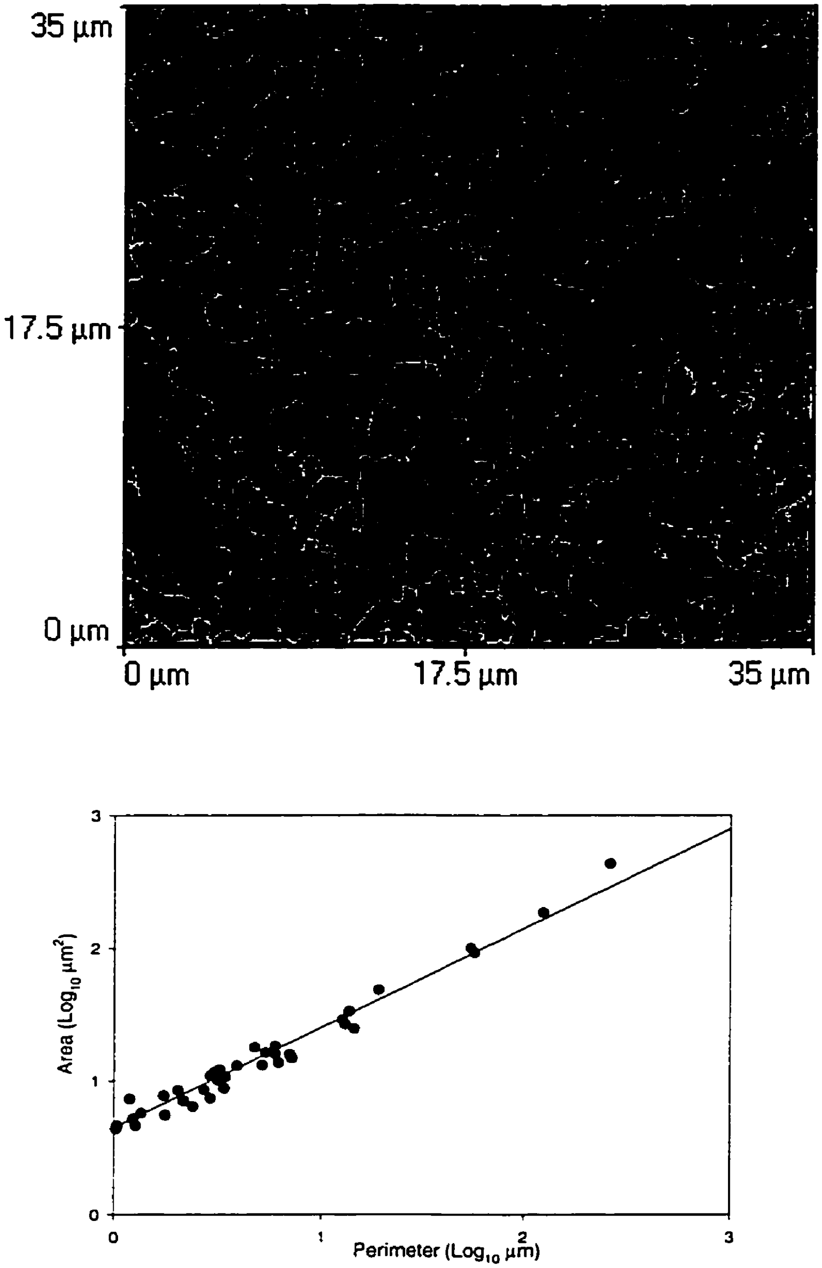

Figure 3-29: Lake Pattern of Set I Sample D inside surface; $D_f = 2.50$

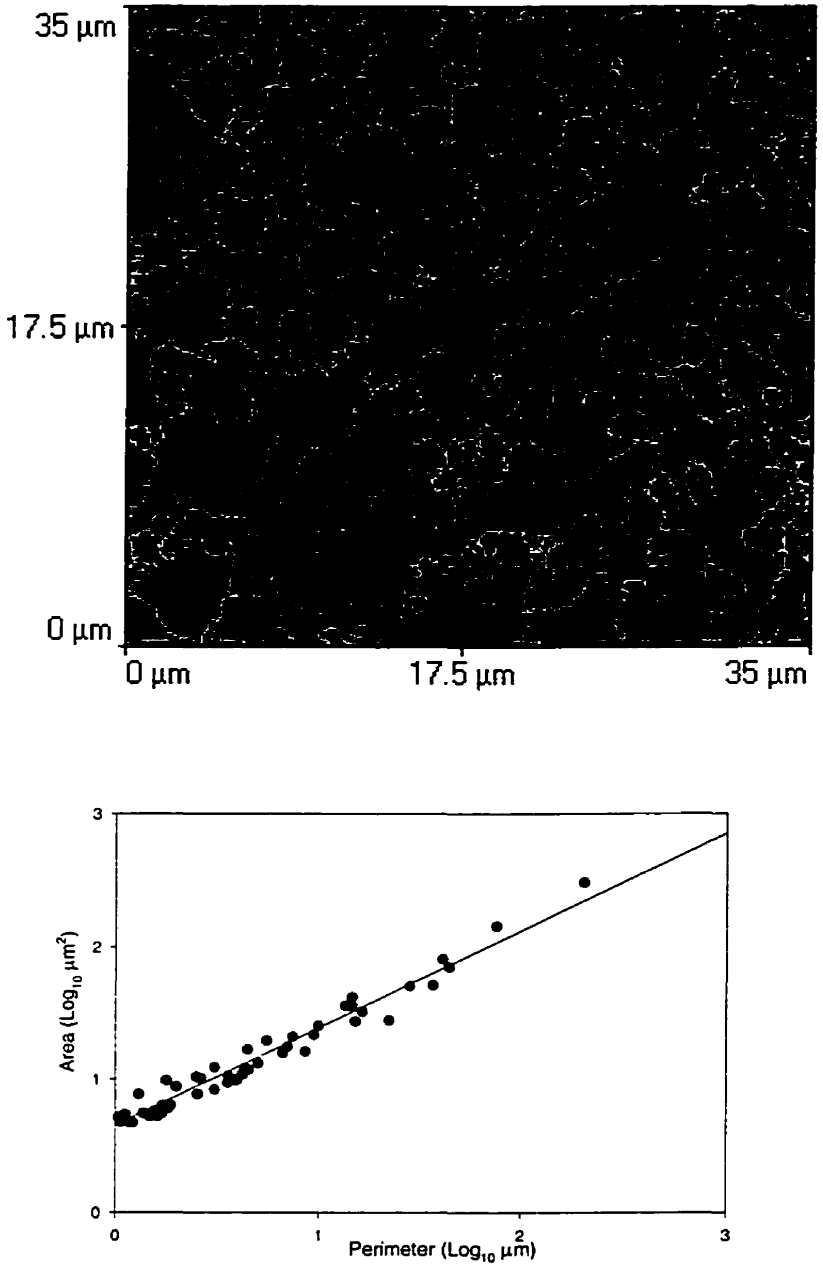

Figure 3-30: Lake Pattern of Set II Sample D_{82} outside surface: $D_f = 2.46$

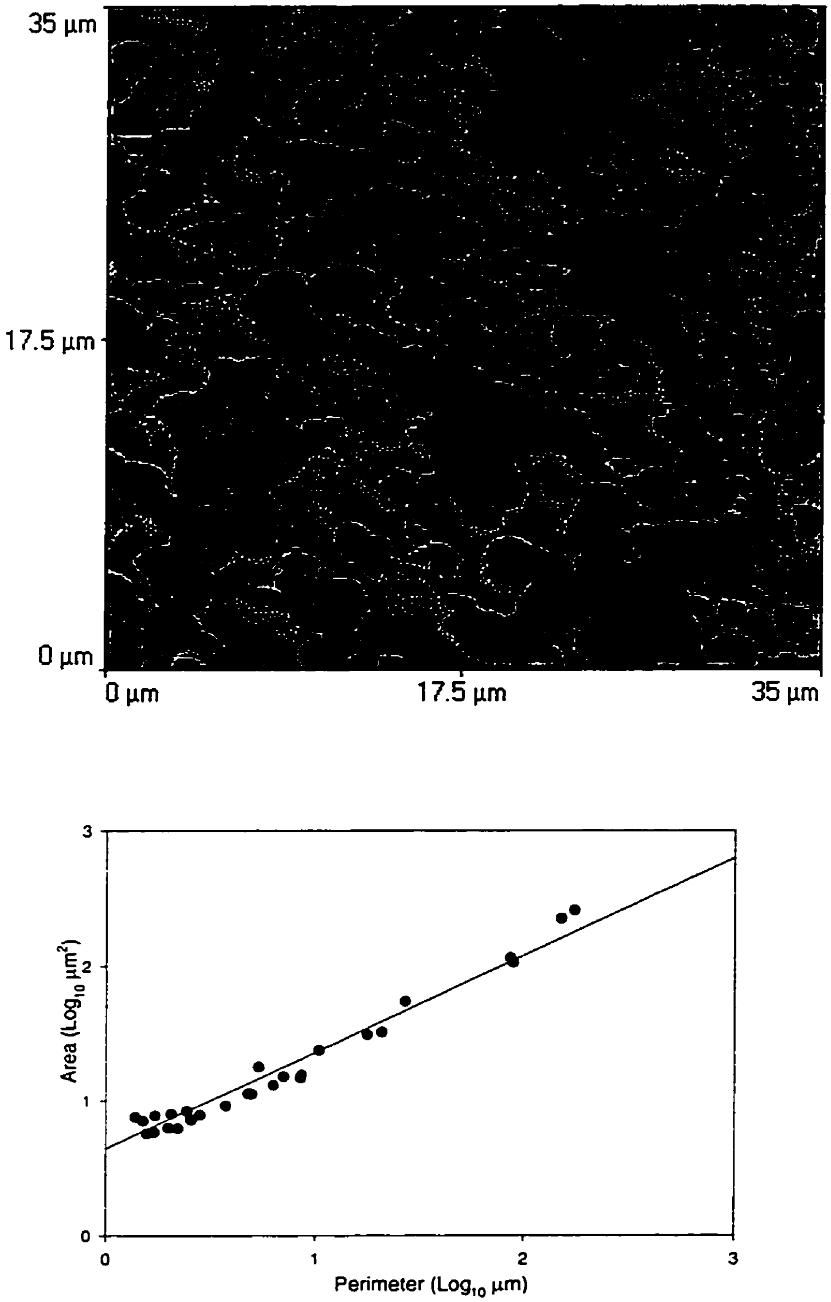

Figure 3-31: Lake Pattern of Set II Sample D_{82} inside surface; $D_f = 2.44$

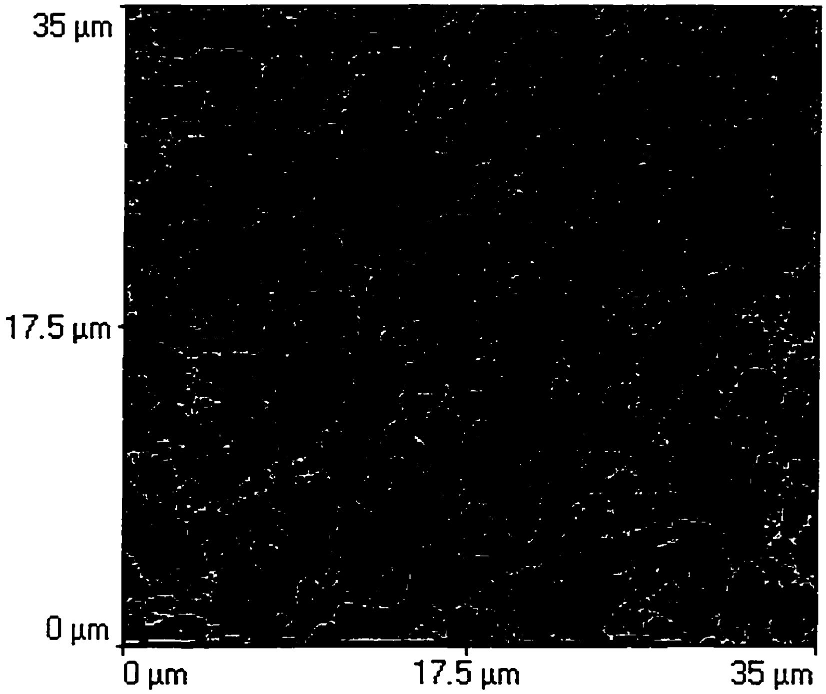

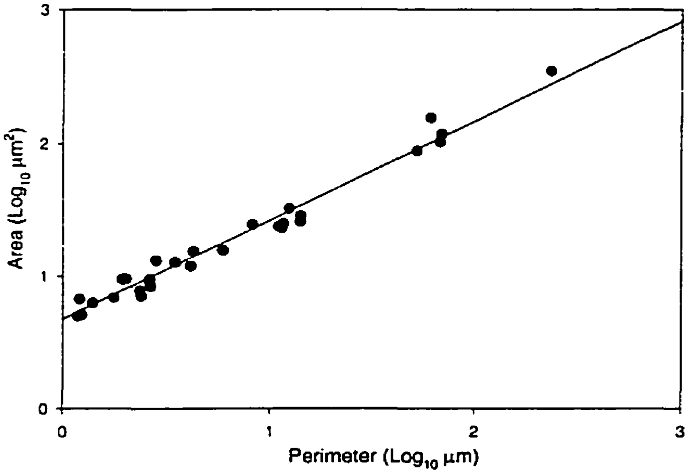

Figure 3-32: Lake Pattern of Set II Sample D_{84} outside surface; $D_f = 2.49$

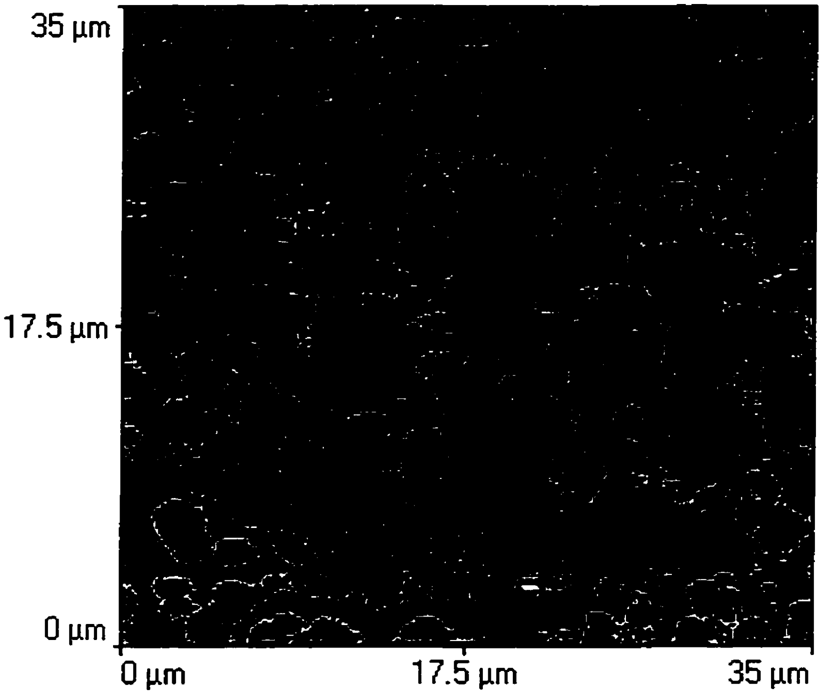

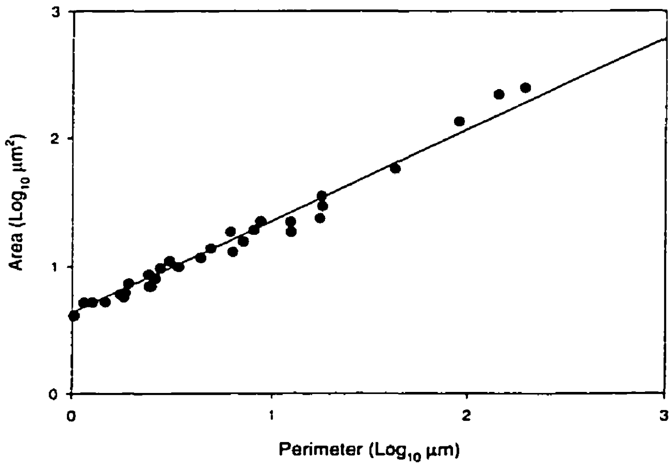

Figure 3-33: Lake Pattern of Set II Sample D_{84} inside surface; $D_f = 2.43$

Table 3.4: Two-Dimensional Fractal Dimension of Sample Films

	A	B	C	D	E	F	G	H	I	J	K	L	M
O	2.58	2.56	2.52	2.57	2.52	2.30	2.57	2.52	2.46	2.57	2.29	2.49	2.57
I	2.47	2.63	2.60	2.50	2.50	2.27	2.55	2.51	2.49	2.60	2.38	2.48	2.51

sample films regarding their surface textures. In general, the inside surface of a film is relatively smoother than the outside surface due to the difference in cooling during the film blowing process. However, the differences are not large. The spherulites on the inside surfaces are on average larger than the ones observed on the outside surface. This difference is indicated by the fact that the fractal dimensions of the inside surface for any sample film are lower than those of the outside surface, which confirms the observation and computation of the line fractal dimension made earlier.

3.5.5 Spherulite Size Distribution

Surfaces of sample films contain sperhulites of various sizes. Spherulites are separated using the "slope" method. At any given point (x_0, y_0, z_0) on a surface $\xi(x, y, z)$, the gradient of the surface is given by:

$$\text{ß} = \nabla\xi = (\frac{\partial\xi}{\partial x}, \frac{\partial\xi}{\partial y}, \frac{\partial\xi}{\partial z}) \tag{3.18}$$

The slope is given by:

$$s = \frac{\frac{\partial\xi}{\partial z}}{\sqrt{(\frac{\partial\xi}{\partial x})^2 + (\frac{\partial\xi}{\partial y})^2}} \tag{3.19}$$

To separate domains on the surface profile, a subroutine will scan the surface for points with slopes above a predetermined threshold. Such points are considered to be on the perimeter of domains. The tracing of the perimeter is done by checking the slopes of the neighboring points. The algorithm will iterate until all of the points on the perimeter

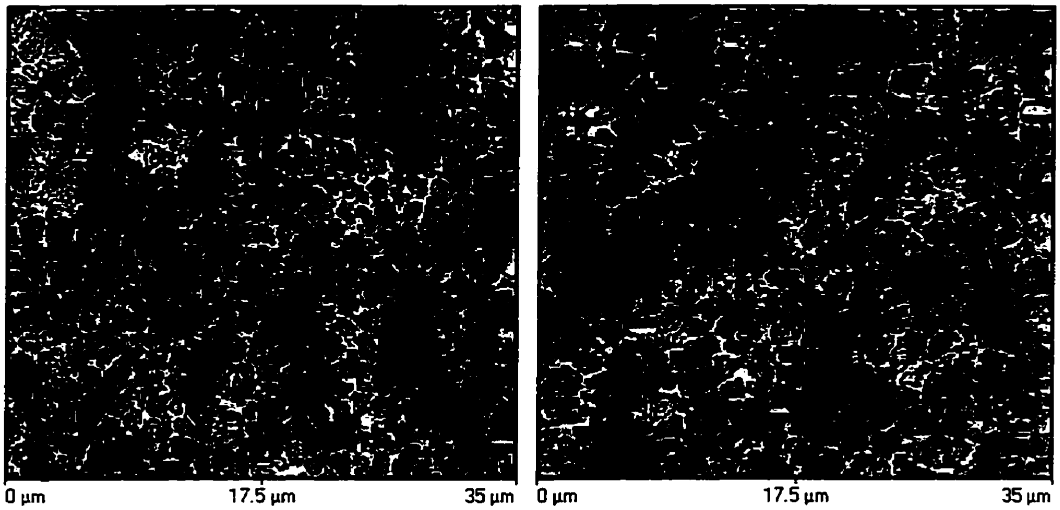

Sample D

Sample G

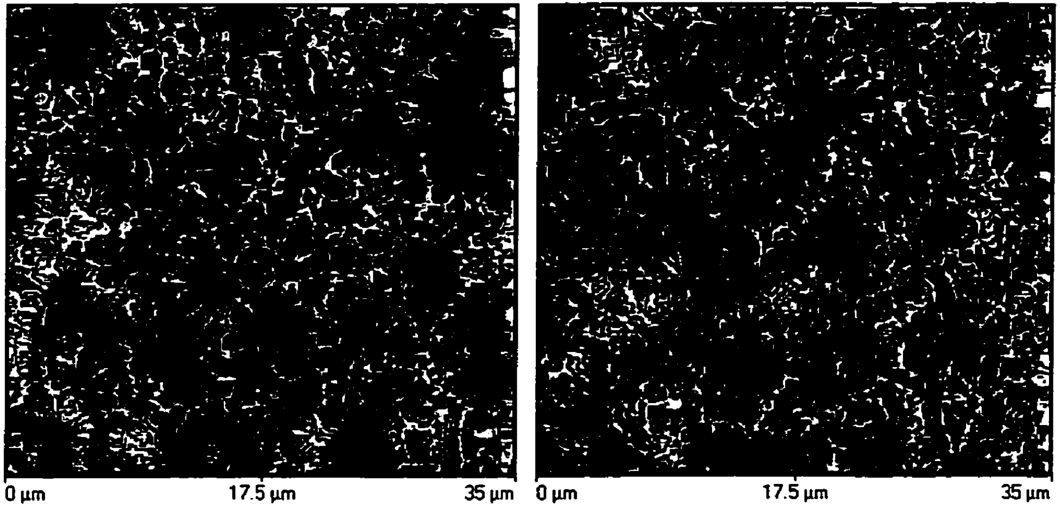

Sample I

Sample J

Figure 3-34: Spherulite analysis of Samples D, G, I and J

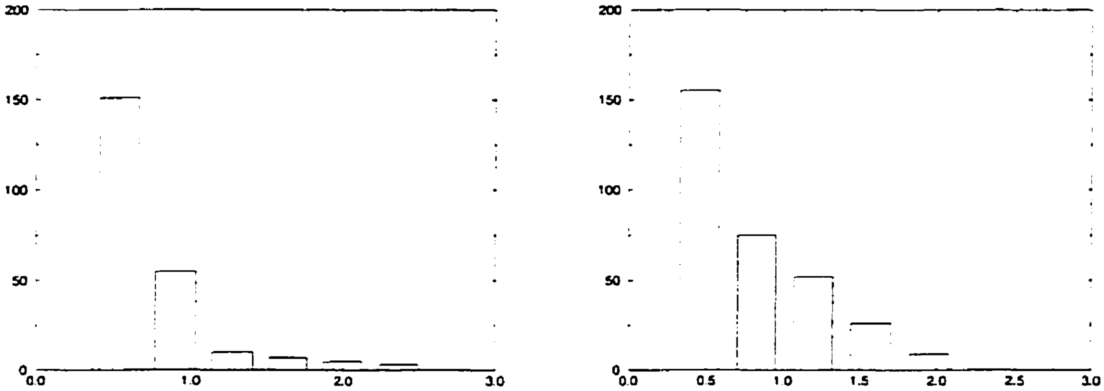

Sample D

Sample G

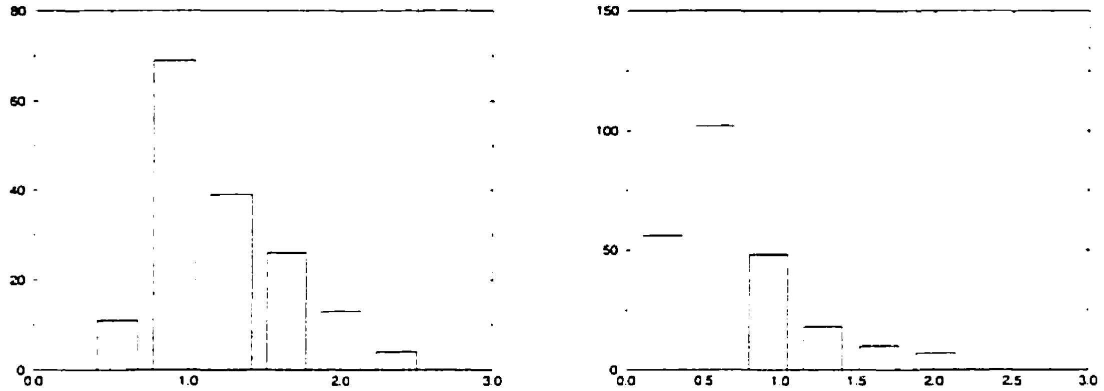

Sample I

Sample J

Spherulite Size (μm)

Figure 3-35: Spherulite count of Samples D, G, I and J of a single domain are found. Once the perimeter is established for a single domain, the surface area and volume of the domain are computed by integrating over the points inside the perimeter. This procedure is repeated over the entire region of interest. By experimenting with different values of the slope for the separation of domain structures, an optimum value of 1 is selected for all samples. The results for samples shown in Figure 3-5 are presented in Figure 3-34. The number densities of spherulites of sample surfaces in Figure 3-34 are presented in Figure 3-35.

3.6 Summary

A thorough AFM/NSOM study of polyethylene blown film morphology is conducted. It presents a rigorous and comprehensive approach to characterize the morphology of polymer films. Observations from morphological information conclude the existance of the spherulitic structure on the surface as well as in the bulk of the sample films. All samples exhibit similar surface structures. However, it differs in size and distribution of spherulites among sample films. The surface roughness of sample films is caused by nucleation on and beneath the surface. The formation and shape of the spherulites did not show any orientation due to the extensional and enlongational flow during the film blowing process. The distribution of spherulites does not show any clustering or preferred pattern. The spherulites are randomly distributed on the surface.

Resin composition and processing conditions appear to play a critical role in the formation of the surface roughness. Detailed knowledge regarding the formation of the film morphology as functions of resin composition and processing conditions requires detailed knowledge of crystallization kinetics, including nucleation and growth of spherulites. It is also needed to couple such knowledge in a comprehensive realistic model of the film blowing process.

The surface morphology is characterized using parameters such as the standard deviation of surface roughness, lateral correlation length and fractal dimensions. These characterization methods provide quantitative ways to study surface morphology. Since this methodology is not material-dependent, it can be applied to all kinds of rough surfaces.

Chapter 4

Surface Reflection and Gloss

4.1 Introduction

4.1.1 Gloss: Specular reflection

For a well polished or perfectly smooth surface, i.e. mirror, light is reflected in a directive manner according to the laws of classical optics, whereas a plane with a rough surface (wall, white paper, plastic film, etc) will scatter the incident light in all directions. The scattered field in such cases is considered to be the sum of two components: the specular component and the diffuse component. Specular reflection is the same as the reflection off a smooth surface. It is directional and obeys the laws of classical optics. Diffuse scattering, on the other hand, contains a larger area and shows little directivity. Gloss is defined as the optical property that measures the ratio between the specularly reflected intensity and the incident light intensity. Because the reflection of incident light depends largely upon the surface onto which the reflection occurs, gloss is closely associated with the surface roughness of the material. In the case of polymer films, gloss is not only a function of the surface profile but also are intrinsic material property as well, i.e. the refractive index of the polymer film. For the same polymer resin, the refractive index of the crystalline state is usually different from that of the amorphous state. However, such difference is small and is usually neglected in the study of surface reflections. Therefore, the refractive index of a polymer film here depends only upon the chemical composition of the resin from which the film is made. The main interest in this study is to evaluate the surface roughness and its effect on gloss. In industrial standards, specular gloss is defined as the relative luminous reflectance factor of a specimen in the mirror direction [6]. Here, the relative luminous reflectance factor is the ratio of the luminous flux reflected from a specimen compared to a standard surface under similar geometric conditions. For the purpose of measuring specular gloss, the standard background surface is polished glass.

The surface roughness depends largely on what occurs during solidification, in addition to thermo-mechanical history experienced by the material during the film blowing process. The solidification behavior of the material is related to the chemical composition of the resin and the additives, such as nucleating agents and clarifying agents. The surface roughness is associated with the crystalline morphology and deformation-related defects that are obtained during the melt flow in film blowing. The addition of nucleating agents can produce different effects in the blowing process. In the presence of such agents, the polymer exhibits a higher density of nuclei at the start of the crystallization. This would, however, usually be associated with smaller spherulites in the final product. Furthermore, nucleating agents on or near the surface contribute to surface irregularities.

A general review of the relation between gloss and surface topography is given by Whitehouse [33]. Most of the work in the area of surface gloss has been devoted to paper coating techniques, paints and associated topics. Lettieri [28] has applied angle-resolved light scattering (ARLS) to measuring surface roughness of paper coating, by obtaining the ARLS patterns of laser light scattered from glossy paper samples and then comparing them with patterns calculated using the theoretical model based on plane-wave scattering from an isotropic rough surface. Some other research in this area includes the work of Mendez [34] on the gloss of paper coating. Published theoretical assessment of gloss is limited. A general expression based on the scalar Kirchhoff solution was proposed by Alexander-Katz [35]. The author proposed an analytical solution to describe surface roughness using two statistical parameters, i.e. the standard deviation value of surface height and the lateral correlation length L_c. Assuming an exponential distribution and Gaussian correlation function, an analytical solution for the surface reflection was derived. Because of the lack of experimental data, the model could not be validated. The theoretical basis used to determine the far field intensity distribution by reflection of the electro-magnetic wave from a rough surface, characterized by statistical properties, has been established in the works of Davies [36] and Beckmann [37].

In this work, the generally accepted Beckmann approach for theoretical and numerical assessment of reflection from the surface of polyethylene blown films is applied. The surface roughness information is gathered using the AFM method as mentioned earlier.

4.1.2 Experimental Measurement of Gloss

According to Hunter [38], "Gloss is defined as the degree to which a surface simulates a perfect mirror in its capacity to reflect incident light"; also"gloss is determined by the surface's geometric selectivity in reflecting light". In most practical glossmeters, specular gloss is the property determined. This is usually taken to be the fraction of incident light flux reflected in the direction of mirror reflection (the specular direction) when a specimen is illuminated by a parallel light beam.

Gloss measurements of all of the sample films supplied by NOVA Chemicals were conducted in accordance with standard ASTM D2457-90. The apparatus used is shown in Figure 4-1[6]. As shown, unpolarized white light from an incandescent lamp is concentrated by a condenser lens onto the source field aperture, which lies in the focal plane of the source lens. The resulting parallel beam is reflected at the surface of the test

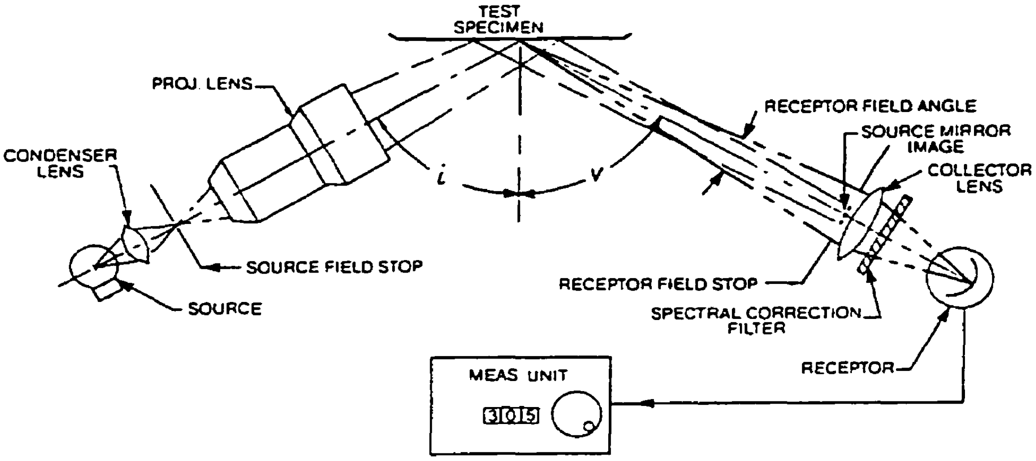

Figure 4-1: Diagram of Glossmeter showing essential components and dimensions.

sample and then collected by the receptor lens. The receptor field aperture lies in the back focal plane of the receptor lens, and the image of the source field aperture formed after reflection in the sample surface lies wholly within it. Specular reflection is thus determined by the ratio of the reflected intensity I_r and the incident intensity I_o.

4.2 Reflection by Rough Surface

For a perfectly smooth surface, the specular reflection is given by the reflection coefficient R_s which is given by the Fresnel equation [7].

$$\begin{aligned} R_s &= \frac{I_r}{I_0} \\ &= \frac{1}{2}[(\frac{\cos i - \sqrt{n^2 - \sin^2 i}}{\cos i + \sqrt{n^2 - \sin^2 i}})^2 + (\frac{n^2 \cos i - \sqrt{n^2 - \sin^2 i}}{n^2 \cos i + \sqrt{n^2 - \sin^2 i}})^2] \end{aligned} \tag{4.1}$$

where R_s is the specular reflectance. I_r and I_0 are the reflected and incident intensities, respectively. n is the refractive index of the material and i the incident angle. The Fresnel equation shows that the reflection of a smooth surface is only a function of refractive index of the sample and the incident angle. In the case of polymer films, there is a variation in reflection due to the roughness of the surface that scatters the incident light in all directions, causing the reduction of intensity in the specular direction and an increase in diffuse reflection. Such a variation is characterized by the Kirchhoff solution [37].

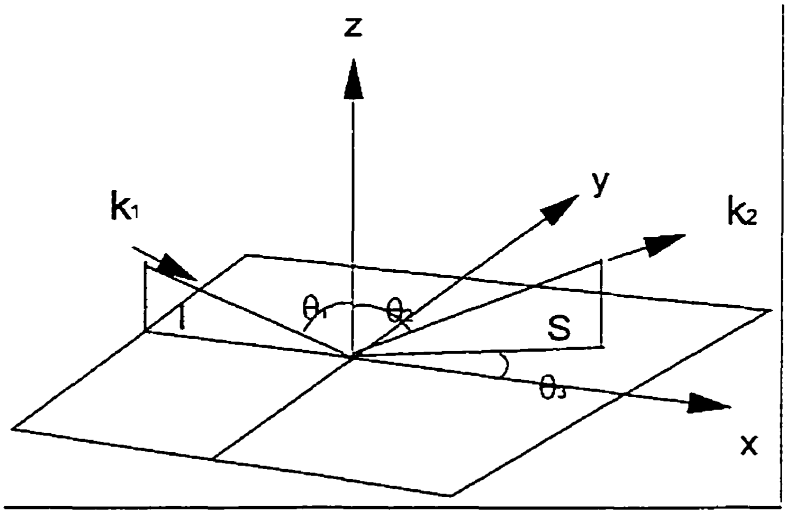

Figure 4-2: The general scattering geometry; k_1 and k_2 are the incident flux vector and reflected flux vector, respectively; θ_1 and θ_2 are the incident angle and reflected angle, respectively; θ_3 is the lateral displacement angle; I is the incident plane and S is the scattered plane.

The general, scattering geometry is illustrated in Figure 4-2. The angle of incidence, between the direction of propagation k_1 and the z axis , is denoted by θ_1. The scattering angle, between the direction of reflected flux k_2 and the z axis, is θ_2. For lateral scattering out of the plane of incidence, a third angle θ_3 is introduced, representing the azimuthal angle. Introducing a new vector $v = k_1 - k_2$, in Cartesian coordinates [37]:

$$v = (v_x, v_y, v_z) = \frac{2\pi}{\lambda}(\sin\theta_1 - \sin\theta_2\cos\theta_3, \quad -\sin\theta_2\sin\theta_3, \quad \cos\theta_1 + \cos\theta_2) \qquad (4.2)$$

For any surface given by $z = \xi(x, y)$, the scattering factor ρ, defined as the ratio between the reflected intensity of a rough surface and the reflected intensity of a smooth surface under the same geometric conditions, is given as a function of the surface profile and reflection coefficient for a smooth surface in two dimensions [37]:

$$\rho = \frac{1}{4XY\cos\theta_1}\int_{-X}^{X}\int_{-Y}^{Y}(a\frac{\partial\xi}{\partial x} + c\frac{\partial\xi}{\partial y} - b)e^{i\mathbf{v}\cdot\mathbf{r}}dxdy \tag{4.3}$$

here,

$$\begin{aligned} a &= (1 - R_s)\sin\theta_1 + (1 + R_s)\sin\theta_2\cos\theta_3 \\ b &= (1 + R_s)\cos\theta_2 + (1 - R_s)\cos\theta_1 \\ c &= (1 + R_s)\sin\theta_2\sin\theta_3 \end{aligned} \tag{4.4}$$

where R_s is the reflection coefficient of a smooth surface given by the Fresnel equation under identical geometrical conditions and the surface vector $\mathbf{r} = (x, y, \xi(x, y))$. This is the general Kirchhoff solution for rough surfaces.

After integration by parts:

$$\begin{aligned} \rho = \frac{1}{4XY\cos\theta_1}\{(b + \frac{av_x + cv_y}{v_z})\int_{-X}^{X}\int_{-Y}^{Y}e^{i\mathbf{v}\cdot\mathbf{r}}dxdy \\ -\frac{ic}{v_z}\int_{-X}^{X}e^{i\mathbf{v}\cdot\mathbf{r}}|_{-Y}^{Y}dx - \frac{ia}{v_z}\int_{-Y}^{Y}e^{i\mathbf{v}\cdot\mathbf{r}}|_{-X}^{X}dy\} \end{aligned} \tag{4.5}$$

At the specular direction, $\theta_1 = \theta_2$ and $\theta_3 = 0$. $\mathbf{v} = (0, 0, 2\cos\theta_1)$, $\mathbf{v}\cdot\mathbf{r} = (0, 0, 0)$ and from equation (12) $a = 2\sin\theta_1$, $b = 2\cos\theta_1$ and $c = 0$. Therefore, the larger is the surface roughness, the larger will be the derivative terms, and the stronger will be the effect of surface roughness on the specular reflected intensity. For a smooth surface, $\xi(x, y) = 0$ for all (x, y), the derivatives in equation 4.3 would vanish and the reflection coefficient would be the same as R_s given by the Fresnel equation.

From the above equations, consider the mean value of the integral

$$\begin{aligned} < \int_{-X}^{X}\int_{-Y}^{Y} e^{i\mathbf{V}\cdot\mathbf{r}} dxdy > &= \int_{-X}^{X}\int_{-Y}^{Y} e^{i(v_x x+v_y y)} < e^{iv_z\xi} > dxdy \\ &= < e^{iv_z\xi} > \int_{-X}^{X}\int_{-Y}^{Y} e^{i(v_x x+v_y y)} dxdy \end{aligned} \tag{4.6}$$

Assume the random surface ξ is isotropically rough, satisfies the same statistical distribution $w(z)$ in all directions over the surface, which is very close to reality illustrated by the experimental images shown in later sections. Then the mean value, which is the one-dimensional characteristic function $\chi(z)$ of a random surface is given by

$$\chi(v_z) =< e^{iv_z\xi} >= \int_{-\infty}^{\infty} w(z)e^{iv_z\xi}dz \tag{4.7}$$

In the case of the one dimensional Gaussian distribution, with a standard deviation of σ,

$$w(z) = \frac{1}{\sigma\sqrt{2\pi}}e^{-\frac{z^2}{2\sigma^2}} \tag{4.8}$$

It follows that, for the reflecting area $A = 4XY$, the mean scattering factor is:

$$< \rho >= \frac{1}{A}\int_{-X}^{X}\int_{-Y}^{Y} e^{iv_x x+iv_y y} < e^{iv_z\xi} > dxdy = \chi(v_z)\rho_0 \tag{4.9}$$

where

$$\rho_0 = A\frac{\sin v_x \sin v_y}{v_x v_y} \tag{4.10}$$

Since $A \gg \lambda^2$, ρ_0 will equal unity for $v_x = v_y = 0$, for the specular direction of

$$\theta_1 = \theta_2, \qquad \theta_3 = 0 \tag{4.11}$$

but it drops to zero rapidly as soon as θ_2 leaves the specular direction. Therefore, the mean scattering factor $< \rho >$ would be infinitismal anywhere in the space, except for a very narrow cone along the specular direction. For the ideal mirror surface, the scattering factor is zero everywhere, except in the specular direction.

To simplify the analysis, assume a random rough surface, with a Gaussian height distribution function. Further, assume the surface is isotropic, i.e. the distribution of roughness is identical in all directions. Therefore, the lateral correlation length T is the same in all locations and directions and the lateral correlation function $C(\tau)$ is one-dimensional. The experimental results are presented to validate this assumption in the following sections.

The field distribution $D(\theta_2, \theta_3)$ of the diffuse light scattered by an isotropic surface in the direction (θ_2, θ_3) is given by Beckmann and Spizzichino [37]:

$$D(\theta_2, \theta_3) = \frac{2\pi[F(\theta_2, \theta_3)]^2}{A} \int_0^\infty J_0[v_{xy}(\theta_2, \theta_3)\tau](exp\{-g(\theta_2)[1 - C(\tau)]\} - exp[-g(\theta)])\tau d\tau \tag{4.12}$$

where θ_3 is the azimuthal angle in the reflected field, J_0 is the Bessel function of the $0th$ order and

$$v_{xy}(\theta_2, \theta_3) = \frac{2\pi}{\lambda}(\sin^2\theta_1 + 2\sin\theta_1\sin\theta_2\cos\theta_3 + \sin^2\theta_2)^{1/2} \tag{4.13}$$

$$g(\theta_2) = [\frac{2\pi\sigma}{\lambda}(\cos\theta_1 + \cos\theta_2)]^2 \tag{4.14}$$

$$F(\theta_2, \theta_3) = \frac{1 + \cos\theta_1\cos\theta_2 - \sin\theta_1\sin\theta_2\cos\theta_3}{\cos\theta_1(\cos\theta_1 + \cos\theta_2)} \tag{4.15}$$

From the above equations, the entire field vector distribution can be determined. In particular, $D(\theta_1, 0)$ represents the flux in the specular direction. Using the lateral correlation function defined above, the angular intensity distribution is computed by the following equation at the incident scattering plane, i.e. $\theta_3 = 0$

$$I(\theta_2) = [F(\theta_2, 0)]^2 \int_0^\infty J_0(v\tau) exp(-g)[g exp(-(\frac{\tau}{T})^\alpha) - 1]\tau d\tau \tag{4.16}$$

where the function v is given by

$$v(\theta_2) = \frac{2\pi}{\lambda} |\sin\theta_1 + \sin\theta_2|. \tag{4.17}$$

Following the computation scheme described above, the reflected field from a rough surface is then determined using equations (4.12) through (4.16). Various field distributions were computed for different rough surfaces. The focus is to study the correlation between reflection from a rough surface and its characteristics. Intensity distributions were computed for simulated surfaces with different values of standard deviation of surface height, lateral correlation length, and incident angles. Also for all of the sample films included in this study, reflected intensity was computed based on the AFM images. The gloss of these samples was estimated from the intensity distributions.

4.3 Results and Discussion

As previously stated, gloss is a term used to describe the amount of mirror-like (specular) reflection relative to the incident intensity. Because of the surface roughness observed in the samples, any incident light will be scattered over a range of angles, causing the reduction of specular intensity and the increase of diffused intensity. The reflected intensity distribution is computed by equation (4.16) from the reflection theory for rough surfaces. To study the effect of surface roughness on the intensity distribution, reflected intensity distribution on the incident plane, i.e. $\theta_3 = 0$, is computed for different values of surface height and different values of lateral correlation length for a simulated rough surface with a Gaussian distribution function.

4.3.1 Influence of Surface Roughness

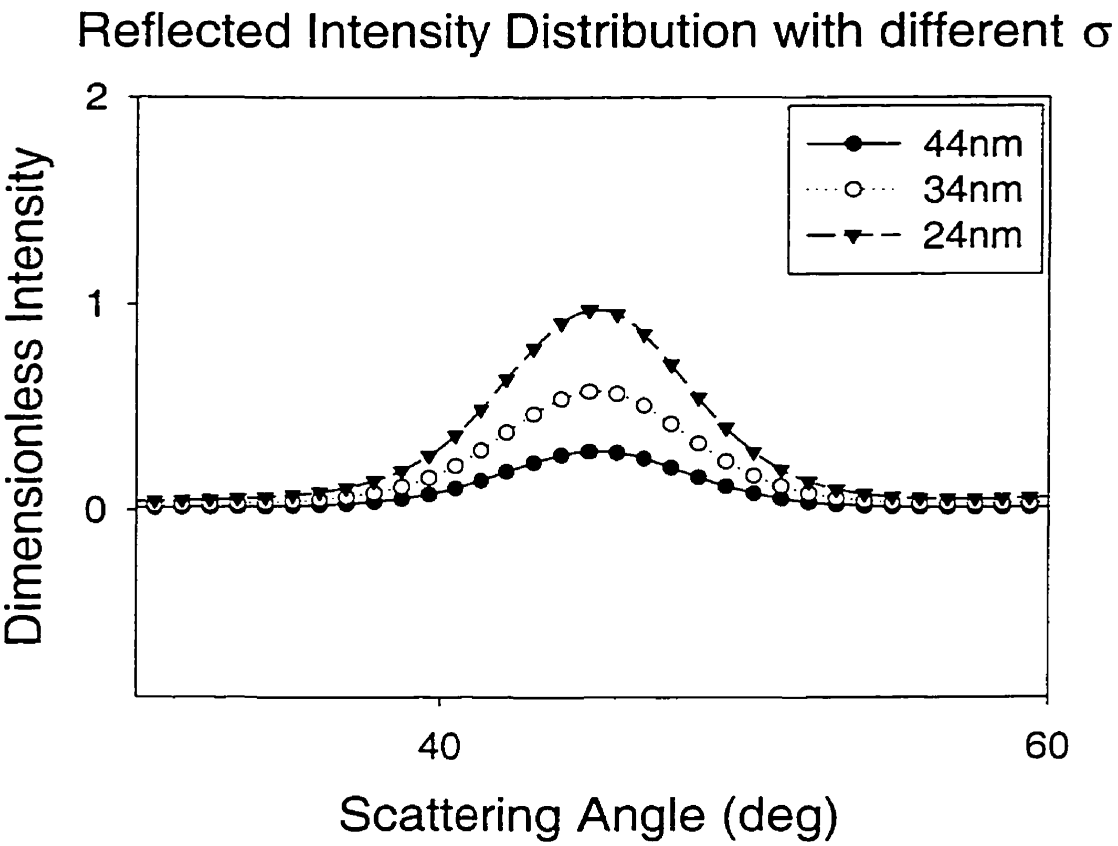

Figure 4-3: Reflected intensity distribution for an isotropically random surface with $\sigma = 24nm, 34nm, 44nm$ respectively. The incident angle is 45^o for all three cases.

For an isotropic rough surface, the reflected intensity distribution depends upon the standard deviation of the surface roughness and the lateral correlation length of the surface. The reflected intensity distribution for different values of surface height is presented in Figure 4-3, for three different σ values with the same incident angle and correlation length. Figure 4-3 shows that the specular intensity increase as the rms value σ of surface roughness decreases. This trend is expected because the coherent component, i.e. the specular reflection, would be dominant at a smaller σ value, whereas the incoherent component, i.e. the diffuse reflected intensity, should only take a smaller portion of the total reflected intensity. In physical reality, a decreasing σ represents a smoother surface. Consequently, the reflection tends to be more concentrated around the specular direction; this explains the increase in intensity and decrease in diffuse reflection.

4.3.2 Influence of Lateral Correlation Length and Incident Angle

Figure 4-4 shows that specular intensity rises with increasing lateral correlation length. This is because a longer lateral correlation length means a slower change in surface heights over the distance and fewer roughness humps within the reflection region. As a result, the specular reflection is enhanced. Reflection intensity for two different incident angles is shown in Figure 4-5. The specular direction in the intensity distribution shifts accordingly. It shows that specular reflection follows the classical optical theory, i.e. the reflected angle equals the incident angle.

4.3.3 Influence of Refractive Index of the Material

Figure 4-6 shows the specular gloss as a function of refractive index of the material at 20, 45 and 60 degrees, respectively. There is a monotonic increases in gloss with increasing refractive index. This is in accordance with the classical optical theory for perfectly smooth surfaces. According to the Fresnel equation [7], the higher the refractive index, the higher will be the reflected intensity in comparison to the transmitted intensity.

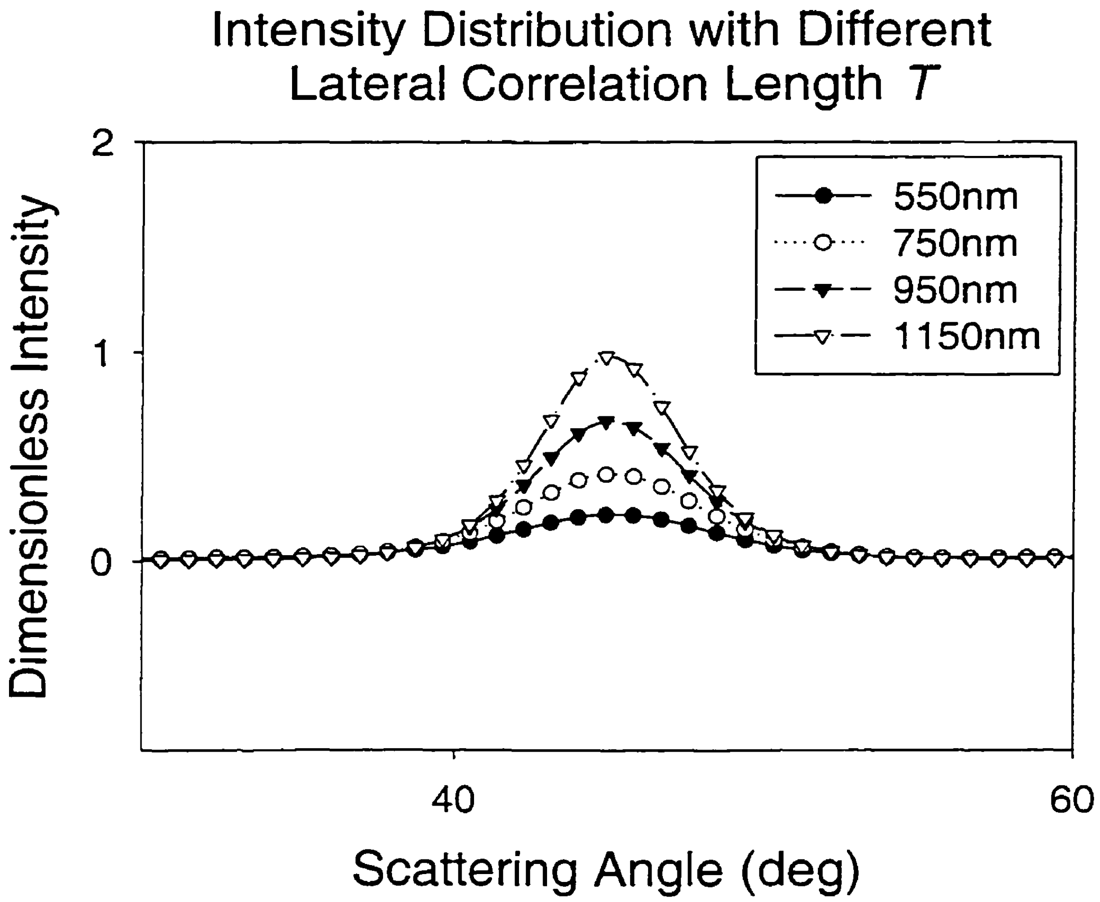

Figure 4-4: Reflected intensity distribution for an isotropically random surface with various lateral correlation lengths: $T = 550nm, 750nm, 950nm, 1150nm$. The incident angle is 45° for all cases.

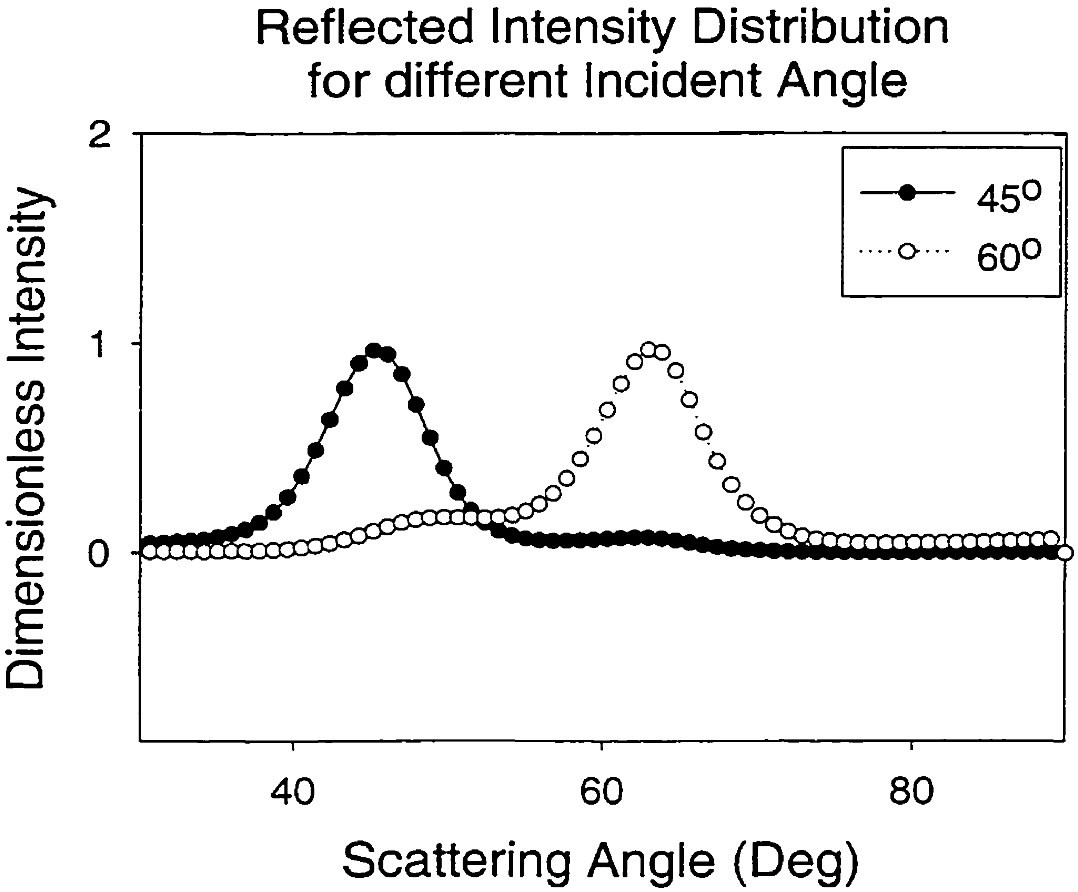

Figure 4-5: Reflected light intensity distribution with scattering angles, for incident angles of 45° and 60°; the maximum of reflected intensity is reached at angles 45° and 60°, respectively, indicating that specular reflection follows the classical optical theory.

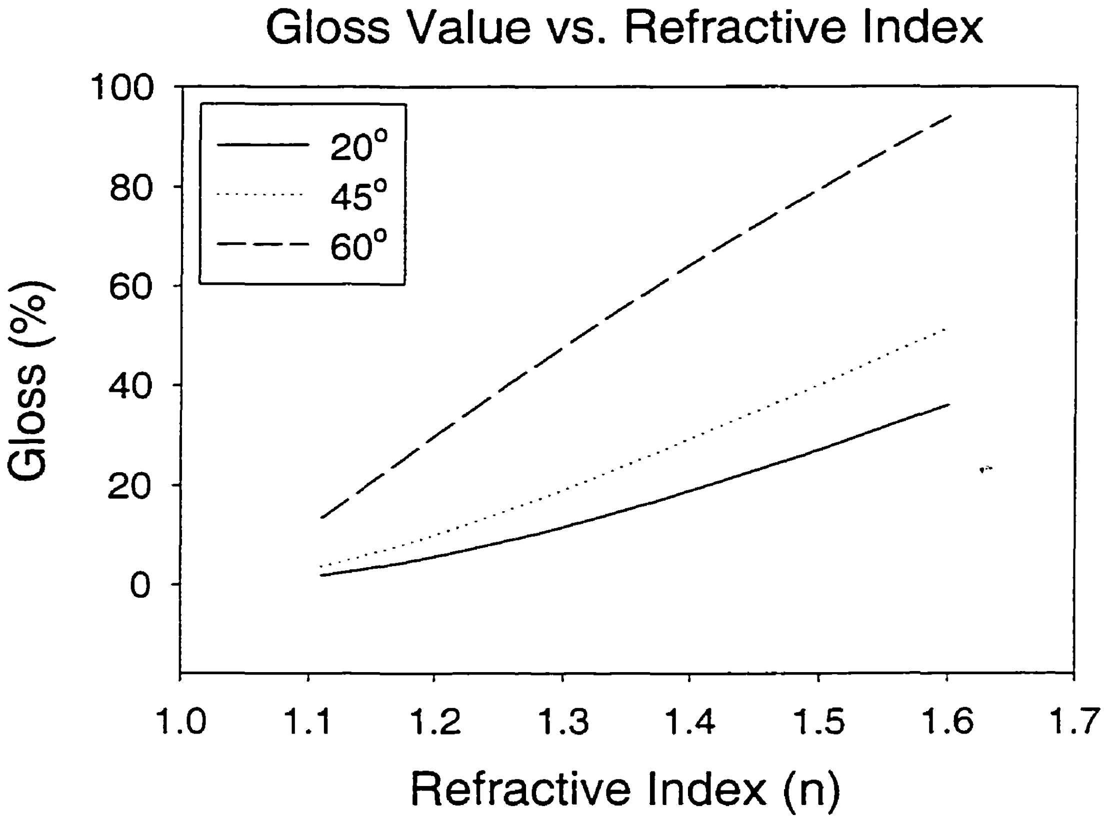

Figure 4-6: Gloss value as a function of refractive index of the material at three incident angles: $20^o, 45^o$ and 60^o.

Hence, the fraction of intensity reflected increases with the original incident intensity. The computation in Fig 4-6 assumes a fixed rough surface with a standard deviation of surface height of 49 nm. Figure 4-6 also shows that the difference in specular gloss at different angles are larger for higher refractive indices, the differences are small for smaller refractive indices. This is again the result of the weak reflection for materials with small refractive index. In addition, although all three curves exhibit monotonic increase with increasing refractive index, the slopes of the three curves are different.

4.3.4 Reflection and Gloss of Sample Films

A comparison of theoretical gloss values and the experimental measurements, for the various polyethylene films included in this study, is presented in Figure 4-7. There is good agreement between the theoretically computed gloss values and the experimental measurements. Because of the design of the glossmeter used in the experimental measurements, the measured gloss value may not consist of only the reflection from the film's top surface. It also includes the reflection of the surface of the background onto which the film is placed for measurement [39]. As a result, for highly transparent films, such an effect would be more significant and hence, a higher gloss value would be measured. In the theoretical assessment of gloss from the surface profile, this effect is not taken into consideration. This is the main reason behind the discrepancy in the observed difference between theoretical prediction and experimental measurements for high clarity film samples in Figure 4-7. For less transparent samples, the effect of background reflection is less significant, in which case better agreement between the theoretical values and the experimental measurements would be expected.

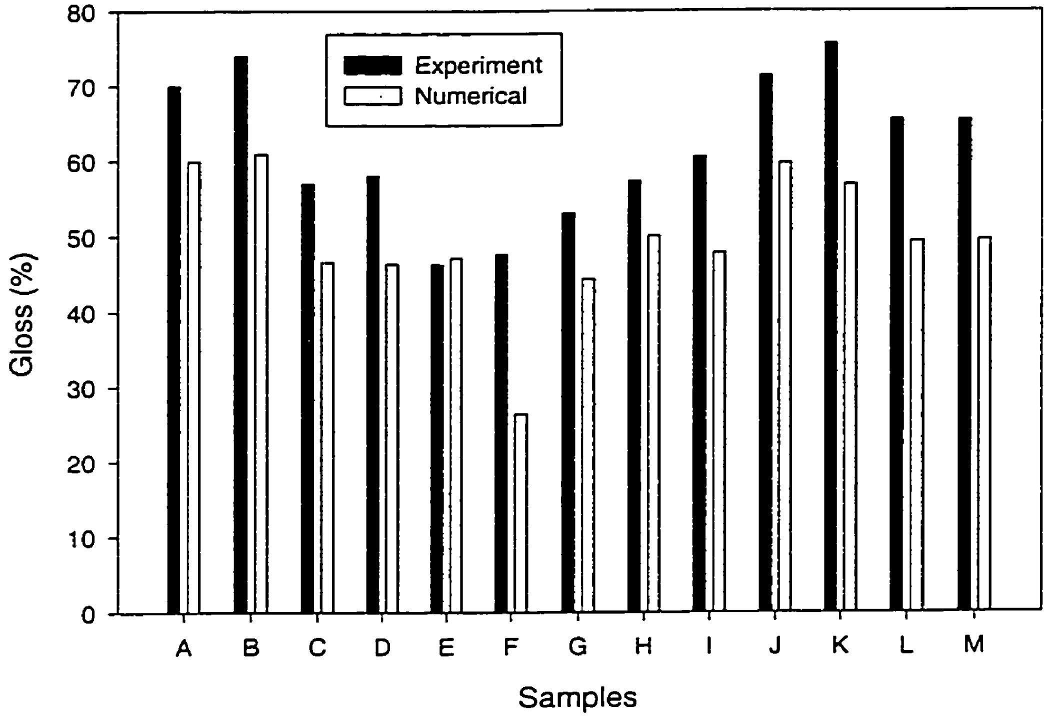

Figure 4-7: Comparison between experimental gloss values and values computed from the surface topography of sample films.

4.4 Summary

A model was developed to compute the reflection of light by the rough surface of polymer films based on the theory of the general Kirchhoff solution of the reflection of electromagnetic waves. The gloss of films was computed by combining this model with the results of the statistical characterization of the surface morphology of the films. The computed gloss values were in good agreement with the experimental measurements.

Chapter 5

Light Transmission and Haze

5.1 Introduction

Unlike gloss which is only a function of surface morphology, light transmission is dependent upon the surface as well as the bulk morphology. It is known that the reduction from perfect transparency for polyethylene blown films is mainly due to the scattering of light. As shown in Chapter 2, the resins or sample films in this project are weakly absorbing materials. The loss of light intensity when passing through the material is thus negligible.

5.1.1 Relationship between Transmittance and Microstructure

A range of approximation theories has been employed in the study of light scattering by polymeric materials. Among them, the Rayleigh approximation assumes that the size of the scattering particles is much smaller than the wavelength of incident light and that the difference between the refractive index of the scattering particle and the surrounding medium is very small[40]. Because of its restrictions, its application in studying light scattering by solid polymers is limited. A more generalized approach, based on the

Rayleigh approximation, is the Rayleigh-Gans-Debye approximation theory, which still requires that the refractive index mismatch is very small, but it is not limited to small particles[40]. The Anomalous Diffraction approximation, on the other hand, requires that the size of the scattering entities is very large compared to that of the incident wavelength and that the refractive index mismatch with the surrounding medium is very small[41].

The Rayleigh-Gans-Debye approximation was the principle theory used in the treatment by Stein and co-workers of light scattering by spherulites in semicrystalline polymers. Individual polymer crystals are very thin (typically $\sim 10nm$) lamellae, which alternate with lower-density layers of amorphous polymers of similar size. Large numbers of crystallites grow radially outwards from a common nucleus to form a spherically shaped spherulite superstructure. The introduction of theoretical treatment of light scattering by spherulites was made by Stein and Rhodes [42]. It is shown that the sphere, as a result of the regular orientation of the anisotropic crystallites, can be characterized by differing radial and tangential refractive indices. In addition, Stein and Prud'homme [43] pointed out that the light scattering properties of spherulites, and hence the transparency of semicrystalline polymers, are not dominated by the fine scale refractive index fluctuation as a result of the alternating crystalline amorphous phase layers inside a spherulite. It was determined by the optical properties of the larger spherulitic superstructures. Following this approach, further studies were carried out for the low-angle light scattering pattern of anisotropic two-dimensional spherulitic disks [44], the light scattering of orientationally disordered spherulites [45] [46], and light scattering patterns of different crystalline orientations [47]. Based on the theories for light scattering by two-dimensional spherulites, Prud'homme [48] studied the multiple scattering of a layered structure. It was found that multiple scattering tends to make the scattering envelope more diffuse, reducing the intensity in the high intensity region, while increasing the intensity in the low intensity region. In addition to light scattering by perfect spherulitic discs, the theory of small-angle light scattering was developed for oblique incidence of the light beam on the surface of a two-dimensional spherulite [49] and scattering of light by disordered spherulites [50]. For small-angle light scattering by random assemblies of truncated spherulites [51], the effect of truncations on the scattering patterns for two-dimensional spherulites is explored as a function of the size, number, and location of the truncations. There were also reported works describing the scattering of arrays of spherulites [52] [53].

A different approach using the Anomalous Diffraction approximation theory has been applied to the study of light scattering by latex solutions [41]. These studies have been very successful inside their domain of validity. In particular, the light scattering approximation theories have been applied to the study of polymer morphology from small angle light scattering (SALS) patterns. However, because of the restriction on the refractive index mismatch between the scattering entities and the surrounding medium, the applications of these approximation theories are limited.

In addition to approximation theories, the Mie scattering theory [40] provides an analytical solution to Maxwell's equations for light scattering by a single homogeneous sphere, regardless of its refractive index and size. For immiscible polymer blends where one component provides only a small volume fraction, or for samples containing a low level of voids or additives, a different approach becomes appropriate, in which the sparsely distributed second phase is regarded as an assembly of separate scattering particles. Provided that these are positioned randomly, the overall scattered-light intensity distribution may be calculated simply by adding the intensity contributions from individual particles. Based upon a geometry in which the scattering particles are sparsely distributed in a uniform surrounding medium, a model based on the Mie scattering theory was proposed by Willmouth [54]. It assumes a random distribution of scatterers of the same size in the medium and neglects multiple scattering effects. The volume fraction of scattering particles in the bulk is limited to $\sim 10^{-4}$, in order for the assumption of neglecting multiscattering to be valid. This requirement implies that the scattering particles in the surrounding medium have to be either very small or very few. For polyethylene blown films, in which the spherulites are abundant, this model cannot be employed.

Other works on light transmission and scattering by thin films are mostly concerned with Polymer-dispersed Liquid Crystal PDLC thin films. PDLC films consist of liquid crystal (LC) microdroplets dispersed in polymer matrices [55]. They can be switched electrically from a cloudy, light scattering state ("off state") to a transparent state ("on state"). The parameters of interest here are the refractive index of the LC droplets as well as the surrounding polymer medium, the volume fraction, the size and distribution of the LC droplets. The radius of these droplets is $0.1\mu\text{m} \sim 10\mu\text{m}$, and the volume fraction they occupy is $10\% \sim 50\%$. Theoretical treatment of light scattering by nematic droplets was based on the Rayleigh-Gans-Debye approximation [56][57]. The results were used in the study of light scattering by PDLC films [58], assuming that the droplets form a collection of optically isotropic scatterers with negligible multiple scattering. Another mathematical model has been proposed to describe the optical behavior of the material in the framework of the Anomalous Diffraction theory [59]. An attempt at the theoretical solution to the multiple scattering problem is reported using the homogenization approach [60]. As pointed out in [58], an exact analysis of light scattering by PDLC films is not possible, because no theory of multiple scattering is available.

The present work relates to the optical properties of commercially produced polyethylene (PE) blown films. In the industrial film blowing process, melted polymer is extruded from an annular die gap and is then blown to a tube much larger than the die while being stretched longitudiually and cooled by cold air emitted from an air ring outside the die gap. The basic physical processes governing the transparency of blown polyethylene films were first studied by Clegg and Huck [61] [62]. For thin blown films, they demonstrated that nearly all of the light scattering was caused by light scattered at the surface rather than the bulk. Clegg and Huck showed that film haze increases with melt elasticity. Two dissimilar scales of melt flow surface defect were identified, the finer leading to film haze and the coarser to imperfect clarity, and these were tentatively ascribed to different aspects of the extrusion process. Secondly, Clegg and Huck showed that surface roughness is also caused by the growth of spherulites close to the film surface. This process becomes more important for crystalline polymers such as polyethylene. From their conclusion, a multistage cooling mechanism was proposed to improve transparency in which the reduction in haze is solely attributed to changes in crystalline morphology. Fritz and Rothe [63] carried out a more detailed analysis and emphasized the inverse relation between haze and gloss for films where surface scatter is dominant. Hert and co-workers [64] have studied films made from low-density polyethylene manufactured using Ziegler-Natta catalyst. Again it was found that the majority of scattered light originates from the surface roughness, and, in this case, the dominating cause for such roughness is crystallization on and beneath the surface.

Other works on the transparency of polymers are mostly concerned with polyethylene terephthalate. Giuffria [65] identified both surface and internal scattering as contributions to haze. Ouchi and co-workers [66][67] studied how the contributions to haze from both the surface and interior of the films varied with draw ratio and with the state of polarization of the incident light. Hobbs and Pratt [68] have studied the origins of haze in biaxially oriented polypropylene films. It was shown that the main cause for haze is a microfibrillar surface texture, the extent of which is attributed to the spherulitic morphology of the polymer. For thick polymer films, Su [69] studied the increased haze of compression moulded high-nitride plastics resulting from water uptake after immersion at selected temperatures. Jabrain [70] investigated the appearance of an initially amorphous extruded PET sheet that had been crystallized at various temperatures. Haze was determined as a function of percentage crystallinity, spherulite size and volume fraction; irrespective of crystallinity, it showed a maximum for spherulite radii of $\sim 1.7\mu$m and spherulite volume fractions of ~ 0.6. Khan and Keener [71] studied the spatial and optical properties of particle-doped PET film. It was found that haze and surface roughness follow the same trend during the biaxial drawing process, suggesting a correlation between the two.

Recently, Atomic Force Microscopy (AFM) was used in studying the surface morphology as well as its relation to transmission haze for polyethylene blown thin films [72]. Smith and co-workers measured the haze of PE blown films with and without oil immersion [25]. The results showed that haze is mainly the derivative of the surface, whereas the bulk contributes less ($\sim 20\%$) to the total haze. A qualitative correlation was found between the surface roughness and transmission haze. Olley and Basset [73] studied the effects of surface morphology on haze for drawn polypropylene films. By comparing a smooth surface produced by fast cooling with that of a rough spherulitic surface, they found that the surface morphology has a significant impact on the structure and number of haze rings of the product. It is clear from the above experimental studies that surface morphology is an important factor in the haze of blown thin films.

All of the theoretical studies of light scattering by polymer films summarized above assume smooth incident and exit surfaces and that the scattering of light is from the bulk. Little is known about the mechanism of surface scattering. In fact, there does not appear to be a theoretical treatment of the relationship between surface morphology, forward scattering and haze of blown films. Moreover, there are no quantitative correlations between experimental haze data and quantitative measurements of forward scattering and surface roughness. The present work attempts to address these issues.

5.1.2 Measuring Forward Transmittance and Haze

In industrial practice, the measurement of haze is specified in material testing standards [74]. Haze is defined as the percentage of transmitted light which, in passing through a specimen, deviates from the incident beam by more than 2.5° from the normal incident beam. In the study of light transmission and forward scattering by polymer films, the parameters of interest are direct transmittance, total transmittance and haze, as shown in Figure 5-1. Here I_0 is the incident flux, I_t is the direct transmitted flux, $(I_s)_f$ is the forward scattered flux, i.e. the scattered intensity between 0° and 90°. $(I_s)^{90}_{2.5}$ is the scattered flux that is deviated from the incident beam in between 2.5° and 90°. The forward transmission parameters are defined as follows,

$$\begin{aligned}
&\text{Direct Transmittance} = \frac{I_t}{I_o} \\
&\text{Total Transmittance} = \frac{I_t + (I_s)_f}{I_o} \\
&\text{Haze} = \frac{(I_s)^{90}_{2\frac{1}{2}}}{I_t + (I_s)_f}
\end{aligned} \tag{5.1}$$

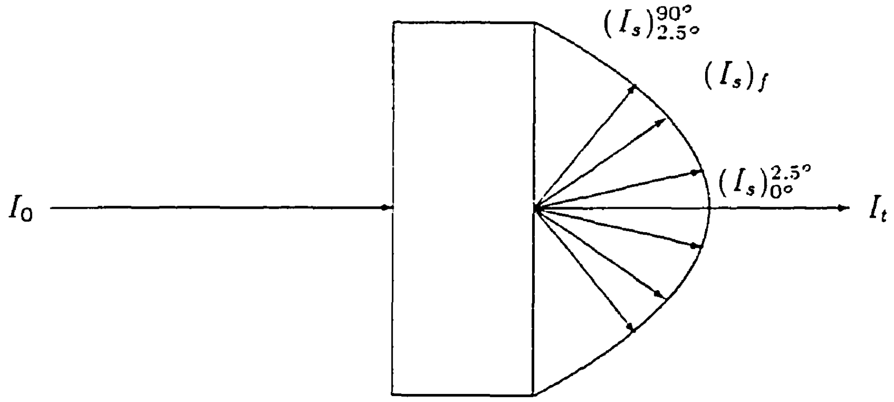

Figure 5-1: Schematic of light transmission through a polymer film sample

Haze is defined as the cloudy or turbid aspect or appearance of an otherwise transparent specimen caused by light scattered from within the specimen or from its surfaces. In the specified test method, haze is the percent of total transmitted light which, in passing through the specimen, deviates from the incident beam through forward scatter by more than 0.044rad or 2.5°. The standard procedure of measuring the forward transmittance and haze requires the use of a hazemeter. The schematic of this hazemeter is shown in Figure 5-2 [74]. The light source is an incandescent lamp. A nominally parallel 1-2cm diameter beam strikes the specimen, which is placed against the entrance port of an integrating sphere whose inside surface is painted uniformly matt white. Light is diffused by multiple back-scattering from the white walls. The photocell, which is prevented by baffles from receiving any light directly from the entrance port, detects an intensity that is proportional to the total radiant flux entering the sphere.

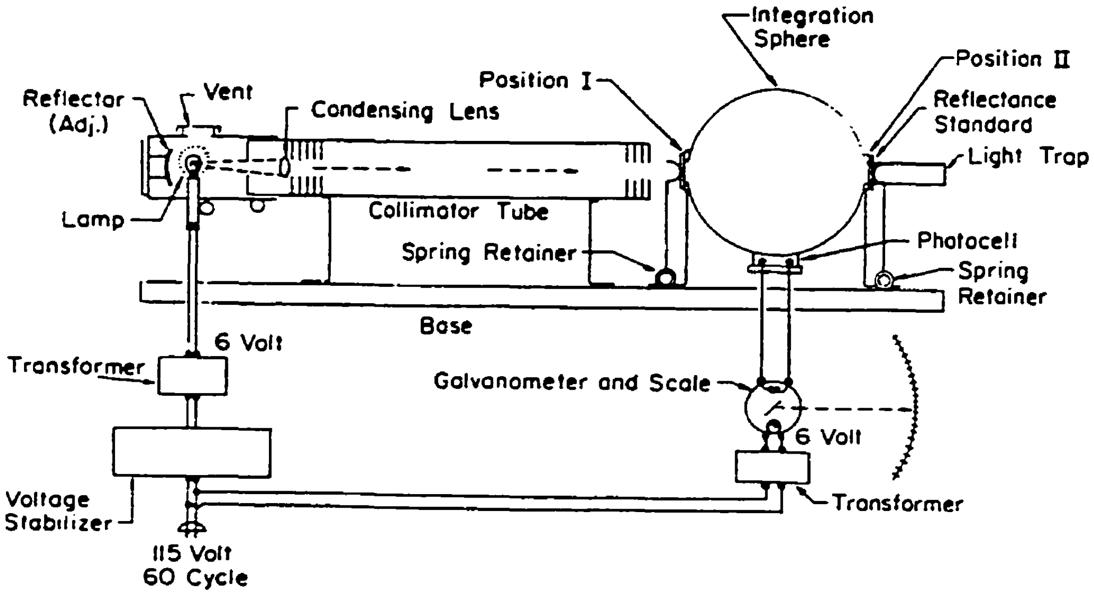

Figure 5-2: Schematic of Commercial Hazemeter

The test is conducted by taking four different consecutive readings and measuring the photocell output as follows:

T_1 = Specimen and light trap out of position, reflectance standard in position
T_2 = Specimen and reflectance standard in position, light trap out of position
T_3 = Light trap in position, specimen and reflectance standard out of position
T_4 = Specimen and light trap in position, reflectance standard out of position

The quantities represented in each reading are incident light, total light transmitted by specimen, light scattered by instrument, and light scattered by instrument and specimen, respectively. Total transmittance T_t and diffuse transmittance T_d are calculated as follows:

$$\begin{aligned} T_t &= \frac{T_2}{T_1} \\ T_d &= \frac{T_4 - T_3(T_2)}{T_1} \end{aligned} \tag{5.2}$$

Percentage haze is calculated as follows:

$$\text{Haze (percent)} = \frac{T_d}{T_t} \times 100 \tag{5.3}$$

5.2 Theory of Light Scattering

5.2.1 Mie Theory of Light Scattering

Assume a single homogeneous sphere of radius a in a vacuum. Using Debye potentials π_1 and π_2 [7], a plane wave incident light, having a unit amplitude, is expanded in spherical coordinates:

$$r\pi_1^i = \frac{1}{k^2}\sum_{n=1}^{\infty} i^{n-1}\frac{2n+1}{n(n+1)}\psi_n(kr)P_n^{(1)}(\cos\theta)\cos\phi \tag{5.4}$$

$$r\pi_2^i = \frac{1}{k^2}\sum_{n=1}^{\infty} i^{n-1}\frac{2n+1}{n(n+1)}\psi_n(kr)P_n^{(1)}(\cos\theta)\sin\phi \tag{5.5}$$

where k is the propagation constant, and $k = 2\pi m/\lambda_0$; m is the refractive index of the sphere; λ_0 is the wavelength of incident light in free space; $P_n^{(1)}(\cos\theta)$ is the associated Legendre polynomials of degree 1 and order n; ψ_n is the Ricatti-Bessel function of the order n.

By introducing the Debye potential to the Maxwell's equations, the original vector form equations are reduced to two scalar wave propagation equations. Assuming the scattering particle is not magnetic, solving the scalar wave equations in spherical coordinates gives the expression for a scattered wave [7]:

$$r\pi_1^s = -\frac{1}{k^2}\sum_{n=1}^{\infty} i^{n-1}\frac{2n+1}{n(n+1)}a_n\zeta_n(kr)P_n^{(1)}(\cos\theta)\cos\phi \tag{5.6}$$

$$r\pi_2^s = -\frac{1}{k^2}\sum_{n=1}^{\infty} i^{n-1}\frac{2n+1}{n(n+1)}b_n\zeta_n(kr)P_n^{(1)}(\cos\theta)\sin\phi \tag{5.7}$$

where ζ_n is Hankel functions of the order n, and a_n and b_n are the Mie coefficients. They are obtained by satisfying the boundary conditions at the sphere-air interface. At $r = a$, the tangential components of the electric field E and magnetic field H must be continuous across the interface. By matching the derivatives of Debye potentials with respect to r at the interface of the sphere and the surrounding air, the coefficients a_n and b_n are obtained in the form of Ricatti-Bessel functions and Hankel functions [7].

$$a_n = \frac{\psi_n(\alpha)\psi_n'(\beta) - m\psi_n(\beta)\psi_n'(\alpha)}{\zeta_n(\alpha)\psi_n'(\beta) - m\psi_n(\beta)\zeta_n'(\alpha)} \tag{5.8}$$

$$b_n = \frac{m\psi_n(\alpha)\psi'_n(\beta) - \psi_n(\beta)\psi'_n(\alpha)}{m\zeta_n(\alpha)\psi'_n(\beta) - \psi_n(\beta)\zeta'_n(\alpha)} \tag{5.9}$$

where, α and β are:

$$\alpha = \frac{2\pi a}{\lambda_0} \tag{5.10}$$

$$\beta = m\alpha \tag{5.11}$$

α is also called the size parameter. The Ricatti-Bessel functions ψ, χ and Hankel functions ζ are derived from half integral order Bessel and Neumann functions:

$$\psi_n(z) = (\pi z/2)^{1/2} J_{n+\frac{1}{2}}(z) \tag{5.12}$$

$$\chi_n(z) = -(\pi z/2)^{1/2} N_{n+\frac{1}{2}}(z) \tag{5.13}$$

$$\zeta_n(z) = \psi_n(z) + i\chi_n(z) \tag{5.14}$$

The physical meaning of Mie coefficients a_n and b_n can be explained by multipole expansions. Any distribution of electric and magnetic dipoles may be represented by a superposition of electric and magnetic multipoles located at some origin with arbitrary multipole movements. In the case of light scattering, the distribution of charges and currents is oscillating at the same frequency as the incident wave and the scattered radiation arises from these multipole movements. Consider the Debye potential corresponding to the partial waves, π^s_{1n} and π^2_{2n}, defined by:

$$r\pi^s_1 = \sum_{n=1}^{\infty} r\pi^s_{1n} \tag{5.15}$$

$$r\pi^s_2 = \sum_{n=1}^{\infty} r\pi^s_{2n} \tag{5.16}$$

Then π^s_{11} describes the radiation by an oscillating electric dipole whose moment is proportional to the scattering coefficient a_1. π^s_{21} is the Debye potential representing the radiation by an oscillating magnetic dipole whose moment is proportional to the scattering coefficient b_1. The higher terms a_n and b_n in equation (5.8) and (5.9) are multipole moments and they are related to each term in the expansion of the Debye potentials in equation (5.15) and (5.16) . This gives the Mie coefficients a clear physical meaning. The scattered radiation is a superposition of multipole radiations, each weighted by its appropriate multipole moment. The frequency of the oscillations is equal to the exciting frequency, i.e. the frequency of the incident light, and the partial fields corresponding to each mode mutually interfere to produce the total scattering field. Each scattering coefficient determines the magnitude of the wavelet associated with each particular multipole.

When a_n and b_n are known, the intensity distribution of the scattering field can be calculated from the above equations. At the far field zone of the scattering field, when $kr \gg n$, here n is the order of the Ricatti-Bessel function, the Mie amplitude functions S_1 and S_2 are defined by,

$$S_1(\theta) = \sum_{n=1}^{\infty} \frac{2n+1}{n(n+1)}[a_n \pi_n(\cos\theta) + b_n \tau_n(\cos\theta)] \tag{5.17}$$

$$S_2(\theta) = \sum_{n=1}^{\infty} \frac{2n+1}{n(n+1)}[a_n \tau_n(\cos\theta) + b_n \pi_n(\cos\theta)] \tag{5.18}$$

with

$$\pi_n(\cos\theta) = \frac{P_n^{(1)}(\cos\theta)}{\sin\theta} \tag{5.19}$$

$$\tau_n(\cos\theta) = \frac{d}{d\theta}[P_n^{(1)}(\cos\theta)] \tag{5.20}$$

The field vectors $(E_\phi, E_\theta, H_\phi, H_\theta)$ are given by:

$$\begin{aligned} E_\phi &= H_\theta = -\frac{i\exp(-ikr)}{kr}\sin\phi\sum_{n=1}^{\infty}\frac{2n+1}{n(n+1)}S_1 && (5.21) \\ E_\theta &= -H_\phi = \frac{i\exp(-ikr)}{kr}\cos\phi\sum_{n=1}^{\infty}\frac{2n+1}{n(n+1)}S_2 && (5.22) \end{aligned}$$

Using Poynting's theorem, the energy flow in the scattered wave is given by:

$$S = \frac{1}{2}(E_\theta H_\phi^* - E_\phi H_\theta^*) \qquad (5.23)$$

where the asterisk denotes the complex conjugate. The intensity of scattered light in the θ and ϕ azimuths is:

$$\begin{aligned} I_\phi &= \frac{\lambda^2}{4\pi^2 r^2}|S_1|^2\sin^2\phi && (5.24) \\ I_\theta &= \frac{\lambda^2}{4\pi^2 r^2}|S_2|^2\cos^2\theta && (5.25) \end{aligned}$$

These two components are perpendicular and parallel, respectively, to the scattering plane, which contains the incident direction and the direction of the scattered wave (θ, ϕ).

Each of these components of the scattered light can be thought of as arising from the component of the incident beam polarized in the same sense, i.e. I_ϕ originates from the incident beam of intensity $\sin^2\phi$ polarized perpendicularly to the scattering plane, and I_θ from a beam of intensity $\cos^2\theta$ polarized parallel to the scattering plane.

For unpolarized incident light of unit intensity, the scattered intensity from a single homogeneous sphere measured at distance r from the center of the sphere is given by:

$$I = \frac{\lambda^2}{8\pi^2 r^2}(|S_1(\theta)|^2 + |S_2(\theta)|^2) \qquad (5.26)$$

Scattering cross section C, defined as the total energy scattered by a particle in all directions, can be obtained by integration of (5.26) over the surface of a sphere:

$$\begin{aligned} C &= \int_0^{\pi}\int_0^{2\pi} I r^2 \sin\phi d\phi d\theta \\ &= (\frac{\lambda^2}{2\pi})\sum_{n=1}^{\infty}(2n+1)(|a_n|^2+|b_n|^2) \end{aligned} \tag{5.27}$$

Scattering efficiency factor Q is obtained from the cross section by dividing by the actual geometrical cross section, which is πa^2 for a sphere:

$$\begin{aligned} Q &= \frac{C}{\pi a^2} \\ &= \frac{\lambda^2}{2\pi^2 a^2}\sum_{n=1}^{\infty}(2n+1)(|a_n|^2+|b_n|^2) \end{aligned} \tag{5.28}$$

Exact evaluation of the scattering problem requires the sum of the infinite series. It is, of course, physically impossible to compute all of the terms. For a converging series, however, when a sufficient number of terms are summed, the results can be arbitrarily close to the exact sum. It is known that for any converging series s_n and any given small number ϵ, there exists a number N such that $\epsilon > \sum_{n>N} s_n$. In practice, when the individual term of the series reaches below the preset precision ($s_N < 10^{-10}$) the remaining terms of the series are considered to be insignificant and the computation is stopped. The partial sum of the series is taken as the sum of the entire series.

The scattering cross section is related to the transmission of a beam through multiple scatterers. The attenuation due to scattering is [40]:

$$-\frac{dI}{dx} = \tau I \tag{5.29}$$

The transmission is:

$$\frac{I_t}{I_0} = \exp(-\tau l) \tag{5.30}$$

where I_0 is the incident intensity. I_t is the intensity at distance l, and τ is the attenuation coefficient, or turbidity. Here it is assumed that there is no absorption by the polymer material when light is passing through the medium. Multiple scattering particles can be considered individually for their contribution to the total scattering field. For N particles of the same size in unit volume, the turbidity is given by:

$$\tau = NC = \frac{N\lambda^2}{2\pi}\sum_{n=1}^{\infty}(2n+1)(|a_n|^2 + |b_n|^2) \tag{5.31}$$

where C is the scattering cross section of the particles. This assumption is valid when the effect of multiple scattering is small and can be neglected. When the volume fraction of scattering particles increases, incident light will likely be scattered more than once by different scattering particles in its path. This multiple scattering effect has two significant impacts on the transparency of the material. Firstly, the direct transmitted light flux will be greatly reduced when the scattering is strong. Secondly, the length of the path on which the light travels within the material increases significantly with multiple scattering. As a result, the absorption of light flux by the medium increases. The combined effect of these two aspects leads to diminishing direct transmittance and weak total transmittance. The transparency of the material will diminish to translucency, and eventually to opaqcity.

5.2.2 Surface Scattering of Polyethylene Blown Films

A general schematic of the film cross section morphology is shown in Figure 5-3. The polyethylene blown film is considered to consist of three layers: the entry surface, the exit surface and the interior. The cross-section can be considered symmetrical with respect to the x axis. Surface layers are defined as the roughness between z_{max} and z_{min}. The bulk, or the interior layer is from z_{min} to $-z_{min}$. The roughness on the surface consists of spherulites formed on and beneath the surface during the blowing process. Since the

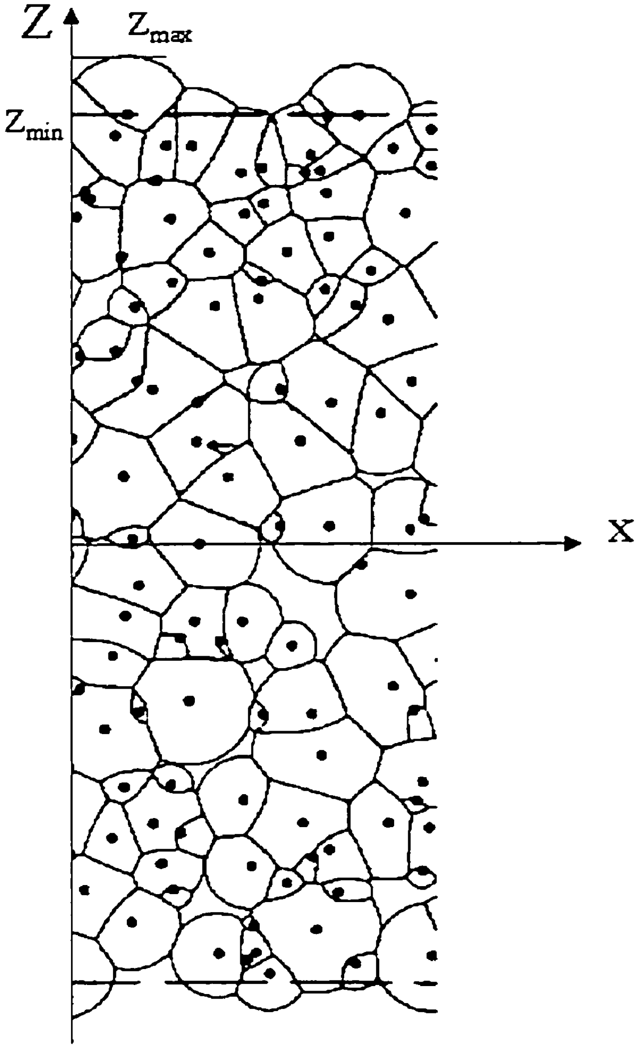

Figure 5-3: Schematic of polymer film

scattering of light is entirely a result of the superstructure of spherulites rather than the refractive index fluctuation caused by the crystallite-amorphous alternating layered structure inside a spherulite [52], spherulites on the surfaces and in the bulk are treated as isotropic and homogeneous scattering entities. Note that in Figure 5-3, the surface layers contain only segments of the spherulites, i.e. the upper part of the surface of spherulites constitutes the surface profile and the lower part is buried in the interior and in contact with impinged spherulites in the bulk.

As shown in Figure 3-19, the bulk of the sample film is formed by a very high volume fraction of spherulite. Since scattering is mainly caused by the refractive index mismatch between scattering entities and the surrounding medium and in this case the interior of the film is filled with spherulites of the same refractive index, the light scattering originated from the bulk is neglected. Therefore, the main contribution to light scattering is due to the surface. In the absence of light absorption, since the film is very thin, the Debye potentials can be considered constant within the film interior. It is then possible to neglect the interior and consider the spherulites on the incident surface as a layer of partial spherulites. Similarly, the exit surface is considered also as a layer of partial spherulites. The boundary conditions that the tangential component of E and H vectors are continuous through the interface are satisfied at the two surfaces. Since the scatterers are formed into one single layer, the effect of multiple scattering is not a factor in evaluating the forward transmission field. Each spherulite will contribute independently to the final scattering field. Since the refractive index mismatch between spherulites on the film surface and the surrounding air is large, the Rayleigh-Debye approximation theory and Anomalous Diffraction approximation theory are not applicable in this case. Because it has no restrictions as to the refractive index mismatch and particle size, the Mie theory of light scattering is applicable.

For a polydispersed system, in which scatterers contribute independently to the total result, the turbidity is given by [40]:

$$\tau = \int_0^\infty C(a)p(a)da \tag{5.32}$$

where $p(a)$ is the probability distribution function of scatterers of the diameter a. $C(a)$ is the scattering cross-section. For sample films, the spherulites on the surface are randomly distributed and of different sizes. a and $p(a)$ are represented by the domain size distribution profile which is derived from AFM images of film surface. Note here that the term volume fraction denotes the ratio of the volume of spherulites in the surface layer to that of the surface layer itself. It is different from the volume of spherulites in the unit volume as used in previous studies [54].

Partial scattering cross section is defined as the total light flux scattered by a single scattering particle between two angles θ_1 and θ_2. For an unpolarized incident flux of unit intensity it is determined by integrating equation (5.26) over the appropriate angles:

$$(C)_{\theta_1}^{\theta_2} = \frac{\lambda^2}{4\pi} \int_{\theta_1}^{\theta_2} (|S_1(\theta)|^2 + |S_2(\theta)|^2) \sin\theta d\theta \tag{5.33}$$

Assuming the thickness of the surface spherulites layer is t, the direct transmitted intensity is given by:

$$I_t = I_0 \exp(-\tau t) \tag{5.34}$$

Therefore, in the absence of absorption, the total scattered intensity in all directions is:

$$I_s = I_0 - I_t = I_0[1 - \exp(-\tau t)] \tag{5.35}$$

Since the scattering cross section represents the total energy scattered, we must have for any two angles θ_1 and θ_2:

$$\frac{(I_s)_{\theta_1}^{\theta_2}}{I_s} = \frac{(C)_{\theta_1}^{\theta_2}}{C} \tag{5.36}$$

which leads to the partial scattered intensity:

$$(I_s)_{\theta_1}^{\theta_2} = \frac{(C)_{\theta_1}^{\theta_2}}{C} I_0[1 - \exp(-\tau t)] \tag{5.37}$$

From partial scattering intensity distribution, the forward transmission parameters can be computed from equation (5.1). Assume the incident intensity is unit, direct transmittance is given by:

$$\begin{aligned} \mathrm{DT} &= \frac{I_t}{I_0} \\ &= \exp(-\tau t) \end{aligned} \tag{5.38}$$

the total transmittance is:

$$\begin{aligned} \mathrm{TT} &= \frac{I_t + (I_s)_0^{90}}{I_0} \\ &= \exp(-\tau t) + \frac{(C)_0^{90}}{C}[1 - \exp(\tau t)] \end{aligned} \tag{5.39}$$

and haze of the film is:

$$\begin{aligned} \mathrm{Haze} &= \frac{(I_s)_{2.5}^{90}}{I_t + (I_s)_0^{90}} \\ &= \frac{(C)_{2.5}^{90}[1 - \exp(-\tau t)]}{C\exp(-\tau t) + (C)_0^{90}[1 - \exp(-\tau t)]} \end{aligned} \tag{5.40}$$

5.3 Results and Discussion

5.3.1 Effect of Volume Fraction of Scatterers

The scattering intensity distributions for different values of volume fraction of scatterers are plotted in Figure 5-4, with a fixed size of the scatterers of 0.49μm. The refractive index of the polymer is assumed to be 1.55. The free-space wavelength in this computation is assumed to be 0.55μm. Note here that the term volume fraction denotes the ratio of the volume of spherulites in the surface layer to that of the surface layer itself. It is different from the volume of spherulites per unit volume as considered in other studies [54]. The scattering intensity at angles larger than 2.5° are plotted. Since the incident light is unpolarized white light, the scattering field is axial symmetric and the distribution is one dimensional. The scattered intensity increases as the volume fraction of the scattering spherulites on the surface increases. The rate of increase will slow down when the volume fraction is already high. Note here that the direct transmitted light flux at 0° is not included in the plot, because the intensity of the direct transmitted beam is much larger than that of the scattered ones, and, if included, it would make the variance in the scattered intensity distribution much less visible.

Figure 5-5 shows the transparency parameters with respect to different volume fractions of scatterers. The diameter of scatterers is assumed to be 0.15μm, and the refractive index is 1.55. These parameters are computed using Equation (5.1), once the angular intensity distribution of the scattering field is established. Notice that the total transmittance and direct transmittance are, respectively, the percentages of all transmitted light flux and the light flux that stays in the direction of incident light with respect to the incident light intensity, which is assumed to be unit. Haze is the percentage of light intensity scattered between 2.5° and 90°, with respect to all of the transmitted light intensity, instead of the incident light. This definition excludes the influence of extinction and backscattering on haze and is in accordance with the testing standard being used to measure the haze and transmittance [74]. As seen in Figure 5-5, haze increases with increasing volume fraction. The direct indication is that as the number of the scattering spherulites increases, more light flux will be scattered away from the direction of incident light. Total transmittance decreases and this decrease is attributed to the

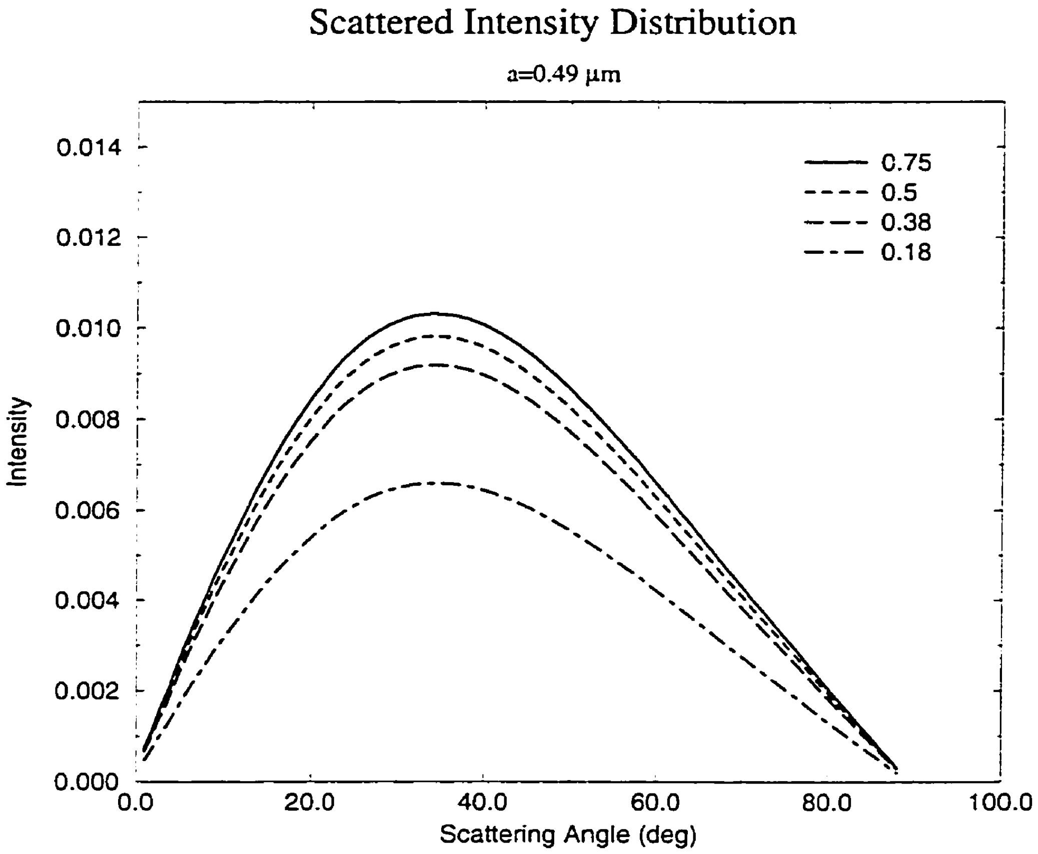

Figure 5-4: Scattering intensity distribution for different volume fractions of scattering particles, assuming scattering particles have the same diameter of $0.49\mu m$

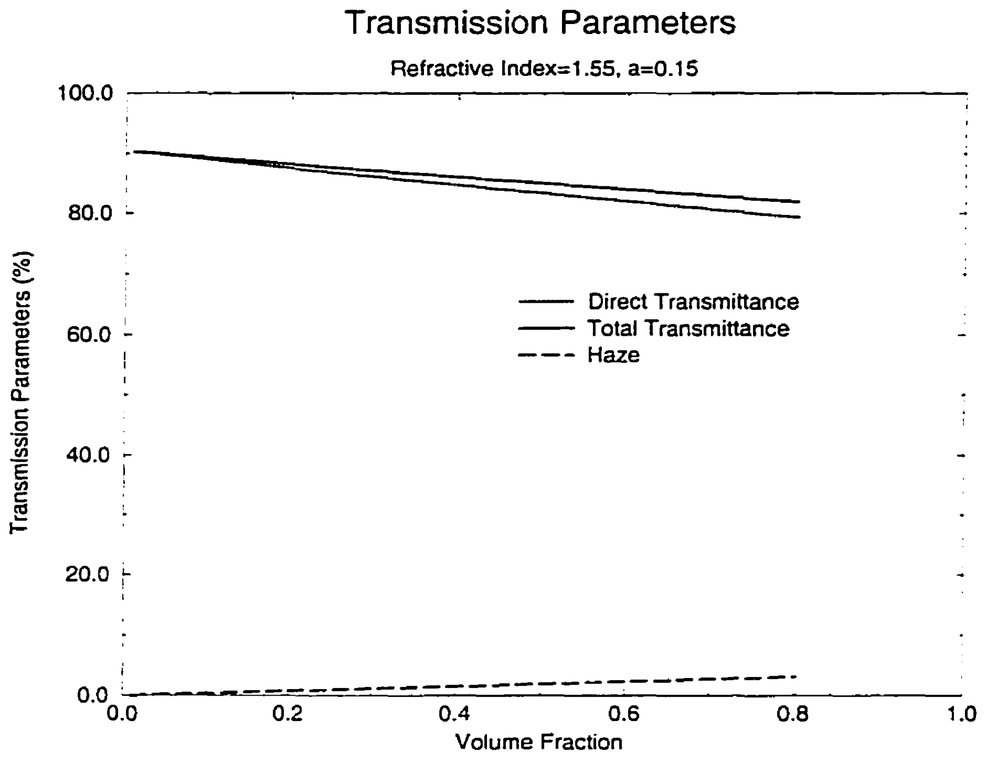

Figure 5-5: Transmission parameters as functions of volume fraction of scattering particles

increasing effect of backscattering with the increasing amount of scatterers. As shown in Equation (5.1), total transmittance includes only the forward scattered intensity plus the direct transmitted intensity. The scattering cross-section C represents the scattering intensity in all directions. Therefore, when C increases, the light flux scattered between 90^o and 180^o will also increase, meaning the backscattering effect will increase. As a result, more light flux will be lost from the incident light and the total transmittance will decrease. Direct transmittance decreases with increasing volume fraction, due the combined effect of the increase in the amount of light flux being scattered.

5.3.2 Effect of Size of Scatterers

Assume a fixed volume fraction of scatterers of 0.5. The intensity distribution of the scattering field is plotted against the scattering angle in Figure 5-6. For smaller scattering particles, the scattered intensity is more stable over all scattering angles. As a increases, the maximum scattered intensity starts to shift to lower angles, and the intensity distribution over scattering angles shows oscillatory patterns. As a increases further, the scattered intensity distribution shows multiple peaks. The number of peaks increases with a. Comparing the scattered intensity for $a = 0.4\mu$m and $a = 3\mu$m, the maximum is shifting towards lower angles and the amplitude of the intensity increases. At larger scattering angles, however, the scattered intensity of $a = 3\mu$m is significantly less than that of $a = 0.4\mu$m.

The scattering pattern for a point light source is shown in Figure 5-7. For small scattering particles, the diffused intensity is more uniform over the entire viewing area. Note that since the direct transmittance is not included in scattered intensity distribution, the scattering field does not include the bright spot in the center which represents the direct transmitted beam. As the size of scattering particles increases, rings start to appear and the intensity in the surrounding area is reduced. These rings correspond to the peaks

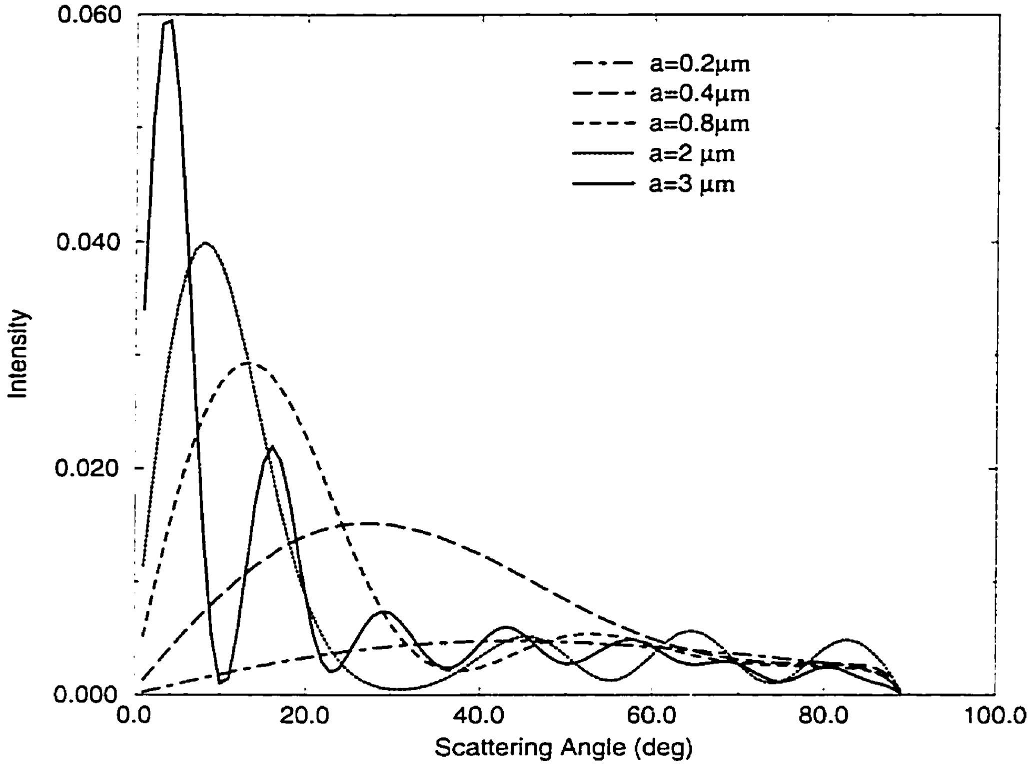

Figure 5-6: Scattering intensity distribution for different sizes of scattering particles, assuming scattering particles have the same volume fraction of 0.58

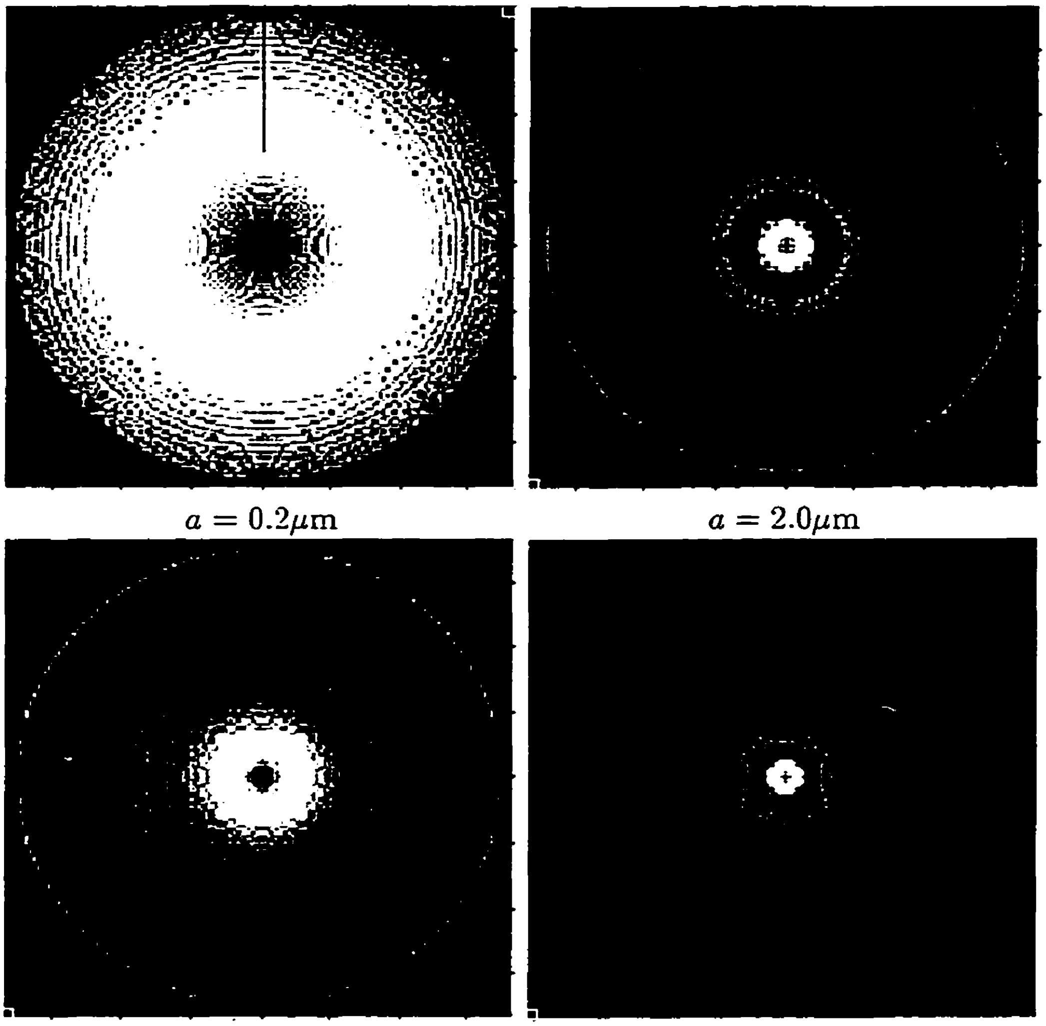

$a = 0.2\mu\text{m}$ $a = 2.0\mu\text{m}$

$a = 0.8\mu\text{m}$ $a = 3.0\mu\text{m}$

Figure 5-7: Scattering Patterns for various values of a

in the angular intensity distribution as shown in Figure 5-6. As a increases, the number of rings will increase. The intensity of ring decreases as the distance from the center increases. The brightest ring is the one nearest to the center. The results agree with the angular intensity distributions reported in earlier studies of the light scattering pattern by polymer films[75]. Starting from $a = 0.2\mu$m, the background which is originally uniformly black appears white due to the wide angle scattering by the spherulites. It leads to loss of contrast and makes the film appear hazy. When $a = 0.8\mu$m, haze reaches a maximum and then starts to decrease as a increases further. However, the narrow angle scattering effect increases with increasing a, indicating that the clarity of film deteriorates with larger spherulites. As shown in Figure 5-7, for $a = 3\mu$m the brightest ring is small and very close to the center. It represents the halos discussed in Figure 1-4. As the intensity of the halo increases, the exact image of the center spot can no longer be differentiated, which leads to loss of clarity.

Figure 5-8 shows the variation of transparency parameters with the diameter of scatterers. The volume fraction is 0.1 and the refractive index is 1.55. Figure 5-9 shows transparency parameters with the diameter of scatterers at volume fraction = 0.3. Maximum haze is achieved at $a = 0.8\mu$m for different values of volume fraction of spherulites. When the size of spherulites increases above 0.8μm, the transmittance increases and haze decreases. The transmitted light flux is the sum of two parts [40]. One is the intensity that passes unperturbed, and the other is the scattered intensity field. When the size of the spherulites a increases, the effect of scattering increases until it reaches a maximum. As the spherulites grow larger, the percentage of direct transmitted intensity increases and the effect of scattering decreases. In addition, the wide angle scattering decreases with increasing spherulite size, which leads to the decrease in haze.

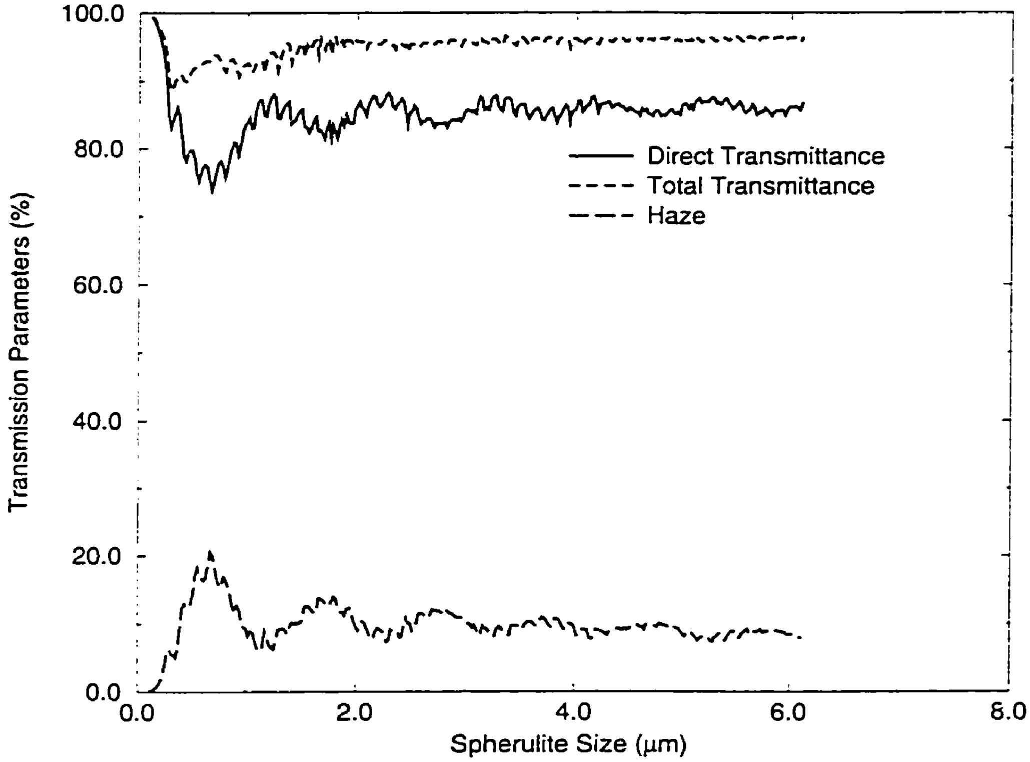

Figure 5-8: Transmission parameters as functions of diameter of scattering particles; volume fraction = 0.1

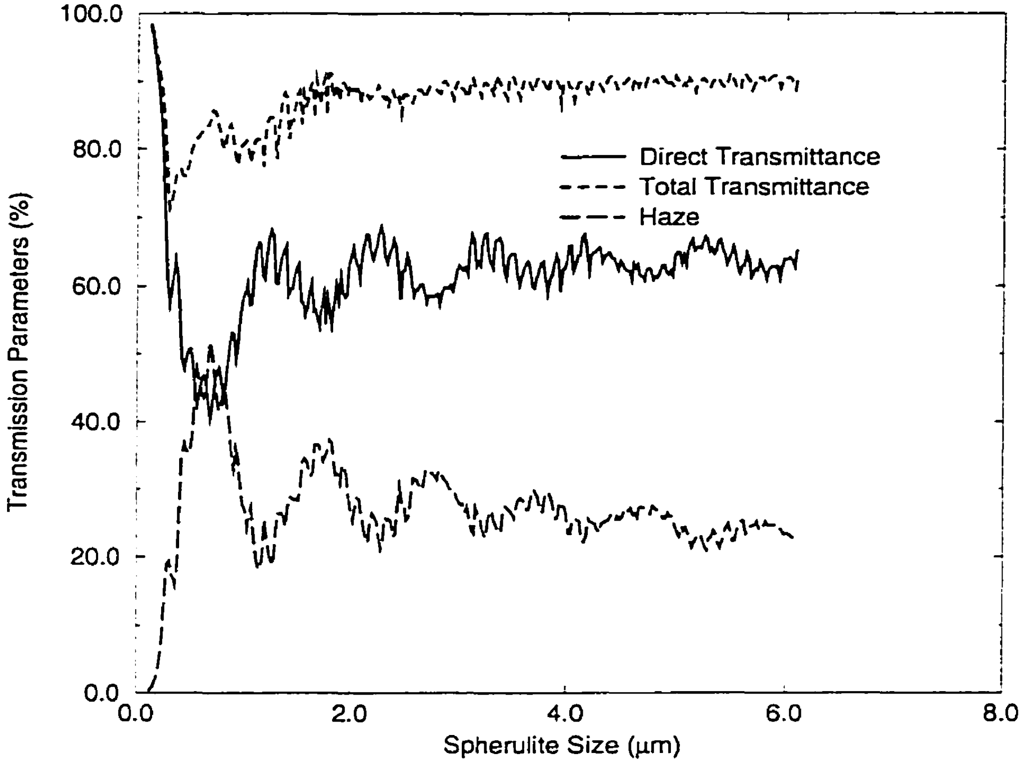

Figure 5-9: Transmission parameters as functions of diameter of scattering particles; volume fraction = 0.3

5.3.3 Effect of Refractive Index

Figure 5-10 shows haze for different spherulite diameters with refractive index of 1.55 and 1.75. The periodical profile of haze persists. For higher refractive index, the maximum haze occurs at smaller spherulite diameters.

To explain the effect of oil immersion on the haze of films as reported in [25], the surrounding medium is changed to oil with refractive index close to that of the spherulites. Figure 5-11 shows the haze for different sizes of scatterers with and without oil immersion. Here the refractive index of spherulites $m = 1.55$ and of oil $m_{oil} = 1.5$. The scattering geometry is the same for the two cases, but there is a significant reduction in haze in the presence of oil. This indicates that as the refractive index mismatch between the material and the surrounding medium becomes smaller, the effect of scattering is reduced significantly.

5.3.4 Haze of Polyethylene Film Samples

Figure 5-12 shows the computed values of haze for six different blown polyethylene film samples. These are compared to experimental measurements[74]. There is good agreement between experimental measurements and the theoretical values computed from the morphology information. The theoretical *predictions* are in general lower than the experimental values. This discrepancy is attributed to neglecting scattering in the bulk. As pointed out by Smith [25], the main contribution to transmission haze comes from the surface. The measurements of haze for polyethylene blown films before and after oil immersion showed up to 70% reduction in transmission haze. However, there is still a fair amount of light being scattered by the bulk of the film. Because of the assumption that the bulk of film does not contribute to light scattering, the calculated haze includes only the contribution of the surface. To include the effect of bulk on the light scattering as well as transmission haze, a detailed knowledge of the internal structure of the spherulites

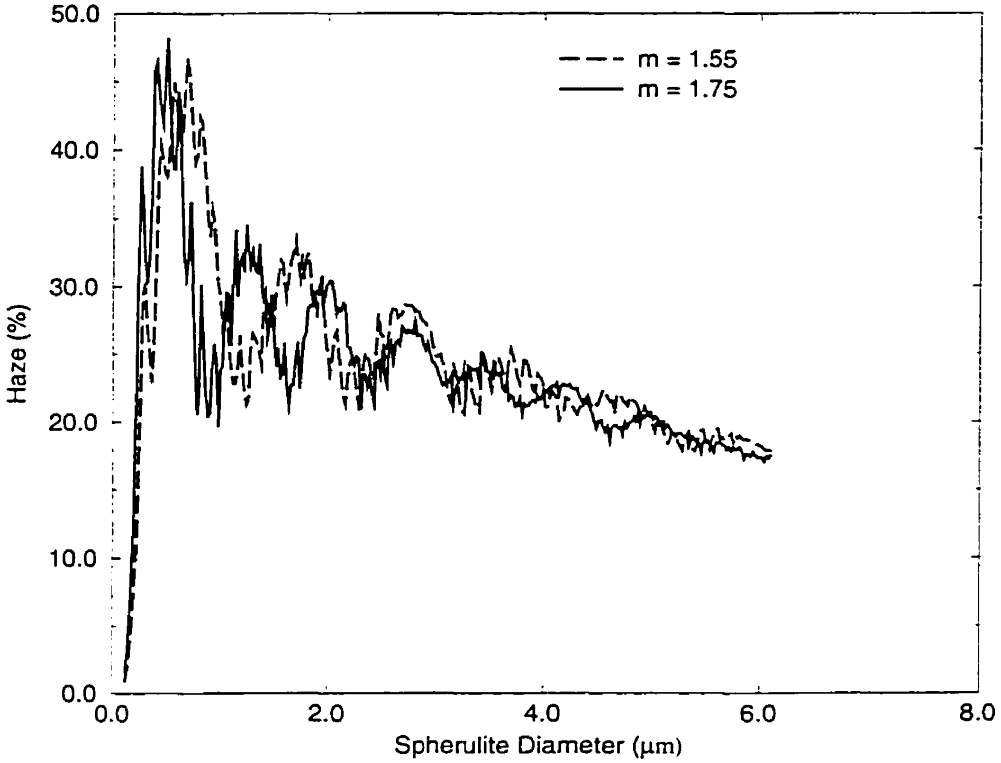

Figure 5-10: Effect of refractive index; Volume fraction = 0.3

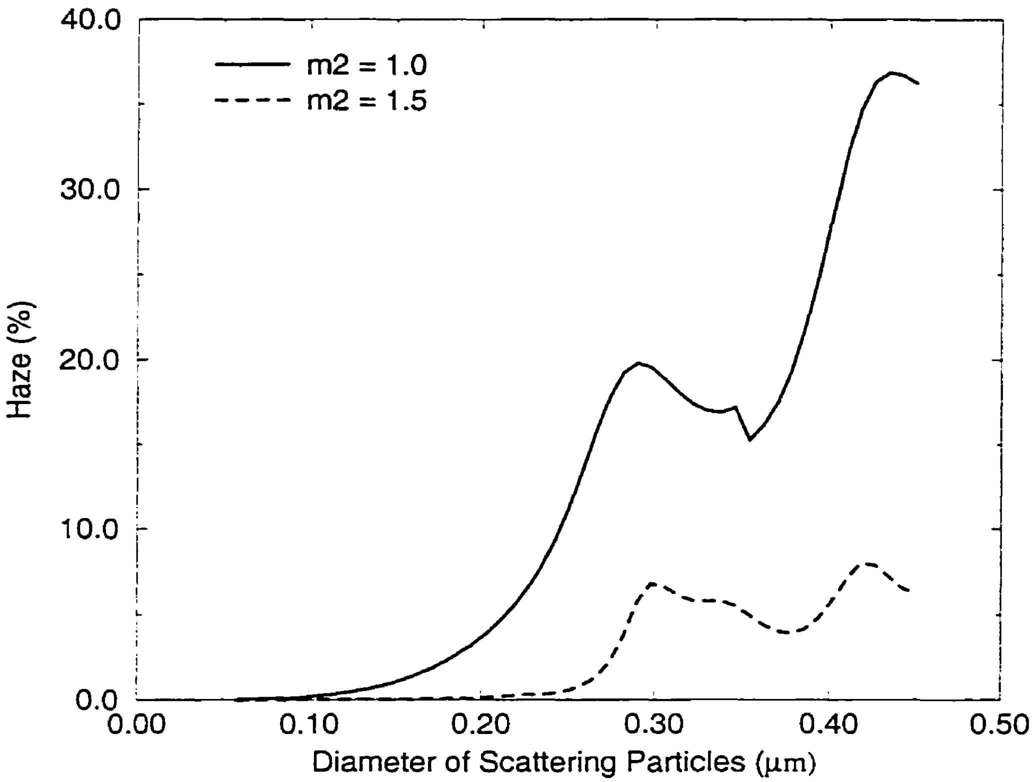

Figure 5-11: Effect of oil immersion; Volume fraction = 0.3, m=1.55, m_{oil}=1.5

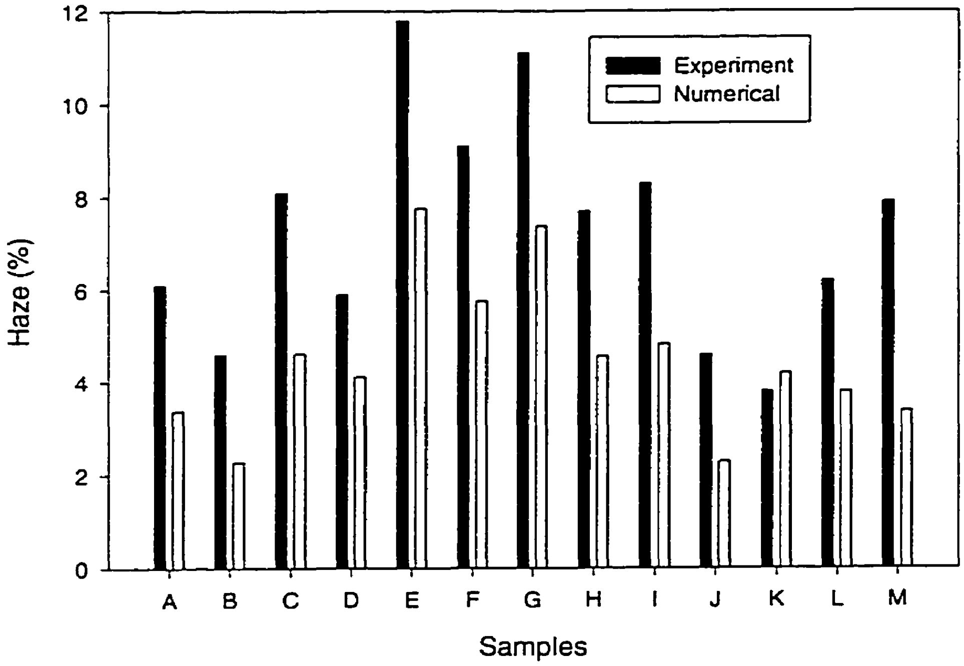

Figure 5-12: Comparison between the experimental haze measurements and values calculated from morphological information

is essential. In addition, when the bulk is not completely filled by impinged spherulites, the remaining amorphous area will become a source of light scattering.

5.3.5 Practical Implications

Maximum transparency is achieved at low volume fraction for different spherulite sizes. A lower volume fraction of spherulites on the surface indicates a smooth surface. This explains the correlation between the surface roughness of films shown in Figure 3-5 and the corresponding haze values in Figure 5-12. A smooth surface will have low haze and high transparency. As surface roughness increases, haze will increase. This positive correlation between the surface roughness and haze of PE films is confirmed by the results reported before [25].

For a fixed volume fraction, maximum haze is reached at a critical spherulite size a_c. When the size increases further, haze will decrease and the transparency of the film will improve, but clarity will decrease as the narrow angle scattering increases. The critical spherulite size a_c is dependent on the refractive index of the material. The higher is the refractive index, the smaller a_c will be. It follows that to minimize haze, the film must either have very small spherulites or very large ones. This can be achieved by adding nucleation agents, which causes high nucleation rates and a large number of small spherulites. Alternatively, increasing cooling rate will cause the film to solidify faster, thus limiting the growth of spherulites. On the other hand, one can also increase the cooling temperature without the addition of any nucleation agents. This will cause lower nucleation rates and longer cooling times, allowing the spherulites to grow. The drawback of larger spherulites is that although the transparency will improve in general, the clarity of film will not be as good as that of films with very small spherulites.

5.4 Summary

Based on the characterization of surface morphology and bulk morphology, a scattering geometry was proposed for the study of light scattering. A model based on the Mie theory of light scattering was developed to describe forward light transmission and scattering. Computations of light transmission by polymer thin films identified the important factors that influence the scattering of incident light and, accordingly, haze and transmittance of the film. The model is also applied to actual film samples to predict the haze. The theoretical results show reasonable agreement with experimental measurements.

Chapter 6

Conclusions and Original Contribution to Knowledge

6.1 Conclusions

Polyethylene blown films are widely used as packaging materials. The optical properties of the films are among the most important properties for this application. The optical properties included in this study are refractive index, gloss and haze.

As the fundamental optical property, refractive index is mostly a function of resin composition. When the detailed structural information of the resin is known, refractive index can be estimated from available group contribution theories. The important factors in determining the refractive index of a polymer are the monomer and comonomer types and ratio, total unsaturation, and the density. For LLDPE, high crystallinity leads to higher density and lower molar volume, if all other parameters are made constant. This decrease in molar volume will increase the refractive index n. Furthermore, increasing comonomer contents or decreasing the amount of total unsaturation will increase the molar refraction R, which leads to larger values of n. The molecular weight M_w, polydispersity M_w/M_n and chain branching of the polymer are not directly included in the group contribution theory. However, these parameters will influence the crystallization during the production process and result in the density variation of the final product. Since the density is a factor in determining the refractive index, the refractive index is indirectly influenced by M_w, M_w/M_n and chain branching. However, whether the density alone can account for all the influence of M_w, M_w/M_n and chain branching in determining the refractive index is not certain.

The method of Transmission Spectrum has been adopted in this study to measure the refractive indices of sample films. The advantage of this method lies in its simplicity in operation and sample preparation. The theoretical formulations underlying the measurements are rigorous and in closed form. Also, the same measurements may be used to determine the thickness of sample film from the transmission spectrum independently.

The present research is based on the consideration that, besides composition, the critical factor determining the optical properties of polyolefin films is their morphology. Film surface morphology is evaluated using a combination of AFM and NSOM techniques. The bulk morphology is obtained from the cross-section of the sample prepared, by ultracryomicrotomy. The study proposes techniques for comprehensive and quantitative characterization of the morphology of polymer films.

Observations from morphological information confirm the spherulitic structure on the surface, as well as in the bulk of the sample films. Resin composition and processing conditions play a critical role in the formation of surface roughness. The surface morphology is characterized using parameters such as the standard deviation of surface roughness, lateral correlation length and fractal dimensions. The results are used in the study of light reflection and transmission by the films. Since the characterization methods are not material-dependent, they can be applied to all kinds of complex geometries.

A model was developed to compute the reflection of light by the rough surface of polymer films based on the Beckmann-Davies theory of the reflection of electro-magnetic waves by a rough surface. The directional distribution of reflected intensity was computed for various surface morphologies. It is found that surface roughness is the dominant factor in determining the specular reflection of the surface. The parameters considered are standard deviation of surface height σ and lateral correlation function $C(T)$, here T is the correlation length. Small σ values and large T represent a smooth surface with small variation of surface height.Also, the roughness is sparsely spaced. Consequently, the diffuse reflection of the surface is less significant and the surface will appear glossy or shiny. On the other end, large σ values represent large surface height variation, which corresponds to a very rough surface. Small T values indicate roughness is more randomly and densely packed on the surface. As a result, incident light will be mostly diffused and the surface will appear matt.

The gloss of films was computed by combining the proposed model with the results of the statistical characterization of surface morphology of the films. The computed gloss values were in good agreement with the experimental measurements. Generally, the computed gloss values were lower than the experimental measurements. For highly transparent films, the discrepancy between computed values and measurements was larger. This is because the reflection of both film surfaces is combined in experimental gloss measurements with the glossmeter. In fact, it is possible to have a measured gloss value larger than 100% due to the double reflection. Double reflection is not considered in the computation of surface reflection, and the computed light intensity includes only the reflection of the top surface.

Light transmission and haze of polymer films involves more complicated issues. Previous experimental studies have shown that the surface of the films is the dominant factor in determining the haze of polymer films. The effect of light scattering at the surface and its relationship to the haze of the film have not been addressed by any previous theoretical studies.

In this project, based on the characterization of surface and bulk morphology, a scattering geometry is proposed for the study of light scattering. A model based on the Mie theory of light scattering was developed to describe forward light transmission and scattering.

Maximum transparency is achieved at low volume fraction for different spherulite sizes. Lower volume fraction of spherulites on the surface indicates a smooth surface. This explains the correlation between surface roughness of films and haze. A smooth surface will have low haze and high transparency. As surface roughness increases, haze will increase. This positive correlation between the surface roughness and haze of polyethylene films is confirmed by results previously reported in the literature.

For a fixed volume fraction, maximum haze is reached at a critical spherulite size. When the size increases further, haze will decrease and transparency of the film will improve, but clarity will decrease as the narrow angle scattering increases. The critical spherulite size is dependent on the refractive index of the material. The higher is the refractive index, the smaller the critical spherulite size will be. It follows that to minimize haze, the film must either have very small spherulites or very large ones. This can be achieved by adding nucleating agents, which causes high nucleation rates and a large number of small spherulites. Alternatively, increasing the cooling rate will cause the film to solidify faster. thus limiting the growth of spherulites. On the other hand, one can also increase the cooling temperature without adding in any nucleation agents. This will cause lower nucleation rates and longer cooling times, allowing the spherulites to grow. The drawback of larger spherulites is that although the transparency will improve in general, the clarity of film will not be as good as that of films with very small spherulites.

6.2 Suggestions for future studies

This project presents a comprehensive study regarding the influence of the morphology of polyethylene films on their optical properties. In order to apply this knowledge directly in industrial practice, one must also understand the formation of morphology and the important factors that influence it. This should include an evaluation of the dependence of crystallization behavior and morphology development on molecular weight, molecular weight distribution, chain branching and comonomer type and ratio. Ultimately, crystallization behavior and morphological models need to be incorporated in film blowing models depicting the thermo-mechanical history experienced by the material during processing.

6.3 Original Contributions to Knowledge

The present thesis represents a significant step towards improved understanding of polyethylene blown film morphology. It also provides a comprehensive study of the relationships between morphology and optical properties of these films. To our knowledge, the present work is the most comprehensive integrated study of morphology and optical properties of polyethylene films and the relationship between them. Furthermore, while some components of the following claims have been the subject of other studies, no studies have reported the full integration of the findings involving each of these claims.

1. Atomic Force Microscopy (AFM) and Near-field Scanning Optical Microscopy (NSOM) were used to elucidate the surface topography of polyethylene blown thin films.

2. Quantitative characterization methods are applied to describe the surface morphology. The roughness of surface morphology of films is characterized by the standard deviation of z height. The lateral correlation function $C(\tau)$ and lateral correlation length T are introduced to represent the characteristics and the distribution of surface roughness.

The line fractal dimension L_f is introduced to characterize the general size and shape of spherulites and their directional distribution. It also indicates if there is any orientational preference, either in shape or distribution, of the spherulites on the surface. The two-dimensional fractal dimension D_f is introduced to characterize the size distribution and the clustering of the spherulites on the surface. The domain analysis is introduced to separate and survey the spherulites on the surface of films.

3. The bulk morphology of polyethylene blown films is obtained by studying the cross-section of sample films. It is shown that the bulk of the films consists of impinged spherulites that are uniform in size.

4. Specular reflection and the angular intensity distribution by the surface of polyethylene blown films are investigated. The gloss value is computed for sample films using the quantitative morphological information obtained from AFM/NSOM images.

5. Forward light transmission and haze of sample films are investigated. The haze of polyethylene blown films is regarded as a result of light scattering at the surface of the film. A model is proposed to study the surface scattering, based on experimental observation of film morphology. The values of haze of sample films are computed from their surface morphologies. Practical implications are discussed and directions are provided to optimize the transparency of polyethylene blown films.

6. The method of Transmission Spectrum is adopted to measure the refractive index of polyethylene blown thin films. The advantages of this method are that it requires minimum sample preparation and can determine the thickness of the sample independently. The results are compared to values estimated using group contribution models.

Bibliography

[1] D. G. Baird. *Polymer Processing: Principles and Design.* Wiley, New York, 1998.

[2] A. Keller. *Phil. Mag.*, (8)2:1171, 1957.

[3] B. Lotz. *Nuct. Instr. and Meth. in Phys. Res. B*, 131:13, 1997.

[4] D. W. van Krevelen. *Properties of Polymers: their correlation with chemical structure, their numerical estimation and prediction from additive group contributions.* Elsevier, Amsterdam, 3rd edition, 1990.

[5] ASTM D1729: Standard practice for visual appraisal of colors and color differences of diffusely-illuminated opaque materials, 1996.

[6] ASTM D2457: Specular gloss of plastic films and solid plastics, 1990.

[7] M. Born and E. Wolf. *Principle of Optics.* Pergamon, Oxford, 6th edition, 1980.

[8] G. H. Meeten. Refraction and extinction of polymers. In G. H. Meeten, editor, *Optics of Polymers.* Elsevier Applied Science, New York, 1986.

[9] L. V. Lorenz. *Wied. Ann. Phys.*, 11:70, 1880.

[10] H. A. Lorentz. *Wied. Ann. Phys.*, 9:641, 1880.

[11] J. H. Gladstone and T. P. Dale. *Transactions of the Royal Society(London)*, A148:887, 1858.

[12] D. J. Goedhart. *Communication Gel Permeation Chromatography International seminar.* Monaco, Oct 1961.

[13] J. C. Seferis. In J. Brandrup and E. H. Immergut, editors, *Polymer Handbook*. Wiley, New York, 3rd edition, 1989.

[14] J. Bicerano. *Prediction of Polymer Properties.* Marcel Dekker Inc., New York, New York, 2nd edition, 1996.

[15] V. Shah. *Handbook of Plastics Testing Technology.* Wiley, New York, 1984.

[16] R. Swanepoel. *J. Phys. E.: Sci. Instr.*, 16:1214, 1983.

[17] U. Dürig, D. W. Pohl, and H. Rohrer. *J. Appl. Phys.*, 59:3318, 1986.

[18] E. Betzig, A. Lewis, A. Harootunian, M. Isaacson, and E. Jratschmer. *Biophys. J.*, 49:269, 1986.

[19] E. Betzig, P. L. Finn, and J. S. Weiner. *Appl. Phys. Lett.*, 60:2484, 1992.

[20] R. Toledo-Crow, P. Yang, Y. Chen, and M. Vaez-Iravani. *Appl. Phys. Lett.*, 60:2957, 1992.

[21] K. Karrai and P. D. Grober. *Appl. Phys. Lett.*, 66(14):1842, 1995.

[22] D. Sarid. *Scanning Force Microscopy with Applications to Electric, Magnetic and Atomic Forces.* Oxford University Press, Oxford, England, 1991.

[23] E. Betzig and J. K. Trautman. *Science*, 257:189, 1992.

[24] E. Betzig, J. K. Trautmann, J. S. Weiner, T. D. Harris, and R. Wolfe. *Appl. Optics*, 31(22):4563, 1991.

[25] P.F. Smith, I. Chun, G. Liu, D. Dimitrievich, J. Rasburn, and G.J. Vancso. *Poly. Eng. Sci.*, 36(16):2129, 1996.

[26] L. Reimer. *Transmission Electron Microscopy: Physics of Image Formation and Microanalysis.* Springer, Berlin; New York, 4th edition, 1997.

[27] J.M. Bennet and L. Mattsson. *Introduction to Surface Roughness and Scattering.* Optical Society of America, Washington D.C., 1989.

[28] T.R. Lettieri, E. Marx, J.F. Song, and T.V. Vorburger. *Appl. Opt.*, 30(30):4439, 1991.

[29] B. B. Mandelbrot. *The Fractal Geometry of Nature.* Freeman, San Francisco, 1977.

[30] S. Chesters, H. Wang, and G. Kasper. *Solid State Tech.*, 34:73, 1991.

[31] J. M. Gomez-Rodriguez. *Vac. Sci. Technol. B.*, 9(2):495, 1991.

[32] J. M. Gomez-Rodriguez, A. Asenjo, R. C. Salvarezza, and A. M. Baro. *Ultramiscroscopy*, 42-44:1321, 1992.

[33] D.J. Whitehouse, D.K. Bowen, V.C. Venkatesh, P. Lonardo, and C.A. Brown. Gloss and surface topography. *Cirp Annals*, 43(2):541, 1994.

[34] E. R. Mendez, R. G. Barrera, and R. Alexander-Katz. *Physica A*, 207:137, 1994.

[35] B. Alexander-Katz and R.G. Barrera. *J. Polym. Sci.: Part B: Polym. Phys.*, 36:1203, 1998.

[36] H. Davies. *Proc. Inst. Elec. Eng. Part IV*, 101:209, 1954.

[37] P. Beckmann and A. Spizzichino. *The Scattering of Electromagnetic Waves from Rough Surfaces.* MacMillan Company, New York, 1963.

[38] R.S. Hunter. *Product Engineering*, 27:176, 1956.

[39] E. M. Mount. *ANTEC Proceedings*, 45:194, 1987.

[40] M. Kerker. *The scattering of light and other electromagnetic radiation.* Academic Press, New York, 1969.

[41] G. H. Meeten. *Optica Acta*, 29:759, 1982.

[42] R.S. Stein and M.B. Rhodes. *J. Appl. Phys.*, 31:1873, 1960.

[43] R.S. Stein and R. Prud'homme. *J. Polym. Sci. B, Polym. Lett.*, 9:595, 1971.

[44] S. Clough, J. J. van Aartsen, and R. S. Stein. *J. Appl. Phys.*, 63(10):3072, 1963.

[45] R. S. Stein and W. Chu. *J. Polym. Sci.: Part A-2*, 8:1137, 1970.

[46] D. Yoon and R.S. Stein. *J. Polym. Sci., Polym. Phys. Ed.*, 12:763, 1974.

[47] D. Y. Yoon, C. Chang, and R. S. Stein. *J. Polym. Sci.: Polym. Phys. Ed.*, 13:2091, 1974.

[48] R. E. Prud'homme, L. Bourland, R. T. Natarajan, and R. S. Stein. *J. Polym. Sci.: Polym. Phys. Ed.*, 13:1955, 1974.

[49] T. Hashimoto, A. Todo, and H. Kawal. *J. Polym. Sci. Polym. Phys. Ed.*, 11:149, 1973.

[50] T. Hashimoto and R.S. Stein. *J. Polym. Sci. A*, 9:1747, 1971.

[51] R. S. Stein and C. Picot. *J. Polym. Sci.: Part A*, 8:2127, 1970.

[52] R.E. Prud'homme and R.S. Stein. *J. Polym. Sci., Polym. Phys. Ed.*, 11:1357, 1973.

[53] D. Yoon and R.S. Stein. *J. Polym. Sci., Polym. Phys. Ed.*, 12:735, 1974.

[54] F. M. Willmouth. Transparency, transclucency and gloss. In G. H. Meeten, editor, *Optics of Polymers.* Elsevier Applied Science, New York, 1986.

[55] N. A. Vaz, W. Smith, and G. P. Montgomery Jr. *Mol. Cryst. Liq. Cryst.*, 146:1, 1987.

[56] R. D. Sherman. *Phys. Rev. A.*, 40:1591, 1989.

[57] S. Zumer and J. W. Doane. *Phys. Rev. A*, 37:3373, 1986.

[58] G. P. Montgomery Jr. and J. L. West. *Phys. Rev. A*, 40:6580, 1989.

[59] F. Bloisi, C. Ruocchio, P. Terrecuso, and I. Vicari. Pdlc: influence of droplet order parameter in light transmittance. *Optics Communications*, 123:449, 1996.

[60] A. Friedman and B. Hu. *SIAM J. Appl. Math.*, 52(1):46, 1992.

[61] P.L. Clegg and N. D. Huck. *Plastics*, 26:114, April 1961.

[62] N.D. Huck and P.L. Clegg. *SPE Trans.*, 1:121, 1961.

[63] H.G. Fritz and J. Rothe. *Kunststoffe*, 59:471, 1969.

[64] M. Hert, N.H. Dac, and A. Sauzeau. *Off. Plast. Caout.*, 28:285, Jan/Feb 1981.

[65] R. Giuffria. *J. Polym. Sci.*, 49:427, 1961.

[66] I. Ouchi. *Japan J. Polym. Phys.*, 5:348, 1966.

[67] I. Ouchi, T. Yokoyama, and Y. Tokai. *Japan J. Apply. Phys.*, 5:545, 1966.

[68] S.Y. Hobbs and C.F. Pratt. *Polym. Eng. Sci.*, 22:594, 1982.

[69] C.J. Su. *Polym. Plast. Technol. Eng.*, 14:181, 1980.

[70] S. A. Jabrain. *Polym. Eng. Sci.*, 22:815, 1982.

[71] M. B. Khan and C. Keener. *Polym. Eng. Sci.*, 36:1290, 1996.

[72] G. J. Vancso and G. Liu. *J. Eng. Appl. Sci.*, 2:2355, 1996.

[73] R. H. Olley and D. C. Basset. *J. Macromol. Sci. Phys.*, n2:209, 1994.

[74] ASTM D1003: Standard test method for haze and luminous transmittance of transparent plastics, 1992.

[75] R. J. Samuels. *J. Polym. Sci., Part A-2*, 9:2165, 1983.

Appendix A

Transmission spectra and refractive index of sample films

The measurements of transmission spectra and calculations of refractive indices for all sample films are listed below.

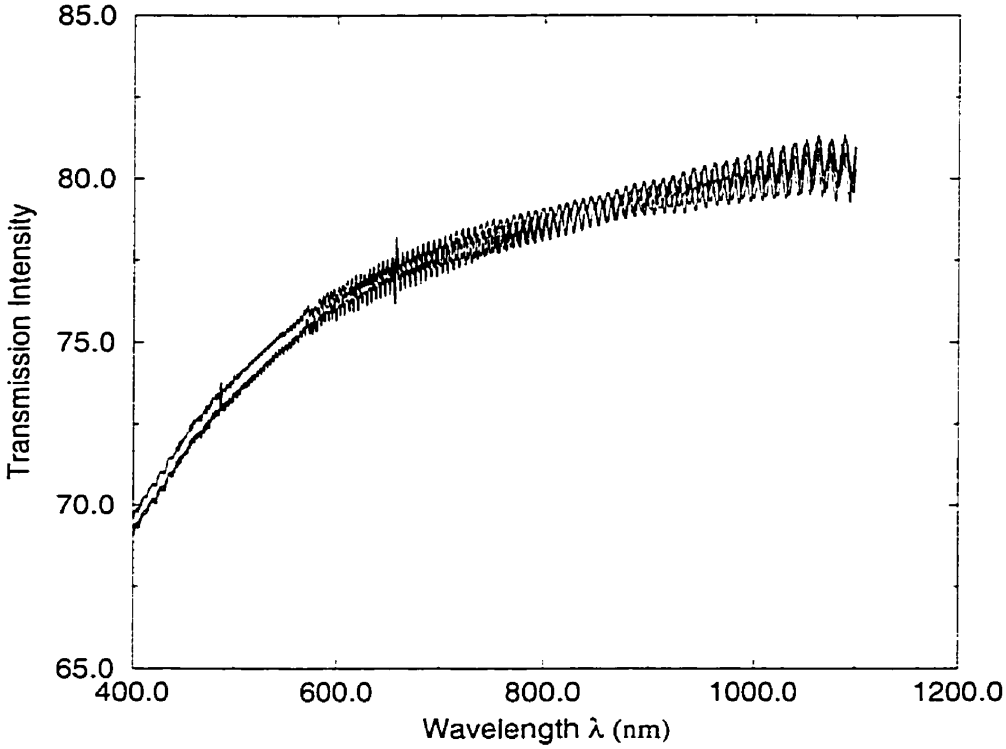

Measurement	n	d μm	a $\times 10^{-6}$
1	1.524	23.95	5.55
2	1.538	25.73	4.85
3	1.535	25.74	4.82
4	1.544	27.23	4.78

n_{ave}=1.54 σ_n= 0.03 d_{ave}=25.63μm σ_d=1.16

Figure A-1: Transmission spectra and refractive index of Sample A

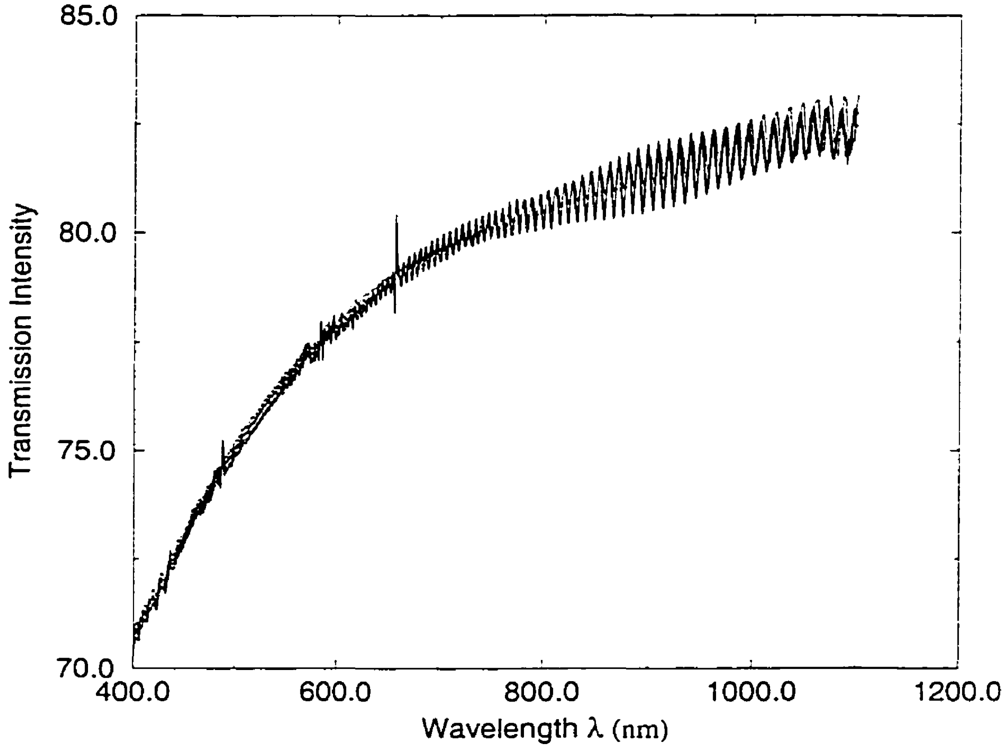

Measurement	n	d μm	a $\times 10^{-6}$
1	1.540	23.08	4.52
2	1.534	22.35	4.56
3	1.495	21.22	4.85
4	1.514	22.62	4.55
5	1.577	23.29	4.44
n_{ave}=1.53	σ_n= 0.03	d_{ave}=22.51μm	σ_d=0.14

Figure A-2: Transmission spectra and refractive index of Sample B

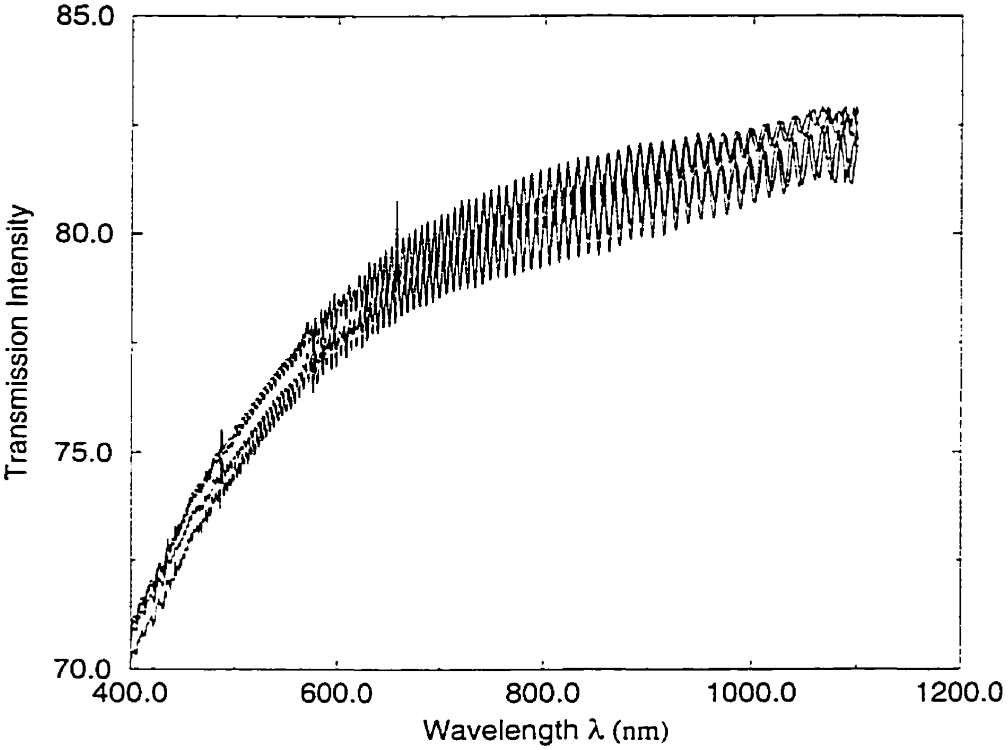

Measurement	n	d μm	a $\times 10^{-6}$
1	1.517	20.66	5.82
2	1.483	19.41	5.13
3	1.528	19.15	6.12
4	1.455	18.5	5.6
5	1.527	21.09	5.81

n_{ave}=1.50 σ_n= 0.04 d_{ave}=19.76μm σ_d=0.88

Figure A-3: Transmission spectra and refractive index of Sample C

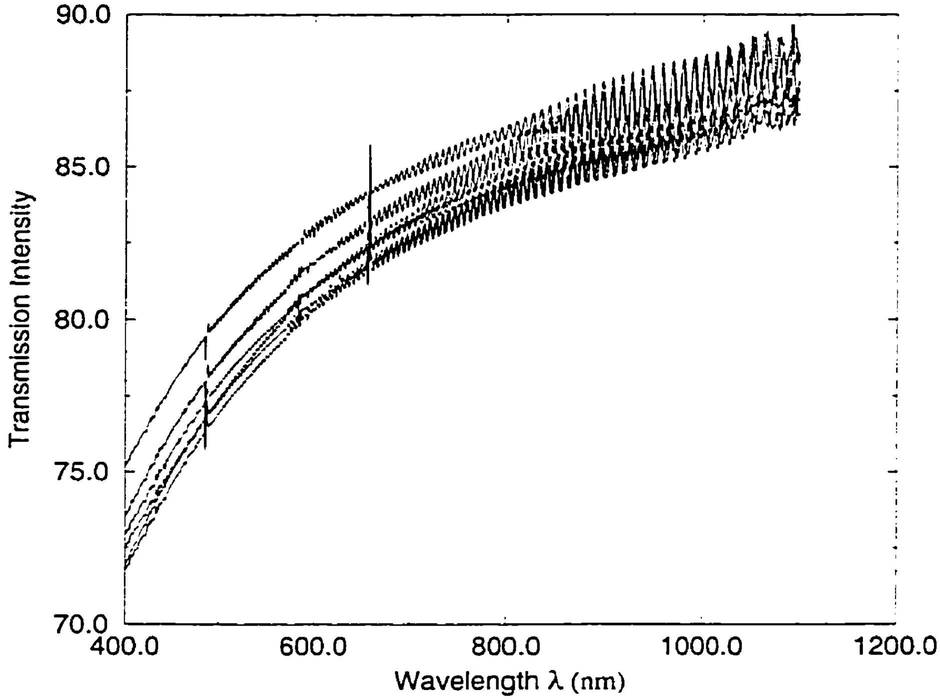

Measurement	n	d μm	a $\times 10^{-6}$
1	1.471	20.72	2.56
2	1.457	19.89	2.41
3	1.554	23.18	1.96
4	1.543	24	1.32
5	1.511	22.9	2.42

n_{ave}=1.5 σ_n= 0.04 d_{ave}=22.14μm σ_d=1.56

Figure A-4: Transmission spectra and refractive index of Sample D

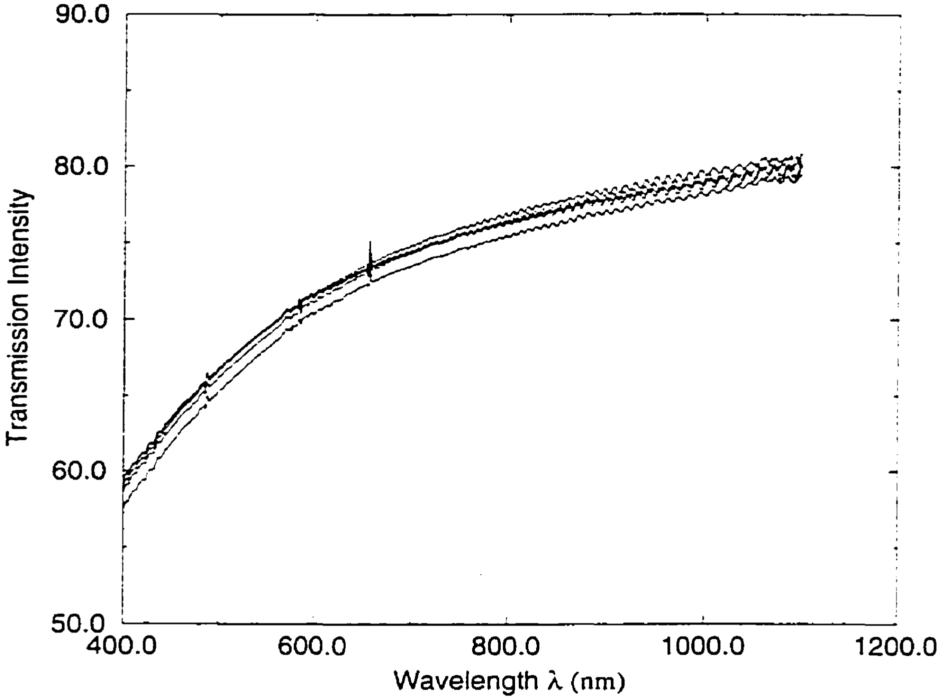

Measurement	n	d μm	$a \times 10^{-6}$
1	1.513	21.61	7.25
2	1.459	20.33	7.76
3	1.500	22.77	6.31
4	1.488	22.91	6.44
5	1.508	23.14	7.07

n_{ave}=1.50 σ_n= 0.027 d_{ave}=22.15μm σ_d=1.05

Figure A-5: Transmission spectra and refractive index of Sample E

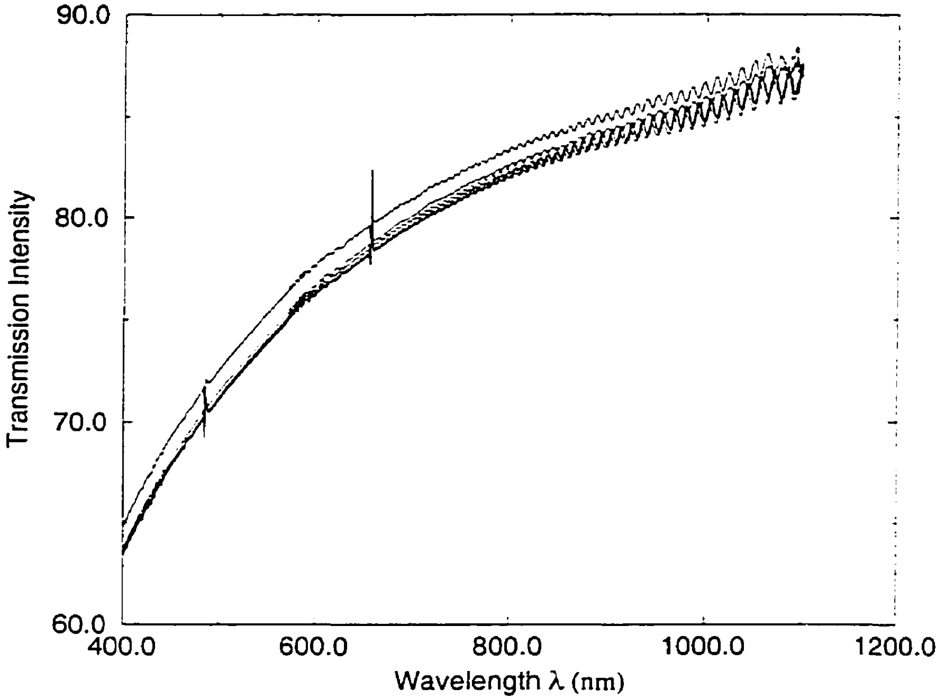

Measurement	n	d μm	a $\times 10^{-6}$
1	1.500	22.08	3.11
2	1.488	22.12	3.38
3	1.533	22.5	3.98
4	1.507	22.02	3.57
5	1.514	21.64	4.09

n_{ave}=1.51 σ_n= 0.013 d_{ave}=22.10μm σ_d=0.38

Figure A-6: Transmission spectra and refractive index of Sample G

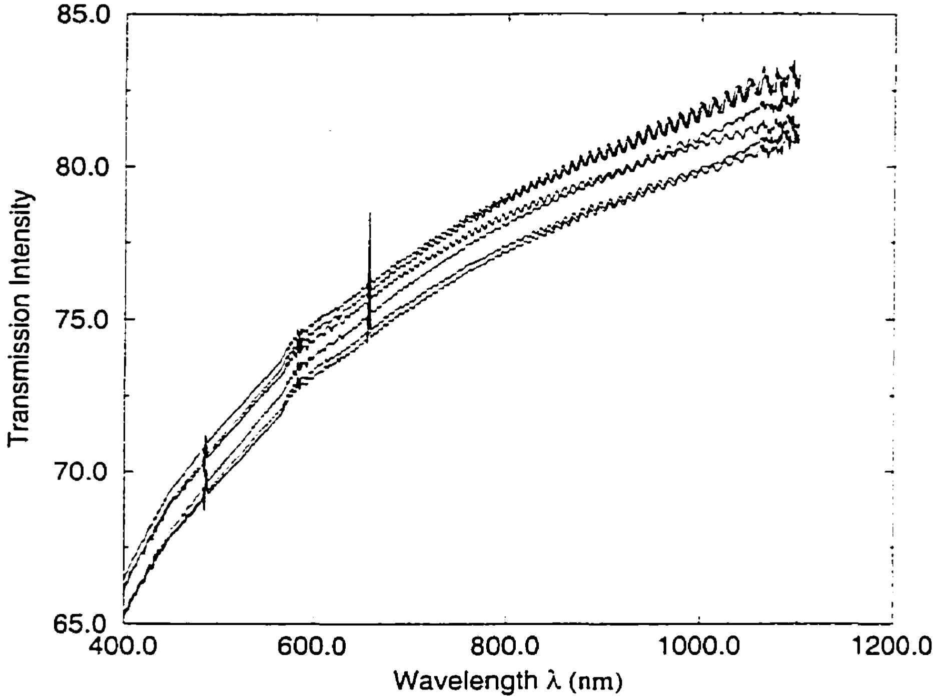

Measurement	n	d μm	a $\times 10^{-6}$
1	1.459	22.83	5.62
2	1.488	23.49	6.06
3	1.514	23.23	5.09
4	1.526	23.51	4.99
5	1.503	23.64	5.73
n_{ave}=1.50	σ_n= 0.023	d_{ave}=23.35μm	σ_d=0.46

Figure A-7: Transmission spectra and refractive index of Sample H

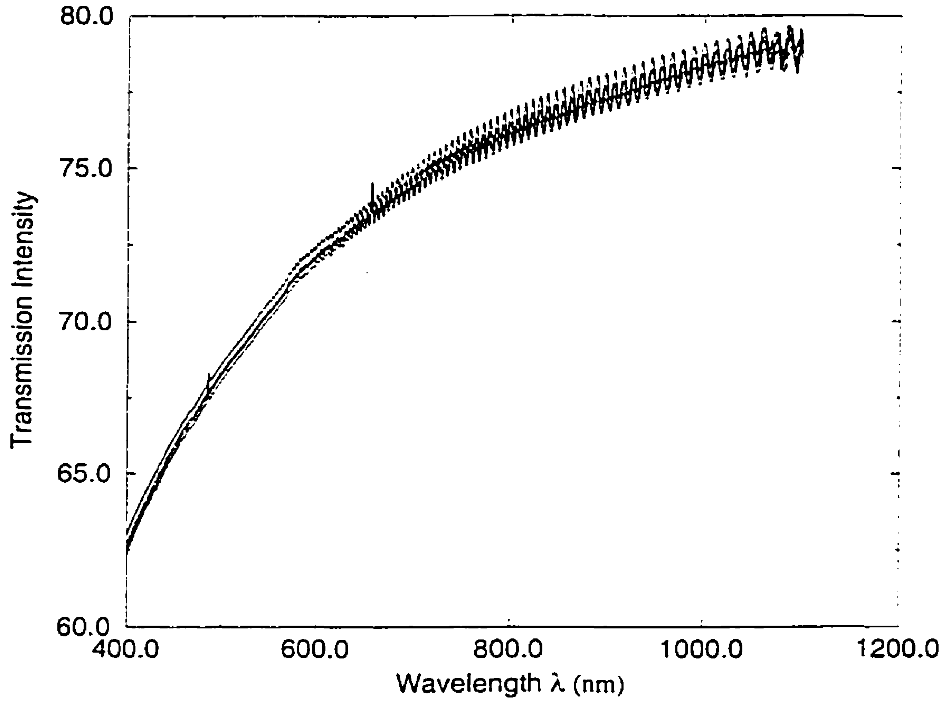

Measurement	n	d μm	a $\times 10^{-6}$
1	1.495	23.00	6.6
2	1.516	24.18	6.57
3	1.489	23.08	6.63
4	1.512	23.78	6.24
5	1.535	22.77	6.46

n_{ave}=1.51 σ_n= 0.019 d_{ave}=23.51μm σ_d=0.58

Figure A-8: Transmission spectra and refractive index of Sample I

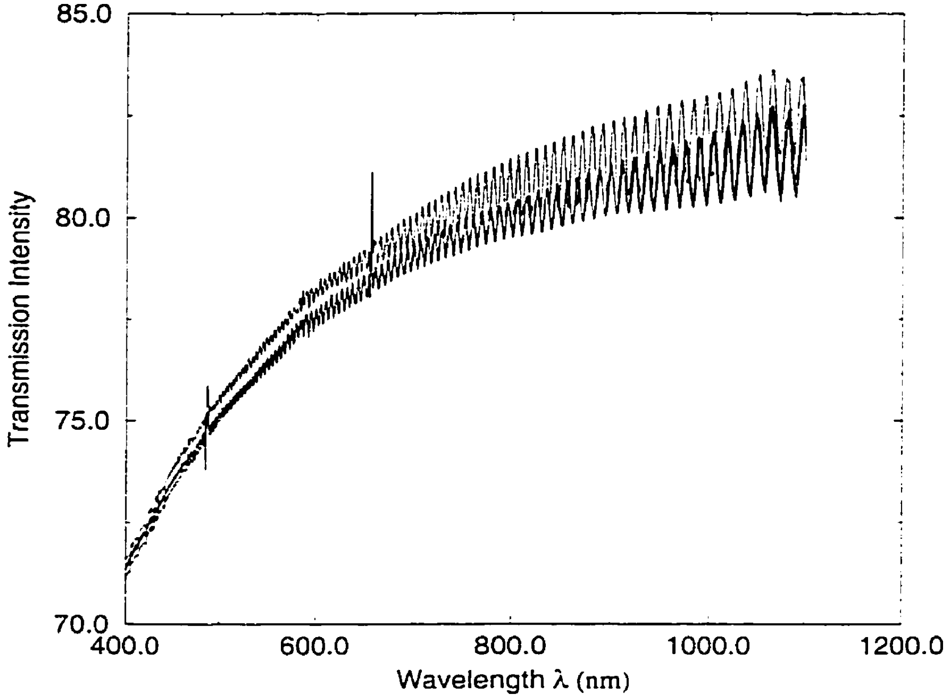

Measurement	n	d μm	a $\times 10^{-6}$
1	1.569	20.50	5.84
2	1.549	19.77	6.00
3	1.567	20.40	5.80
4	1.608	20.61	5.79
5	1.588	21.83	5.64

n_{ave}=1.57 σ_n= 0.029 d_{ave}=20.62μm σ_d=0.67

Figure A-9: Transmission spectra and refractive index of Sample J

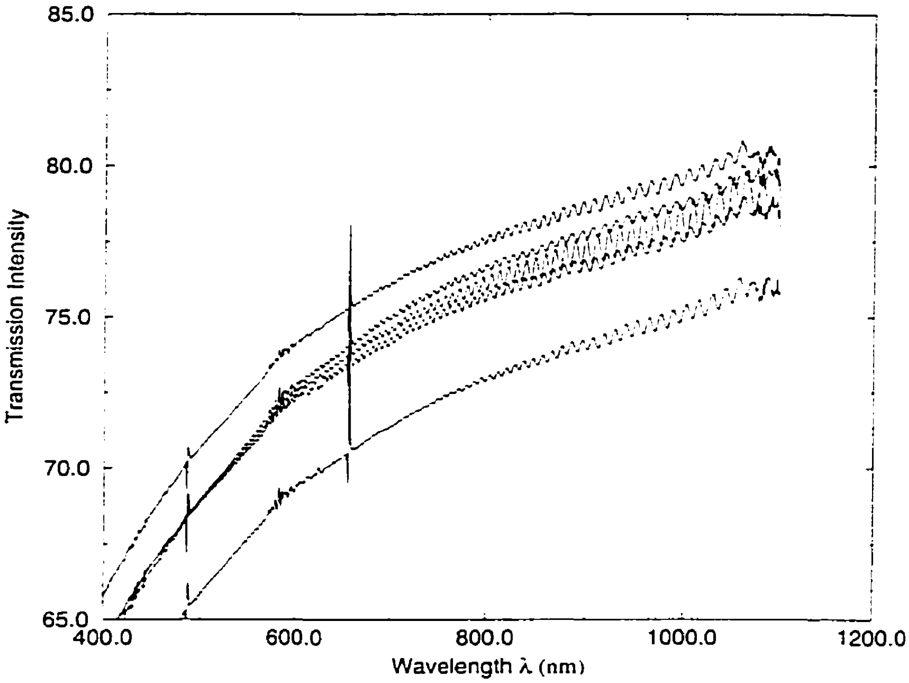

Measurement	n	d μm	$a \times 10^{-6}$
1	1.526	22.03	6.5
2	1.513	21.46	6.53
3	1.501	21.93	6.67
4	1.523	22.11	6.21
5	1.512	21.56	6.06

n_{ave}=1.51 σ_n= 0.024 d_{ave}=21.82μm σ_d=0.26

Figure A-10: Transmission spectra and refractive index of Sample L

Appendix B

Surface morphology of sample films

The outside and inside surfaces of all sample films are presented below.

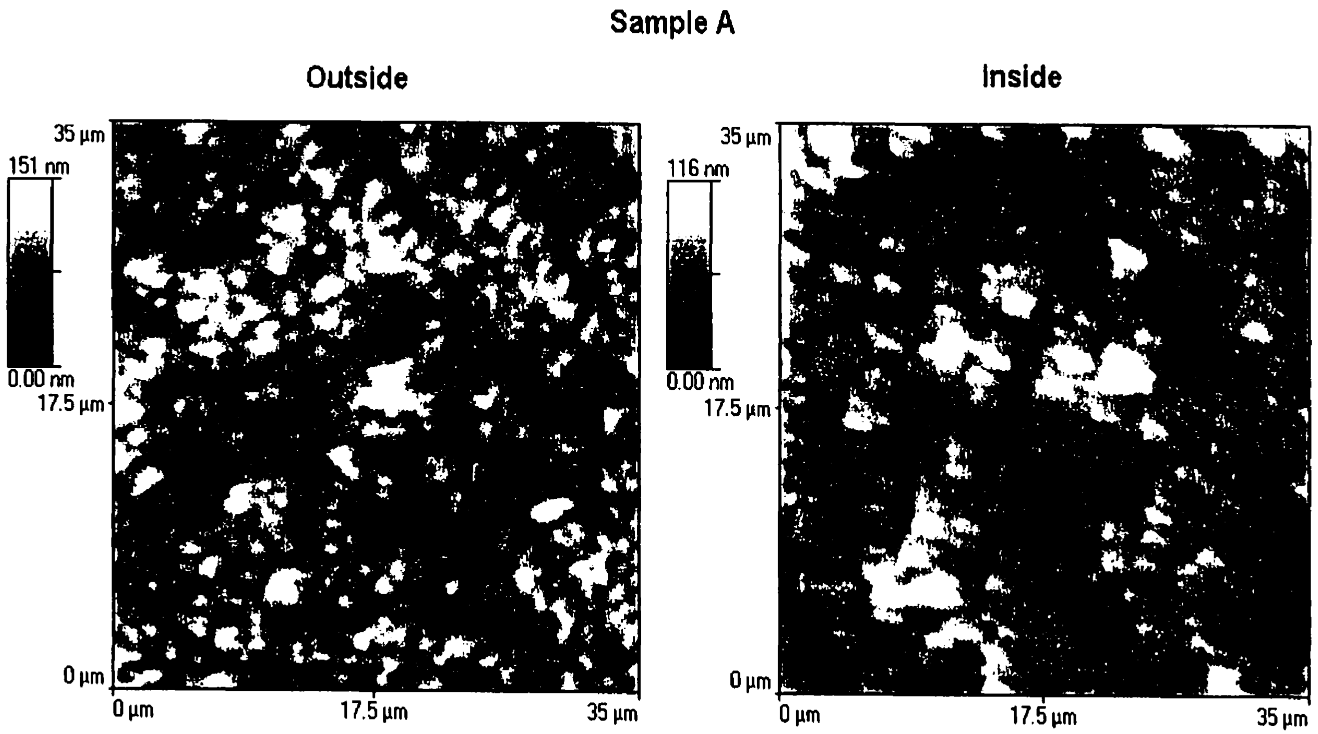

Figure B-1: Outside and Inside surfaces of Sample A (P972403:978585)

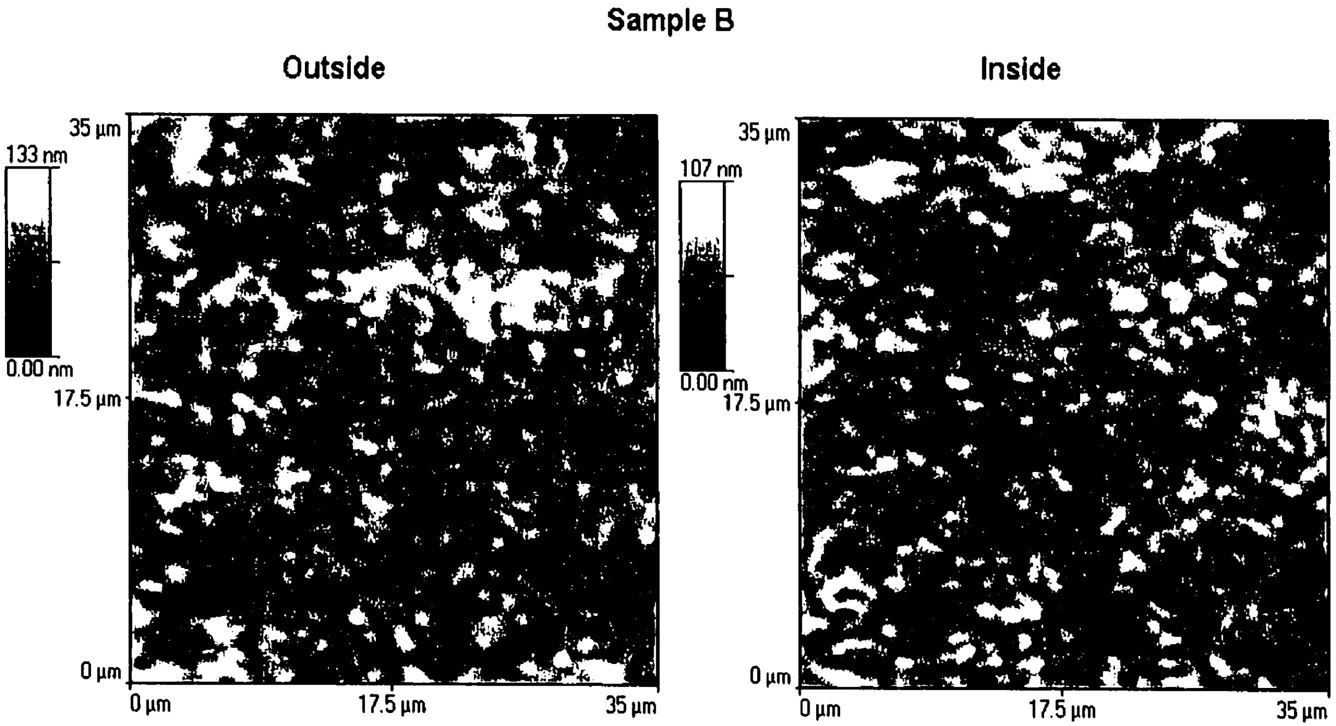

Figure B-2: Outside and Inside surfaces of Sample B (P972403:978586)

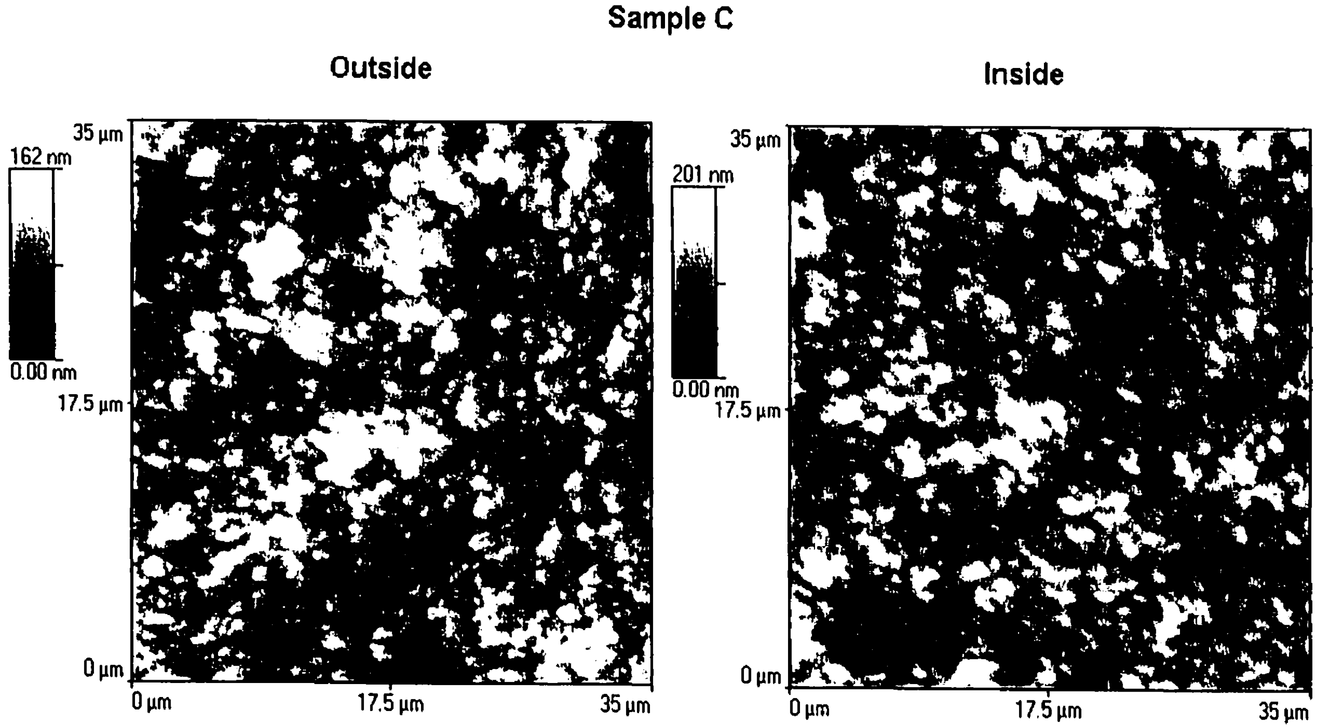

Figure B-3: Outside and Inside surfaces of Sample C (P972403:978587)

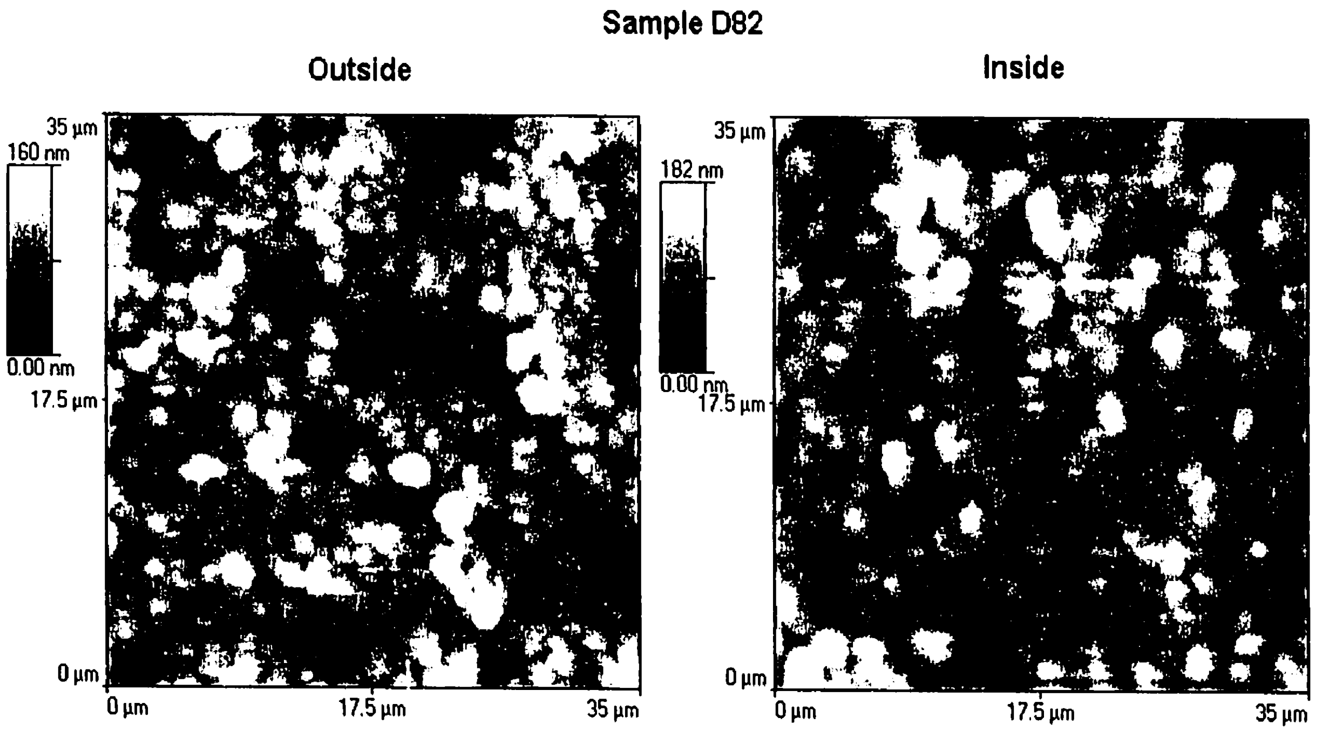
Sample D82

Outside

Inside

Figure B-4: Outside and Inside surfaces of Sample D82 (P972403:978582)

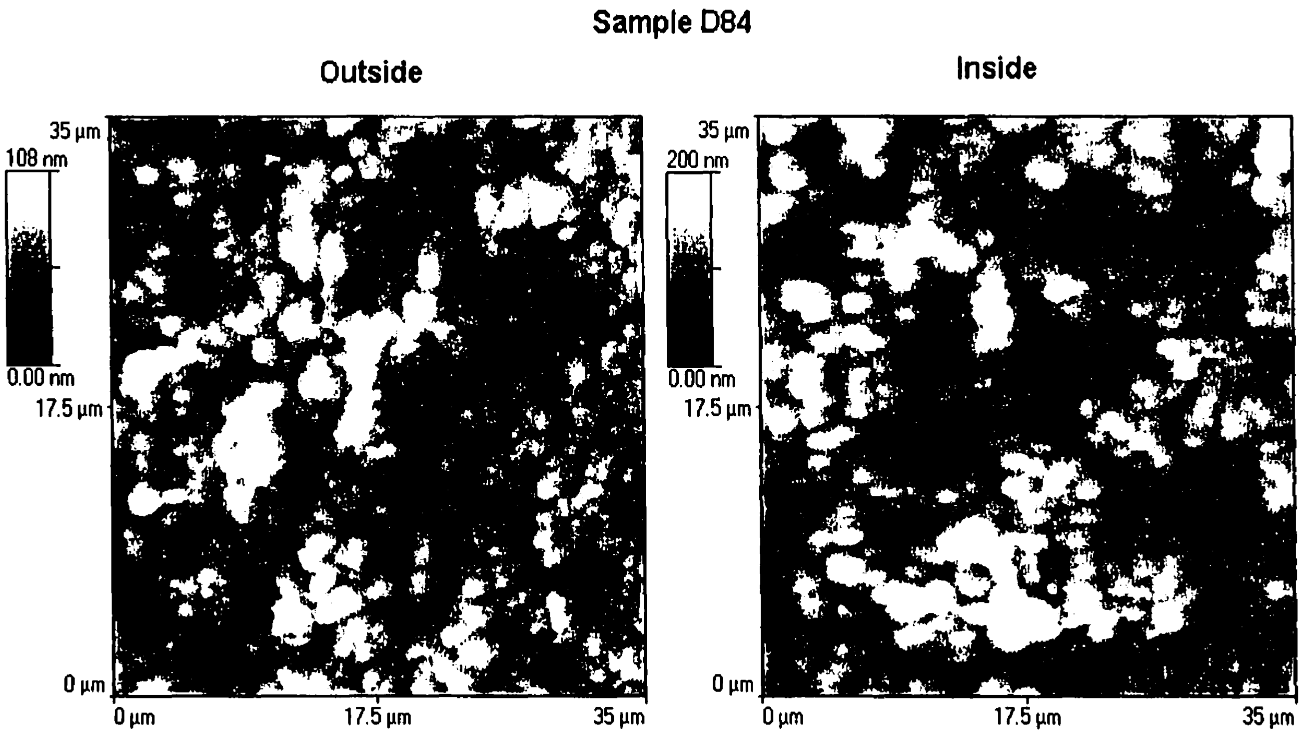

Figure B-5: Outside and Inside surfaces of Sample D84 (P972403:978584)

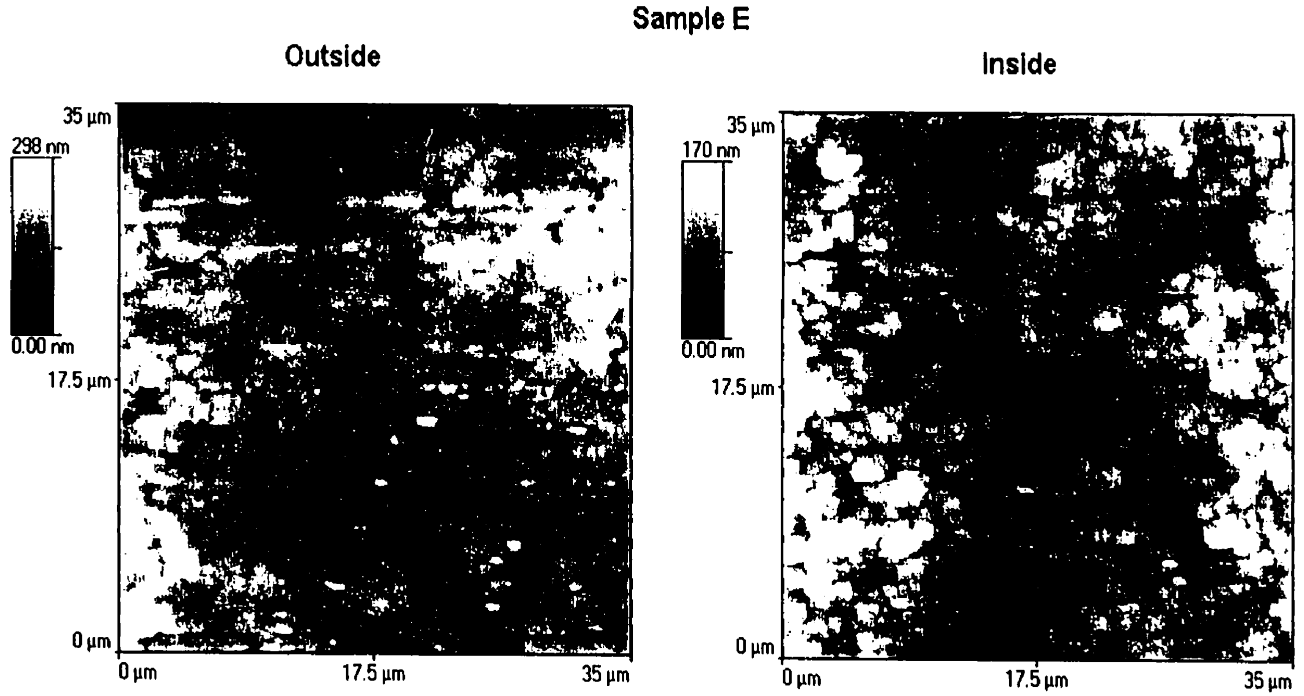

Figure B-6: Outside and Inside surfaces of Sample E

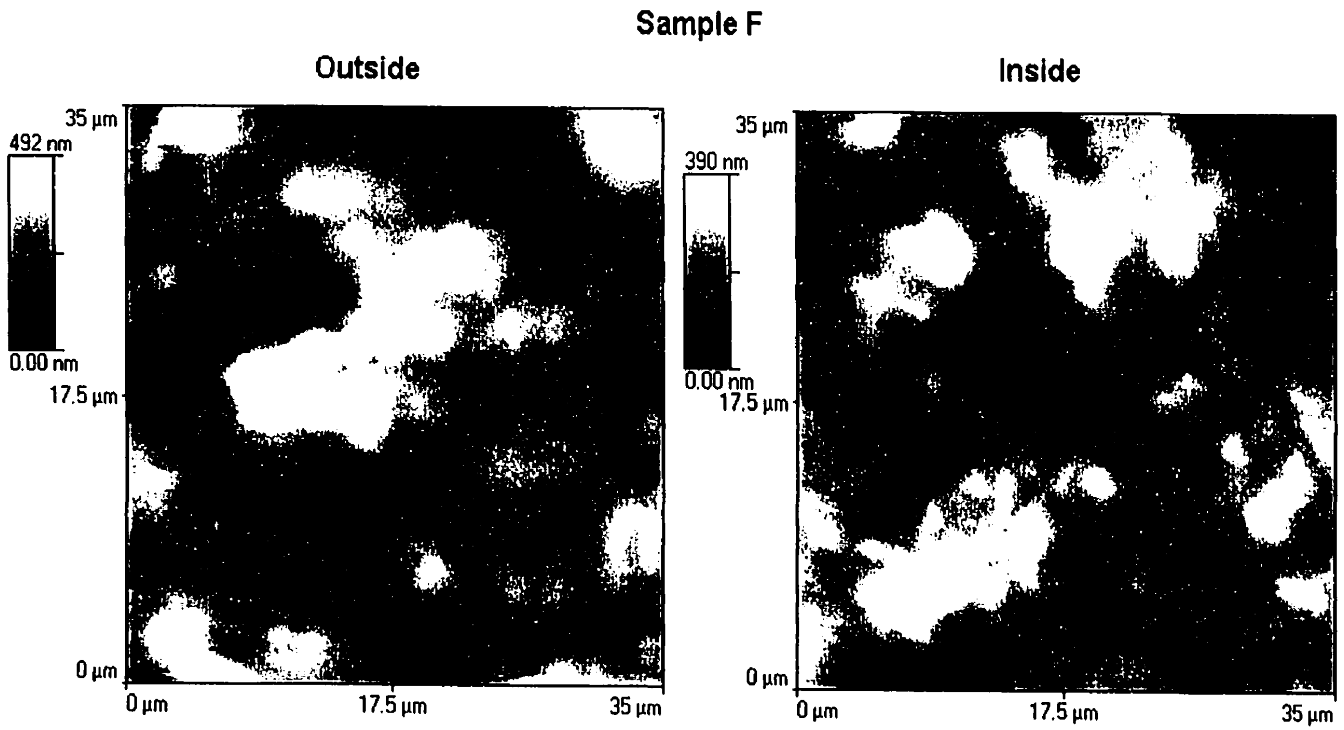

Figure B-7: Outside and Inside surfaces of Sample F (P971351:974751)

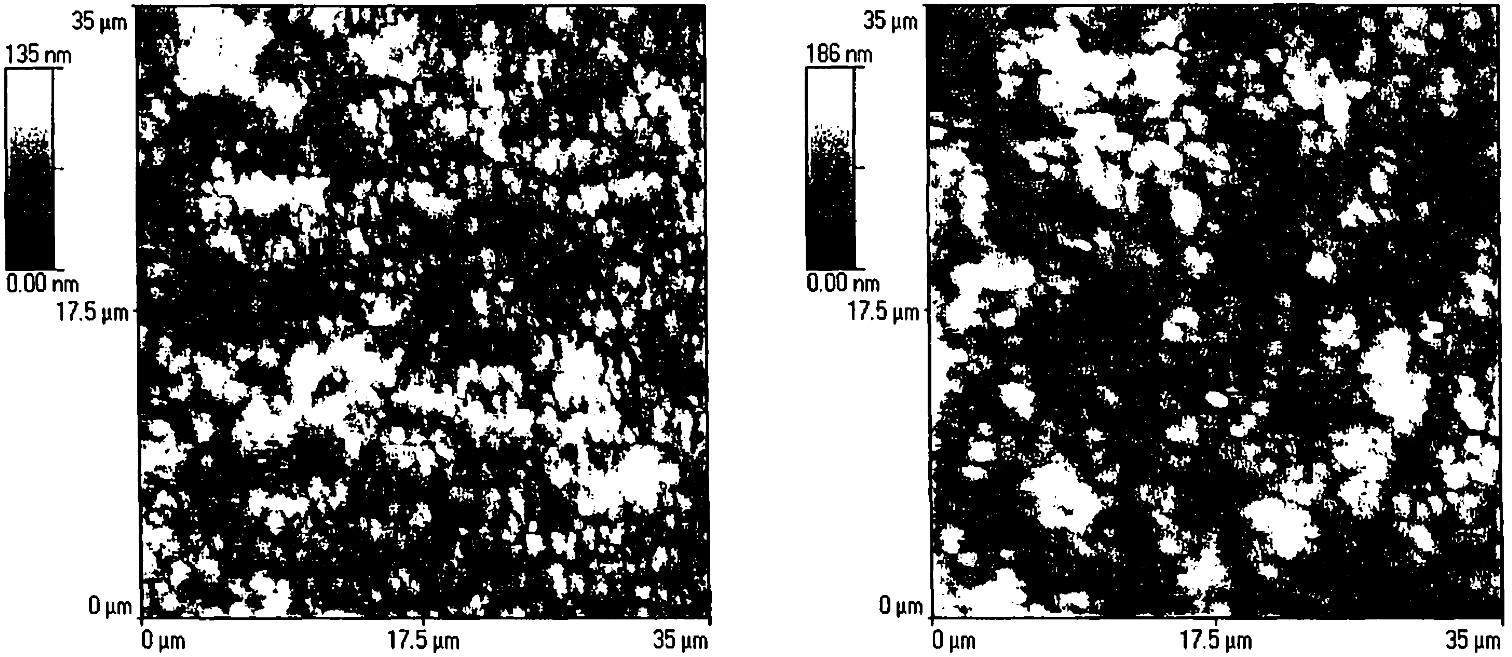

Outside Surface

Inside Surface

Figure B-8: Outside and Inside surfaces of Sample G (P972403:978583)

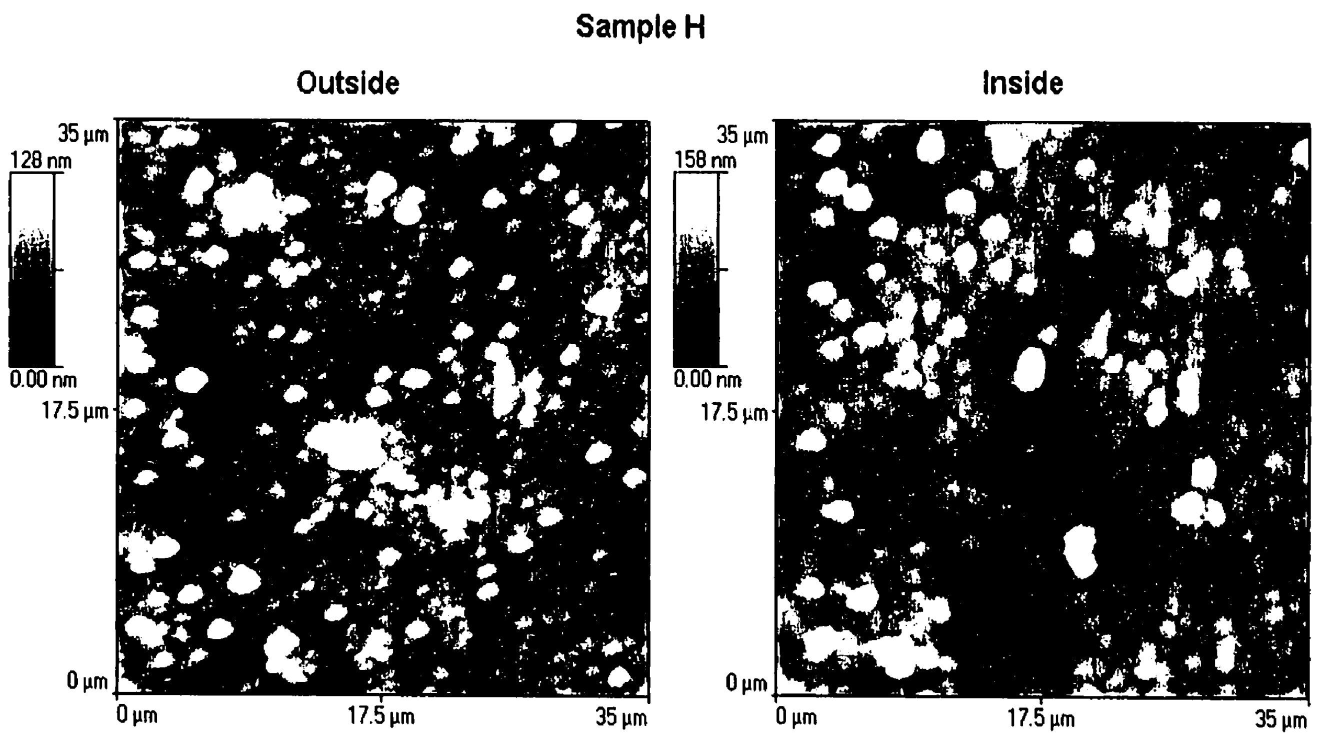

Sample H

Outside

Inside

Figure B-9: Outside and Inside surfaces of Sample H (P971664:975866)

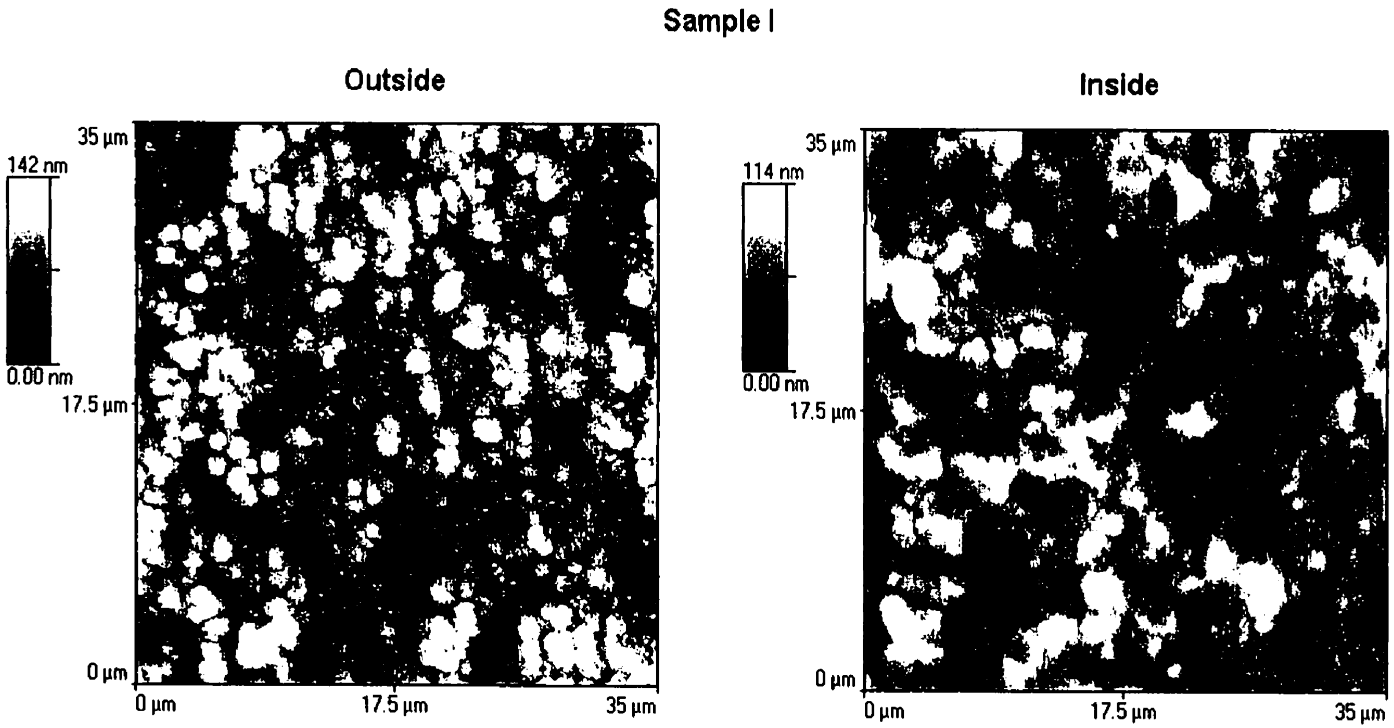

Figure B-10: Outside and Inside surfaces of Sample I

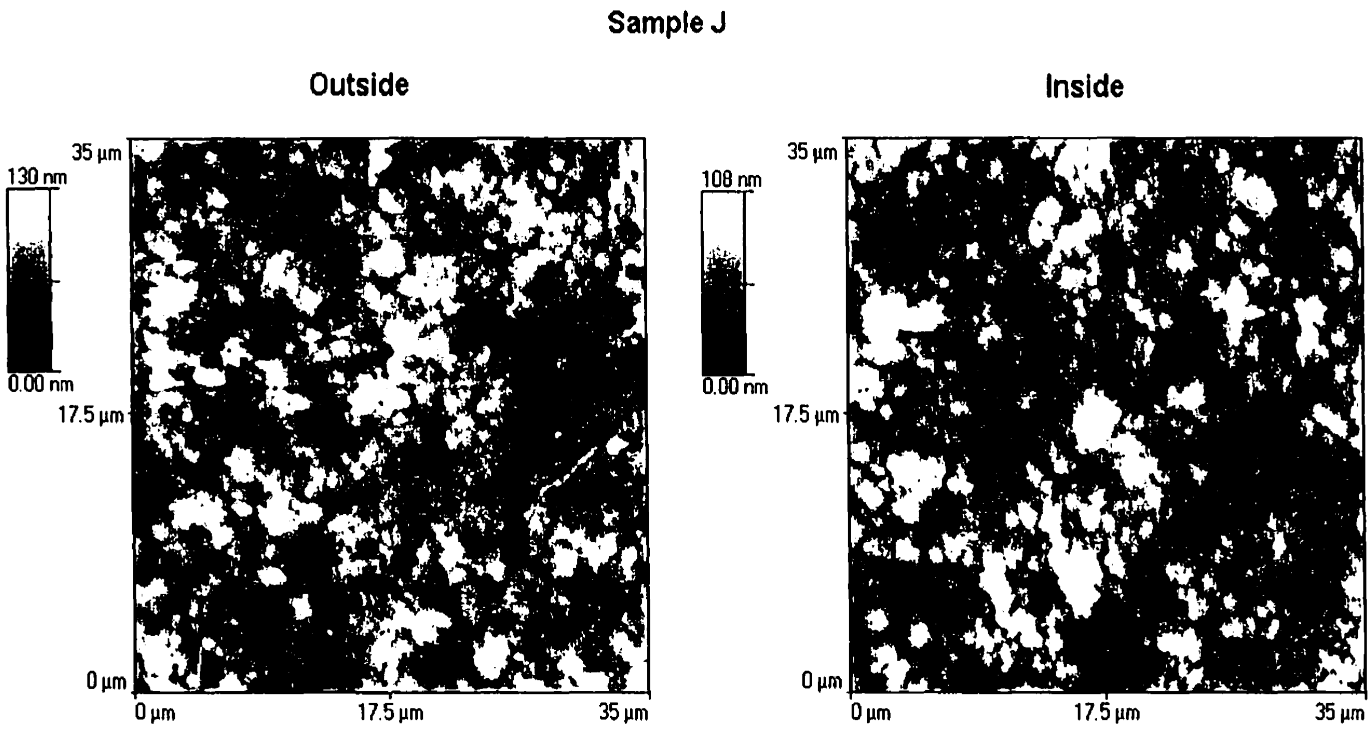

Figure B-11: Outside and Inside surfaces of Sample J

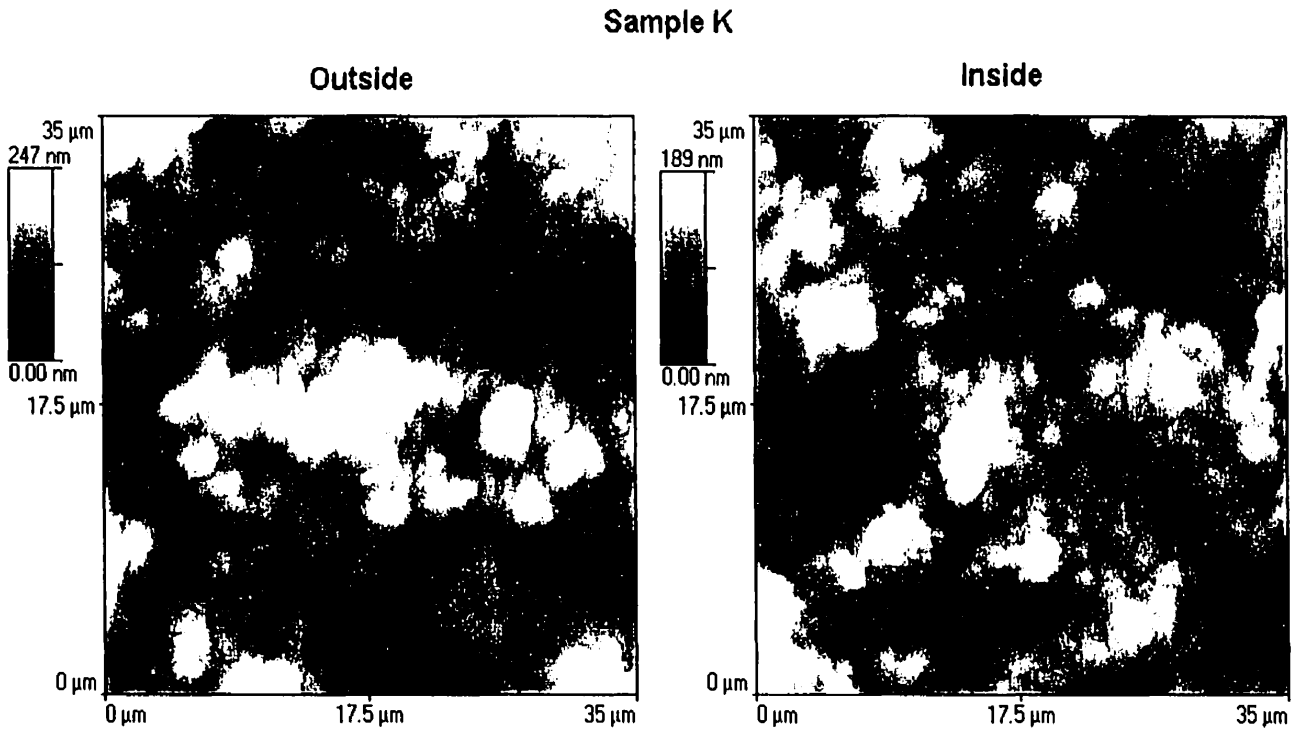

Figure B-12: Outside and Inside surfaces of Sample K (P971351:974752)

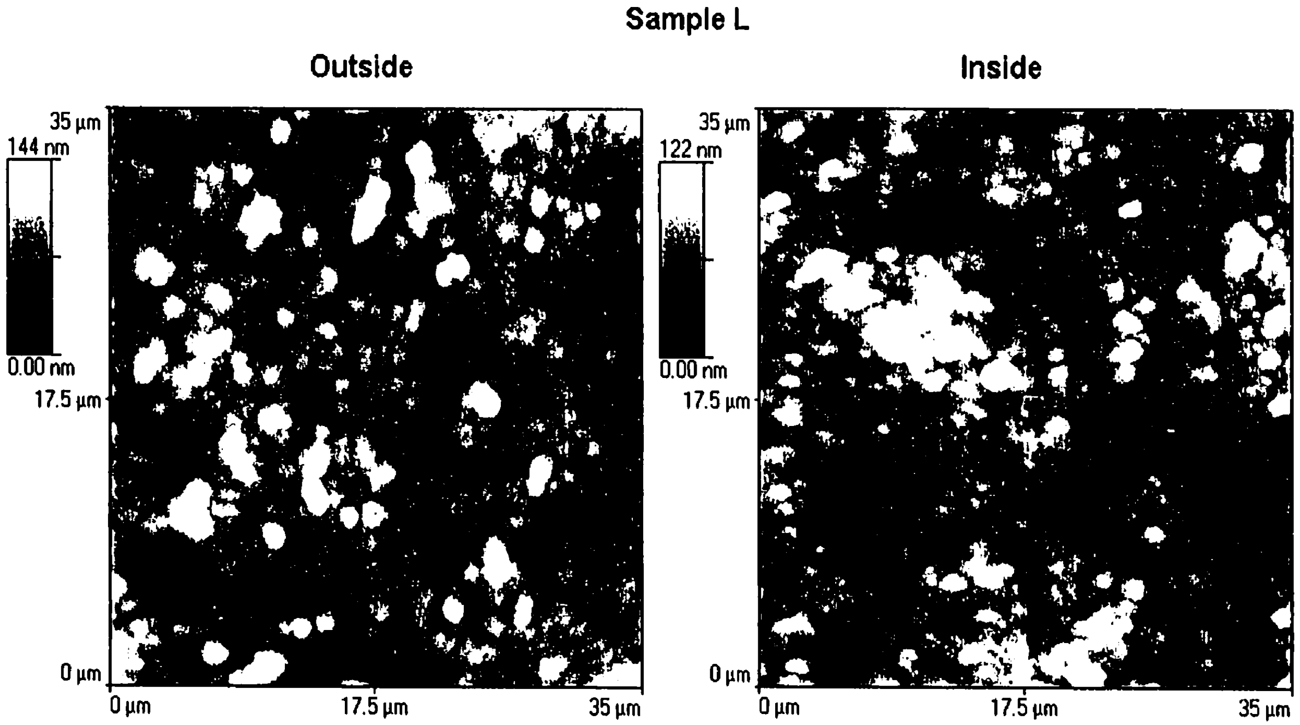

Figure B-13: Outside and Inside surfaces of Sample L (P970268:970703)

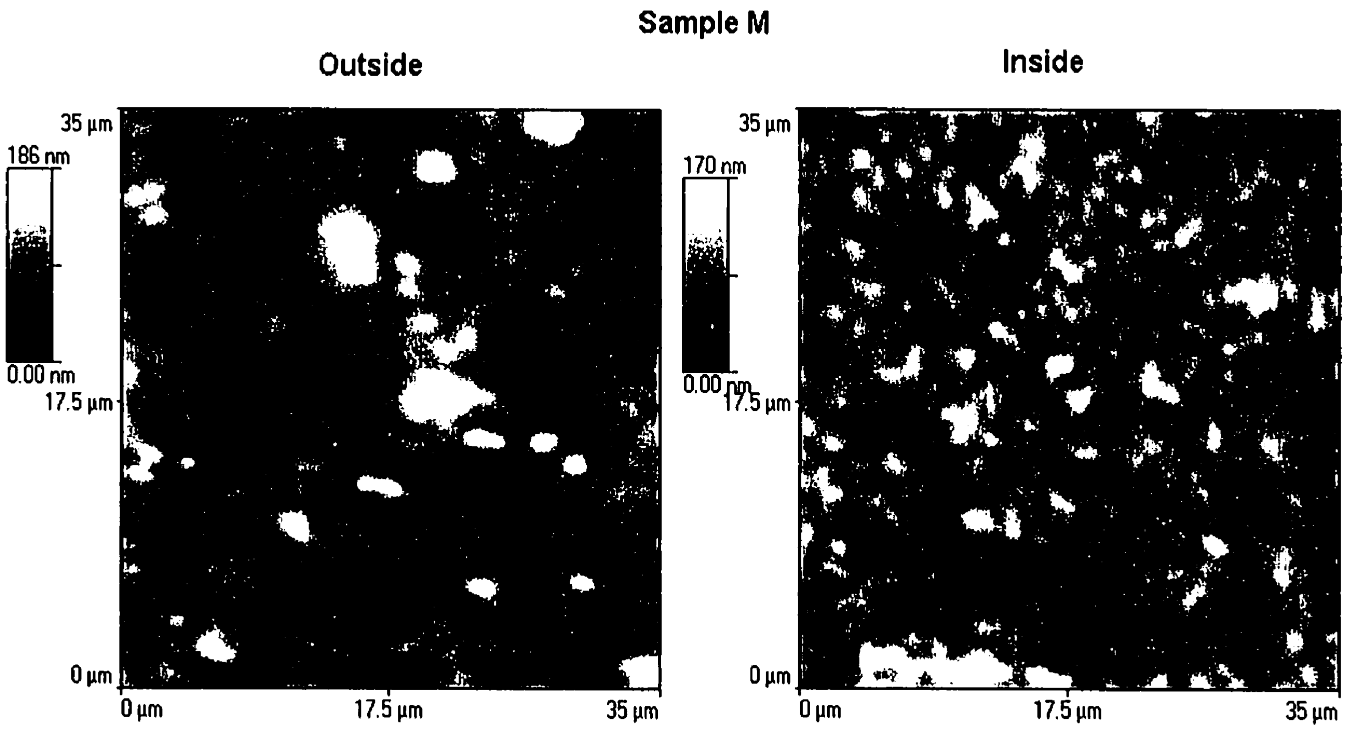

Figure B-14: Outside and Inside surfaces of Sample M (P9807250:9807251)